②

AD-A227 713

GL-TR-90-0131

IR PLASMA EMISSIONS

Precila C.F. Ip
Russell A. Armstrong

Mission Research Corporation
One Tara Blvd., Suite 302
Nashua, NH 03062

April 1990

DTIC
ELECTE
OCT.2 3.1990
S B D

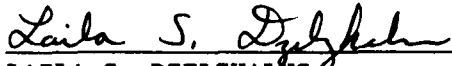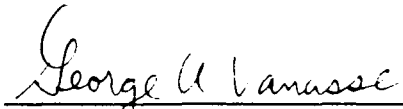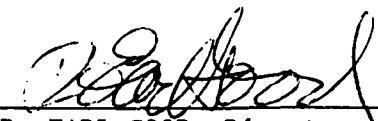Final Report
August 1986-March 1990

APPROVED FOR PUBLIC RELEASE; DISTRIBUTION UNLIMITED

90 10 22 197

"This technical report has been reviewed and is approved for publication"

LAILA S. DZELZKALNS
Contract Manager
Infrared Physics Branch
Optical/Infrared Technology Div.

GEORGE A. VANASSE, Chief
Infrared Physics Branch
Optical/Infrared Technology Div.

R. EARL GOOD, Director
Optical/Infrared Technology Div.

REPORT DOCUMENTATION PAGE

1a. REPORT SECURITY CLASSIFICATION	1b. RESTRICTIVE MARKINGS
UNCLASSIFIED	NONE

2a. SECURITY CLASSIFICATION AUTHORITY	3. DISTRIBUTION/AVAILABILITY OF REPORT
N/A	Approved for public release, distribution unlimited.
2b. DECLASSIFICATION/DOWNGRADING SCHEDULE	
N/A	

4. PERFORMING ORGANIZATION REPORT NUMBER(S)	5. MONITORING ORGANIZATION REPORT NUMBER(S)
MRC-NSH-R-90-003	GL-TR-90-0131

6a. NAME OF PERFORMING ORGANIZATION	6b. OFFICE SYMBOL (If applicable)	7a. NAME OF MONITORING ORGANIZATION
Mission Research Corporation		Geophysics Laboratory

6c. ADDRESS (City, State, and ZIP Code)	7b. ADDRESS (City, State, and ZIP Code)
1 Tara Blvd., Suite 302 Nashua, NH 03062-2801	Hanscom AFB, MA 01731-5000

8a. NAME OF FUNDING/SPONSORING ORGANIZATION	8b. OFFICE SYMBOL (If applicable)	9. PROCUREMENT INSTRUMENT IDENTIFICATION NUMBER
Geophysics Laboratory	OPI	F19628-86-C-0100

8c. ADDRESS (City, State, and ZIP Code)	10. SOURCE OF FUNDING NUMBERS			
	PROGRAM ELEMENT NO	PROJECT NO	TASK NO.	WORK UNIT ACCESSION NO
Hanscom AFB, MA 01731-5000	61102F	2310	G4	BR

11. TITLE (Include Security Classification)

IR PLASMA EMISSIONS

12. PERSONAL AUTHOR(S)
Dr. Precila C. F. Ip, and Dr. Russell A. Armstrong

13a. TYPE OF REPORT	13b. TIME COVERED	14. DATE OF REPORT (Year, Month, Day)	15. PAGE COUNT
FINAL	FROM 8/86 TO 3/90	1990 April	118

16. SUPPLEMENTARY NOTATION

17.	COSATI CODES		18. SUBJECT TERMS (Continue on reverse if necessary and identify by block number)
FIELD	GROUP	SUB-GROUP	Oxygen Stark Broadening
			Plasma Hydrodynamics
			IR Emission Kinetics

19. ABSTRACT (Continue on reverse if necessary and identify by block number)

This final report summarizes the latest results in data acquisition and various modeling efforts of the GL-LINUS plasma. Plasma radiance equations relevant to the LINUS plasma are first reviewed. Experimental data on the early-time plasma continuum are next presented. This is followed by discussions of the calculations on Stark broadening, hydrodynamics, and kinetics. Finally, recommendations on future experiments and calculations are made based on the present results.

20. DISTRIBUTION/AVAILABILITY OF ABSTRACT	21. ABSTRACT SECURITY CLASSIFICATION
[X] UNCLASSIFIED/UNLIMITED ☐ SAME AS RPT ☐ DTIC USERS	Unclassified

22a. NAME OF RESPONSIBLE INDIVIDUAL	22b. TELEPHONE (Include Area Code)	22c. OFFICE SYMBOL
L. S. Dzelzkalns	617-377-3671	GL/OPI

DD FORM 1473, 84 MAR   83 APR edition may be used until exhausted.   SECURITY CLASSIFICATION OF THIS PAGE
All other editions are obsolete.

TABLE OF CONTENTS

iii

FIGURES

FIGURES (CONTINUED)

TABLES

I. INTRODUCTION

This final scientific report summarizes work performed for the period August 1986 – 15 March 1989 under GL contract no. F19628-86-C-0100. The objective of this contract effort is to understand disturbed upper atmospheric plasma processes which give rise to optical radiation that could degrade the target discrimination capabilities of surveillance systems. These processes include nuclear-induced plasmas and auroral excitation that are investigated in laboratory experiments (e.g. LINUS/LABCEDE) and related field experiments (e.g. HIRAM).

An understanding of the effects of nuclear airbursts on the atmosphere has long been a topic of national interest. Special interest has recently been focussed on the ultraviolet, visible and infrared emission processes and the potential operational constraints placed on surveillance systems by the persistence of these processes. Due to the ban on testing of atmospheric nuclear weapons, research into such optical radiation effects is constrained to extrapolation from the limited data base obtained in the 1950's and early 1960's, theoretical developments and various experimental simulation techniques.

Among the sources of UV/VIS/IR radiation are the processes associated with ion-electron interactions and recombination in the nuclear fireball plasma and plume. Current models of plasma radiation are based on classical theories of plasma properties[1]. While these models are based on solid physical principles, considerable uncertainties exist in areas where theoretical development is lacking. Furthermore, approximations and estimations are required to insure computational tractability. Uncertainties are further exacerbated by the fact that for most nuclear plasmas of interest, thermodynamic equilibrium cannot be assumed. The test-series data cannot be comprehensively used to validate these models since experimental observations were incomplete in the areas of interest.

In order to alleviate the lack of experimental data for model validation, GL began an experiment to generate plasmas for spectroscopic investigation. This experiment, called LINUS (Laser-Induced NUclear Simulation), is conceptually quite simple and well founded in the background literature. A Nd:YAG laser is focussed into a gas cell, whose pressure is externally controlled, causing a dielectric breakdown of the gas. An excellent review of this technique has been presented by Minck[2]. Time-resolved spectroscopy is then performed to gather detailed data on the relaxing plasma for nuclear plasma model validation.

1

Although the LINUS experiment has generated very interesting results, a complete understanding of the laser-induced plasma processes vis-a-vis nuclear-induced plasma processes is not yet developed. In order to quantitatively benchmark present models against the LINUS results, such an understanding is required. This report is designed to push the LINUS results beyond phenomenological observation to analytical understanding and to determine the fidelity of LINUS for nuclear plasma model validation.

Chapter II of this report describes the LINUS plasma issues and analytic relationships that form the basis for the present model. The purpose of this review section is to focus on and identify those parameters requiring experimental investigation.

In Chapter III, the results of experimental efforts to obtain information on the LINUS continuum radiation are presented and discussed in terms of their implications for the conditions in the plasma. The observation of unexpected narrow-line emission is also presented along with a possible explanation.

Chapter IV discusses the effect of plasma microfields on atomic energy levels and of electron collisions on linewidths. This includes the details of the Stark calculations as well as synthetic spectra for comparison with the LINUS data.

Chapter V covers in detail the SALE hydrodynamic calculations that have been performed to aid in understanding the LINUS dynamics. These results indicate a rapid shock expansion and fully spatially developed plasma "fireball" at times early with respect to spectroscopic observations of interest.

Chapter VI describes the present kinetic model and resulting calculations for a specific experimental condition. This approach couples the rate parameters with the temperatures derived from the SALE code covered in Chapter V. The results are shown to be consistent with those described in Chapter IV.

Chapter VII summarizes the findings to-date and concludes with specific recommendations for further work.

II. LINUS PLASMA ISSUES AND ANALYTIC RELATIONSHIPS

A. GENERAL

The purpose of this chapter is to discuss the underlying issues involving plasma effects and the rationale for the LINUS experimental approach. The analytic relationships that form the basis for the present nuclear plasma emission model are described and parameters requiring experimental investigation are identified.

In the nuclear exchange environment, plasma processes are the dominant emission mechanism in the region of the fireball. Models of these processes exist, but a combination of gaps in theoretical knowledge, required computational approximations and lack of verifying data result in substantial uncertainties in the predictive models. The model presently used by the DNA community (EGG22) is based on Sappenfield's plasma model[3]. This model has been compared favorably with some test data, (to the extent that the electron density is known) and somewhat less favorably to other data. There is very little useful quantitative experimental data for validating EGG22, thus LINUS is intended to achieve benchmark analytical understanding to aid in further model validation. There are certain fundamental parameter issues and analytical relationships involving nuclear and LINUS fireball plasma processes which are presented here for review and completeness.

The regimes of interest for understanding plasma processes are generally divided into three altitude categories: low (<30 km), intermediate (30 km-90 km) and high (>90 km). At altitudes below 60 km, the fireball is contained in a relatively small region of space and reaches thermodynamic equilibrium very rapidly. Therefore, for the LINUS investigations, this regime is not of particular interest and is not further discussed. In the altitude regime from 60 km to 150 km, the fireball becomes much more expansive and dominates the emission for the first few tens-of-seconds to minutes (yield, altitude-dependent). In this region, the atmosphere is more tenuous and thermodynamic equilibrium is not achieved on time scales of interest. Therefore the prediction of plasma emission from the fireball becomes more important and also more difficult. In the fireball, the atmospheric molecules are completely dissociated and a high level of ionization occurs, resulting in emission as the plasma relaxes via free-free (bremsstrahlung), free-bound (recombination) and bound-bound (de-excitation) processes. The plasma bremsstrahlung,

recombination and radiative de-excitation processes give rise to continuum and line emission across the entire optical regime.

For very high altitudes (>200 km), plasma emission is also important but tends to be at lower radiance levels spread over very large geographic regions. Since the atmosphere is very tenuous at these altitudes, and since there are very few molecules, the term "fireball" may be inappropriate, as there is generally not a well defined boundary region. Given both the nuclear airburst phenomenology and the LINUS experimental conditions, the results of the LINUS experiment are most applicable to part of the intermediate and high altitude regimes. Although emphasis has been placed on the infrared in the past, SDI requirements have expanded the interest across the visible and into the ultraviolet.

The processes of interest in the intermediate and high altitude regimes as listed above are discussed here with some emphasis on the important parametric issues. Additional details can be found in Zel'dovich and Raizer[4] or the MRC "Physics of High-Altitude Nuclear Burst Effects" handbook[5]. These discussions are based on the absorption and emission coefficients, related by Kirchhoff's law, which states that in *thermodynamic equilibrium*, the spectral emission coefficient, ϵ_ν, is given by the product of the corresponding blackbody emission at the specific temperature, B_ν, and the absorption coefficient, α_ν, i.e.

$$\epsilon_\nu = B_\nu \alpha_\nu. \qquad \text{(erg s}^{-1}\text{ cm}^{-3}\text{ Hz}^{-1}) \qquad \text{(II.1)}$$

The caveat in this is the assumption of thermodynamic equilibrium. For free-free transitions, the initial "states" are not defined and the temperature is the electron temperature. For free-bound, the initial "state" (or final, if absorption) is a continuum and the temperature is again the electron temperature. For a description of the bound states, one must be able to define a temperature, thus Saha equilibrium is assumed. This is an important point, since Kirchhoff's relationship relies on a definable temperature where detailed balancing applies. If the system cannot be described by at least some "quasi-equilibrium" with a definable temperature, then the Kirchhoff relation does not hold.

Given that one can describe the absorption and emission coefficients by the Kirchhoff relation, it takes the form

$$\epsilon_\nu = \frac{8\pi h\nu^3}{c^2} \alpha_\nu \exp(-h\nu/kT), \qquad \text{(erg s}^{-1}\text{ cm}^{-3}\text{ Hz}^{-1}) \qquad \text{(II.2)}$$

where

ϵ_ν = emission coefficient
ν = photon frequency
α_ν = absorption coefficient (cm^{-1})

and all other symbols have their usual meaning.

The absorption coefficient must be corrected for stimulated emission if there is appreciable population in the upper-state level. In this case the partition function $[Q = 1 + exp(-E_i/kT) +...]$ has contributions from the second (and higher) terms and the exponential correction term must be applied. Hence the corrected absorption coefficient, α_ν', is defined as

$$\alpha_\nu' = \alpha_\nu[1-exp(-h\nu/kT)]. \qquad (cm^{-1}) \qquad (II.3)$$

B. FREE-FREE TRANSITIONS IN THE FIELD OF AN ION

Free-free (Bremsstrahlung) emission results from the acceleration of an electron in the field of a neutral or ion. Since the initial and final "states" of the electron are not quantized, the resulting emission is a continuum. The free-free/ion emission level as a function of frequency can be solved using classical Coulomb-field analytical physics, resulting in the relation

$$\epsilon_\nu = \frac{32\pi}{3} \left[\frac{2\pi}{3mkT}\right]^{\frac{1}{2}} \frac{e^6}{mc^3} N_e \, exp(-h\nu/kT) \sum_i (Z_i^2 N_i^+) \quad (erg \; s^{-1} \; cm^{-3} \; Hz^{-1}) \quad (II.4)$$

where

m = electron mass
e = electron charge
N_e = free electron number density
N_i^+ = density of ion, i
Z_i = charge number

and all other symbols have their usual meaning. The summation is over all charge states, which must be approached cautiously. In EGG22, it is assumed that Z=1, i.e. only singly charged species are present for times of interest. This is most likely a good assumption for a nuclear case but the

5

LINUS data suggests that at times shorter than ~100 nS, higher charge states contribute to the emission. Hence, judicious use of time-resolved spectroscopy to determine the relative charge-state density is important.

Equation (II.4) is derived from classical physics and gives a slightly different result than that derived from quantum physics. The difference between the two is normally accounted for by applying a correction term called the Gaunt factor. However, this correction term is very close to unity except when $h\nu \ll kT$, a situation not of interest to LINUS.

The corresponding absorption coefficient for free-free in the field of an ion (inverse bremsstrahlung) is given by combining expressions (II.2), (II.3), and (II.4) to yield

$$\alpha_\nu' = \left[\frac{2\pi}{3mkT}\right]^{\frac{1}{2}} \frac{4e^6}{3hcm\nu^3} N_e \sum_i (Z_i^2 N_i^+)[1-\exp(-h\nu/kT)]. \qquad (cm^{-1}) \qquad (II.5)$$

Inspection of eqs. (II.4) and (II.5) shows important characteristics of free-free ion emission/absorption for LINUS investigation.

(1) The coefficients are a function of the degree of ionization, hence electron density. Since $N_e = nN_i$, $\epsilon_\nu, \alpha_\nu' \propto N_e^2$ (n is a coefficient determined by the relative charge-state densities). It is therefore important in LINUS to determine the charge states before applying eq. (II.5).

(2) The temperature given refers to the *electron* temperature.

(3) The absorption coefficient is inversely proportional to the cube of the frequency. Thus at longer wavelengths, absorption may become relatively important for LINUS. This will have to be determined when extending LINUS to the LWIR.

C. FREE-FREE TRANSITIONS IN THE FIELD OF A NEUTRAL

The derivation of expressions to describe this process is much more difficult than for a free-free transition in the field of an ion. For the neutral, the classical Coulomb attraction term is not operative and the field felt by the electron near a neutral is both ill-defined and a much

6

stronger function of separation distance. Furthermore, the free-free/neutral coefficients are much weaker than with the ion, and are relatively important only when the degree of ionization is low. This is likely to be achieved in most nuclear scenarios in a few seconds. However, on time scales of LINUS, this condition is likely not met until after ~1 μS. Since so little experimental information is available on the topic and substantial uncertainty in the emission level predictions exists, any chance of obtaining additional information from LINUS should be pursued.

The derivation given by Zel'dovich and Raizer[4] for the free-free/neutral emission coefficient comes from the expression for the absorption of radiation in the neutral field, given by

$$\alpha_\nu' = 4e^2\sigma N_a N_e [1-\exp(-h\nu/kT)] \left[\frac{2/(3\sqrt{2})}{hcm^{3/2}\nu^3}\right] \int_0^\infty [(E+h\nu)^2/\sqrt{E}]\, f(E)dE \quad (cm^{-1}) \quad (II.6)$$

where

σ = scattering cross section for electron-atom interaction
N_a= neutral atom density
E = free electron kinetic energy
$f(E)$= electron kinetic energy distribution function
      = $2\{E/[\pi(kT)^3]\}^{\frac{1}{2}}\exp(-E/kT)$.

Upon integration, one derives

$$\alpha_\nu' = \frac{4e^2\sigma}{3hc\nu^3}\left[\frac{2}{\pi m^3 kT}\right]^{\frac{1}{2}}[2(kT)^2+2h\nu kT+(h\nu)^2][1-\exp(-h\nu/kT)]N_a N_e. \quad (cm^{-1}) \quad (II.7)$$

Combining eqs. (II.2) and (II.3) with eq. (II.7), one obtains the emission coefficient for free-free/neutral,

$$\epsilon_\nu = \frac{32\pi e^2\sigma}{3c^3}\left[\frac{2}{\pi m^3 kT}\right]^{\frac{1}{2}}[2(kT)^2+2h\nu kT+(h\nu)^2]N_a N_e\, \exp(-h\nu/kT). \quad (II.8)$$

$$(erg\ s^{-1}\ cm^{-3}\ Hz^{-1})$$

7

Again, several points need to be raised concerning the formulation of eq. (II.8).

(1) The formulation of eq. (II.8) is not to be considered as exact. In fact, different temperature and energy dependences can be derived based on different representations of the electron-neutral atom interaction. This formulation is the one presently used in the EGG22 nuclear plasma emission model.

(2) The cross section for interaction is not very well established but has a direct effect on the coefficient. The current model (EGG22) uses cross sections derived from the experimental results of Taylor and Caledonia[6] which are expressed in terms of radiative absorption coefficients. However, the measurements were only made at three wavelengths (2.0 μm, 3.5 μm, and 5.0 μm) and one electron temperature. There is thus a considerable uncertainty in extrapolating and interpolating these results to different wavelengths. A possible alternative is to use the theoretically calculated results of Geltman[7] which have yielded reasonable agreement with the experimental data in ref. 6.

(3) The temperature, as with free-free/ion, is the electron kinetic temperature and has a more pronounced effect than with the ion.

(4) The emission coefficient for free-free/neutral is a linear function of N_e. This is in contrast to the stronger N_e^2 dependence in the case of free-free/ion.

D. FREE-BOUND EMISSION

The derivation of expressions to describe free-bound emission begins with the realization that this process is the inverse of photoionization. In the photoionization process, energy is absorbed from discrete levels into a continuum. A useful descriptive model is to consider a series of occupied levels near the ionization limit in an ensemble of atoms and ions under the influence of a radiation field. As the energy of the photons increases, the threshold for ionization of the highest occupied level is achieved and absorption occurs. As the photon energy continues to increase, radiation continues to be absorbed with the excess energy accommodated in kinetic energy of the free electron. When the threshold

8

for ionization of the second highest energy level is reached, more energy is absorbed as that level is ionized. This effect is repeated with increasing photon energy with the result of a "sawtooth" structure in the absorption spectrum. If energy levels asymptotically approaching the ionization limit are populated, then the "teeth" in the spectrum are sufficiently close in energy that they appear to be a quasi-continuum. Functionally, as the wavelength of the radiation increases across the visible into the infrared, the "sawtooth" structure smooths out to approach a continuum in the infrared. The inverse process of emission results in the same structure as electrons are captured from a Maxwellian (or other) distribution into discrete states.

The photoionization cross section for a given bound state, i, is given by Kramers' formula (see Zel'dovich and Raizer, ref. 4) as

$$\sigma_\nu^{\ i} = \frac{64\pi^4}{3\sqrt{3}} \frac{e^{10}mZ^4}{h^6c\nu^3 n_i^{\ 5}} \qquad (cm^2) \qquad \text{(II.9)}$$

where n_i is the principal quantum number of the ith bound state. The absorption coefficient for an ensemble of atoms in the radiation field is then given by

$$\alpha_\nu' = \sum_i N_i \sigma_\nu^{\ i}[1-\exp(-h\nu/kT)] \qquad (cm^{-1}) \qquad \text{(II.10)}$$

where N_i is the density of the populated state, i, and the summation is over all bound states with energy less than or equal to $h\nu$.

In order to proceed further with this analytical derivation, one must assume a definable temperature, i.e., some sort of quasi-equilibrium, and that the ground state population, N_0, is much greater than the sum of the excited state populations, N^*. These assumptions are probably accurate for atmospheric airbursts but are somewhat questionable for LINUS, depending on the relaxation time. This is problematic for LINUS since at early times, when T_e is large, radiative/collisional relaxation is much more rapid than recombination while at later times, when T_e decreases, relaxation and recombination times are of the same order. In the latter case, which is described by the collisional-radiative model, a modified Saha equilibrium is achieved. If this is true, then the assumptions may be valid in LINUS

for times greater than 0.1 μS. These assumptions lead to the expression
for the absorption coefficient

$$\alpha_\nu' = \frac{64\pi^4}{3\sqrt{3}} \frac{e^{10}mZ^4N}{h^6c\nu^3} [1-\exp(-h\nu/kT)] \sum_i \frac{\exp(-E_i/kT)}{n_i^3} \qquad (cm^{-1}) \qquad (II.11)$$

where
   N = total density of absorbers
   Z = residual charge, i.e. if N is neutral, Z = 1, etc.
   E_i = excitation energy of state, i.

Applying the Kirchhoff relation (II.2), the resulting emission
coefficient is found to be

$$\epsilon_\nu = \frac{128\pi^{7/2}}{3\sqrt{6}m} \frac{e^{10}N^+NgZ^4}{h^2c^3g_+(kT)^{3/2}} \exp(-h\nu/kT) \sum_i \frac{\exp(I_i/kT)}{n_i^3} \qquad (II.12)$$

$$(erg\ s^{-1}\ cm^{-3}\ Hz^{-1})$$

where
   g = statistical weight of the level i
   I_i = ionization potential of the level i
   n_i = principal quantum number of the level i.

The relative populations of charged species to neutral species, if
$N_0 \gg N^*$, is given by the Saha relation

$$\frac{N_+N_e}{N} = 2\left(\frac{2\pi m_e kT}{h^2}\right)^{3/2} \frac{g_+}{g} \exp(-I_0/kT) \qquad (cm^{-3}) \qquad (II.13)$$

where
   I_0 = ionization energy of the *ground state*.

It should be recognized that there is a defined *modified* Saha
equilibrium for the collisional-radiative regime[8] similar to eq. (II.13)
where I_0 is replaced by I^*. This means that under some conditions (like
LINUS) there is a range of excited states with $I < I^*$ (usually levels
within kT of ionization) such that the conditions of eq. (II.13) hold for

10

coupling excited levels to the ground level of the next higher charge state. The value of I^* must be determined by experimental evaluation of level populations, i.e. determine the applicable "temperature" coupling the levels of interest.

As with free-free emission, a correction term may be necessary to account for the difference in the quantum mechanical result and the classical result. This gaunt factor, G, is expressed as the ratio

$$G = (d\epsilon_\nu/d\nu)_{QM} \div (d\epsilon_\nu/d\nu)_{CL}. \qquad (II.14)$$

Its source lies in the quantum mechanical accounting of nuclear charge screening in the capture potential and the effect on emissivity of the plasma frequency under high electron density conditions. This plasma frequency is given by

$$\omega_p^2 = (N_e e^2)/(\pi m) \qquad (Hz^2) \qquad (II.15)$$

where
N_e = electron density
m = electron mass.

If the frequency of the photons of interest is less than the plasma frequency, then the reflectance rises and emissivity decreases. This is a condition unachievable in any realistic nuclear airburst of interest for plasma radiance. However, for LINUS, it may be an issue. For example, at 10 μm (1000 cm^{-1}), the frequency is ~ 3E13 Hz. Inserting this value into the expression for the plasma frequency, one derives a required electron density of 1E19 cm^{-3}. This is achievable in LINUS at atmospheric pressures, but not at pressures below 100 torr. However, the gaunt correction factor will likely not deviate excessively from unity except for very early times when free-bound is not important.

E. KRAMERS-UNSÖLD APPROXIMATION

In practice, the free-free and free-bound infrared components of the plasma emission can often be reduced to a single simplified expression via the Kramers-Unsöld approximation. This entails assumptions of the physical

11

state of the plasma that are often obtained under nuclear conditions but may not be applicable under the conditions of LINUS except in very specific time domains. These assumptions are:

1. Only neutral and singly ionized species are present in measurable quantities. This is true under most nuclear-plasma conditions, but indications are that it is valid only at times greater than ~0.1 μS in LINUS over most of the spatial regions in the discharge.

2. Free-free/ion interactions dominate over free-free/neutral. This is a direct consequence of the starting assumptions which lump the free-free/ion with the free-bound emission. Free-free/neutral is usually handled separately. This condition is most likely met in LINUS for times <0.1 μS, but not necessarily in nuclear-plasmas or in LINUS for times >0.1 μS.

3. $h\nu \leq kT$ (and by correspondence, $h\nu \ll I$). This is obviously a function of the observation time of emission. At early times, when the temperature is high, optical emission can be treated with the Kramers-Unsöld approximation. At later times, when the temperature decreases, the treatable wavelengths extend into the infrared and visible/ultraviolet emission are not accurately treated with the approximation.

4. Ground state populations exceed the sum of excited state populations. This is probably true for both LINUS and for nuclear-plasmas since allowed radiative channels to the ground state exist with very large Einstein coefficients, i.e. radiative relaxation is fast with respect to time scales of interest.

Given the assumptions, the desired result is obtained by summing eqs. (II.5) and (II.11) and including the correction for stimulated emission, $\alpha_\nu' = \alpha_\nu[1-\exp(-h\nu/kT)]$. (The manipulative algebra is not presented here. For the details, see Zel'dovich and Raizer, (ref. 4, pp 270-271)). The Kramers-Unsöld expression for the absorption coefficient is

$$\alpha_\nu' = \frac{16\pi^2}{3\sqrt{3}} \frac{e^6 Z^2 kTN}{h^4 c\nu^3} \exp[-(I-h\nu)/kT][1-\exp(-h\nu/kT)]. \quad (cm^{-1}) \quad (II.16)$$

12

Again, applying the Kirchhoff relation (II.2) (remember that the correction for the stimulated emission is already in eq. (II.16)) and the Saha equilibrium relation (II.13), one obtains the relation for the emission coefficient as

$$\epsilon_\nu = \frac{32\pi^{3/2}}{3\sqrt{6}} \frac{g}{g_+} \frac{e^6}{m^{3/2}c^3(kT)^{\frac{1}{2}}} N_+N_e. \qquad (\text{erg s}^{-1}\ \text{cm}^{-3}\ \text{Hz}^{-1}) \qquad (\text{II}.17)$$

Note that this relationship has no dependence on exponential energy or on wavelength. However, for infrared applications, the desired units are in $W\ cm^{-3}\ \mu m^{-1}$, and recall that $\nu = c/\lambda$, and thus $d\nu/d\lambda = -c/\lambda^2$ (minus sign is the direction of slope). Therefore multiplication of eq. (II.17) by c/λ^2 yields (including $10^4\ \mu m/cm$ and $N_+ = N_e$)

$$\epsilon_\lambda = \frac{(32E4)\pi^{3/2}}{3\sqrt{6}} \frac{g}{g_+} \frac{e^6}{m^{3/2}(kT)^{\frac{1}{2}}} \frac{1}{c^2\lambda^2} N_e^2. \qquad (\text{erg s}^{-1}\ \text{cm}^{-3}\ \mu m^{-1}) \qquad (\text{II}.18)$$

Thus these components of the plasma emission are reduced to an analytical expression involving the electron temperature and density. It is important to note the assumptions that were required for derivation of eq. (II.18). Specifically, it is only valid in the infrared, when $N_e = N_+$ and $N^* \ll N_0$, and when free-free/ion dominates over free-free/neutral. These conditions can be met in LINUS only at times when O^+ dominates.

F. BOUND-BOUND EMISSION

The technique used to model the bound-bound radiance as a function of electron density and temperature is based on the collisional-radiative recombination (CRR) model of Bates, Kingston and McWhirter[9], and McWhirter[8]. A reasonable discussion of the physics involved is contained in Sappenfield[3]. In this model, high-lying levels of the neutral atom are assumed to be in Saha equilibrium with the ion, and the electronic level populations are in quasi-steady state. Thus

$$N_i = N_eN_+(h^2/2\pi m_ekT)^{3/2}(g_i/2g_+)\exp(I_i/kT) \qquad (cm^{-3}) \qquad (\text{II}.19)$$

13

where the variables have their usual meaning. All transitions to the ground level are taken as optically thick so that real contributions to the radiance are given by intra-excited state transitions. One further assumption is that $N_e = N_i$, that is, by the time that this radiation matters, only singly ionized species exist. The result of this numerical model is a series of emission coefficients arranged in wavelength sequence given by

$$\epsilon_{ij} = h\nu_{ij}N_iA_{ij} \qquad (\text{erg s}^{-1} \text{ cm}^{-3}) \qquad (II.20)$$

where

ϵ_{ij} = Integrated emission coefficient

A_{ij} = Einstein coefficient for the transition,

and other variables are as defined previously. This expression for the plasma bound-bound emission is relatively straightforward, and yields specific line emission overlaying the continuum and quasi-continuum represented analytically for free-free and free-bound emission. Equation (II.20) is the basis for the discrete line emission in EGG22. Further details of the bound-bound emission model appear in ref. 3.

G. ISSUES

Inspection of the relationships described above yields a number of important parametric issues for LINUS plasma investigation.

1. Critical parameters for understanding the emission from LINUS for all the processes described above are the electron density and temperature. Thermodynamic equilibrium cannot be assumed, thus the time-dependent values of these parameters must either be measured or inferred from measurements. Because there is expected to be a radial distribution of both electron density and temperature, techniques for spatially resolved measurements of the emission must be implemented. The details of the electron parameters will determine the details of the emission processes. A spatially integrated measurement of the emission will yield a "lumped" signal, hindering detailed analysis of the contributing emission. In support of spatial experiments, application of hydrodynamics calculations will yield general parameters of internal energy, pressure and density as a function of space-and-time. High electron densities also cause broadening and shifting of lines.

14

2. Knowledge of the distribution over states of the recombined product is required to infer time-dependent relative populations. For a full understanding, this must include (a) the initial distribution, (b) the collisional coupling of levels, and (c) effects of state-dependent re-ionization. These requirements dictate detailed temporally resolved measurements of specific transitions to determine initial distributions and relaxation channels.

3. Knowledge of state-dependent transition probabilities is required for a full analytical understanding. This topic is strongly coupled to item 2. Under conditions of high electron density, Rydberg levels are strongly perturbed and transition probabilities can change by orders-of-magnitude. The result is a complex emission spectrum where lines are broadened, non-allowed transitions become relatively strong and emission wavelengths change as a function of time as the electron density/temperature relax.

4. Cross sections for both atom- and ion-electron collisional interactions and level-to-level coupling interactions must be determined. These are very difficult measurements which are probably not achievable in LINUS. However, with the appropriate spatial/temporal/spectral measurements, spectra are achievable which may be compared directly to nuclear plasma model predictions. For example, the free-free/neutral emission due to short-range interactions are not well understood. Under conditions where the electron density is <1% of the gas density and the electron temperature is well known, the measurement of the emission continuum will allow an estimate of the cross sections.

5. Optical opacity is an issue for both the LINUS experiment and for extensions of the EGG22 model. Free-free and free-bound absorption coefficients are described above. However, line emission is not treated explicitly due to computational constraints. In the model, only transitions to the ground state are treated as optically thick. However, extensions of the model to high electron and temperature conditions may result in increased optical opacity on other transitions. These are generally treated with a limit on the optical depth. The validity of this approach requires testing. Unfortunately, in LINUS, the pathlengths are generally sufficiently short that treating optical

15

opacity is difficult. However, both absorption and time-dependent emission features may be used in LINUS to investigate optical opacity.

6. Ultraviolet effects were not explicitly discussed in the plasma processes. However, for both LINUS and NWE, UV emission/deposition in the surrounding gas is an important topic. Models of UV deposition are only partly verified and emission from UV excited species can be important. LINUS experiments have shown the existence of highly excited *narrow* line emission that clearly emanates from cold regions around the discharge region. This indicates the possibility of investigation of UV deposition and signature processes surrounding the plasma region.

These fundamental parameters are the basis for the LINUS experimental program for both present-model validation and a first-principles time-dependent model of nuclear plasma relaxation.

III. SPECTROSCOPIC CONTINUUM AND LINE EMISSION EXPERIMENTS

A. GENERAL

This chapter presents the results of data acquisition on UV/VIS continuum radiation at early times (t ≤ 500 nS). Also described are the LINUS plasma conditions deduced from these experimental observations.

Former LINUS results[10,11] for O_2 and N_2 reported the observation of continuum radiation at early time (from time integrated spectra) from the visible to the infrared at a pressure of 125 torr. As described in Chapter II, continuum emission arises from bremsstrahlung and recombination processes, the emission coefficients of which are functions of electron temperature and density. Since early time continuum in LINUS is most likely dominated by free-free transitions in the field of ions, data have been gathered on continuum radiation in the visible at early times in order to obtain values for the electron density and temperature. To reiterate, the explicit functionality of the emission coefficient in the field of an ion is given by eq. (II.4):

$$\epsilon_\nu = \frac{32\pi}{3} \left[\frac{2\pi}{3mkT}\right]^{\frac{1}{2}} \frac{e^6}{mc^3} N_e \exp(-h\nu/kT) \sum_i (Z_i^2 N_i^+). \quad (\text{erg s}^{-1} \text{ cm}^{-3} \text{ Hz}^{-1})$$

From the above equation, it is seen that a plot of ln(emission) vs. frequency should give a slope of h/kT. Similarly, the intercept of the same plot should give a value for the electron density. Therefore, the continuum data should provide knowledge of the temporal dependence of electron temperature and density, parameters which are important inputs to the plasma spectral line radiance code presented in Chapter IV.

B. EXPERIMENT

Data were taken with the laser focused into the oxygen cell as described previously[11] and emission from the spark was resolved with a 0.5 meter monochromator. The scanning of the monochromator and data acquisition are computer-controlled. Typically, a 500 A scan with 0.1 A resolution is taken in the visible region with a scan time of 25 minutes. Acquisition was restricted to this scan time because the laser can be unstable without re-tuning for longer periods.

A 5000 A long-pass filter was inserted behind the entrance slit in the monochromator in order to prevent the appearance of higher order lines. Time resolved data were taken using a PAR 162/165 gated integrator-boxcar averager. The gatewidth is set at 50 nS with data taken for delay times of 0, 5, 10, 25, 50, and 100 nS. The laser beam profile (as measured using a fast photodiode) and boxcar aperture were monitored on a dual-trace oscilloscope. Time delay is defined by the time difference between the rise of the boxcar aperture and the peak of the laser profile as monitored on the oscilloscope. This is illustrated in Figure III.1A. The precision of the time delay is about 5 nS, as defined by observing jitter on the order of 0.5 cm on the oscilloscope when the time scale is set at 10 nS/cm.

In order to identify time zero more accurately, signals at 5050 A, 5550 A, and 6050 A were observed on the multimeter for times less than 0 nS. In general, no emission is observed for these three wavelengths when the time delay is less than -10 nS (see Figure III.1B). An alternative definition of time zero could then be the time when no emission is observed; this corresponds to the point when the rise of the boxcar aperture is aligned with the rise of the laser pulse. If one uses this new criterion for the definition of time zero, then the presently reported time delay, which is defined by the difference between the rise of the boxcar aperture and the peak of the laser profile, is shifted by 10 nS.

Absolute and relative calibrations have been obtained from 4500 A to 9000 A at monochromator slit widths of 25 μm and 50 μm using a tungsten-halogen lamp.

C. RESULTS

Three sets of data were taken: (i) 55 torr from 4000-4500 A for delay times of 100, 200, and 500 nS, (ii) 30 torr from 6000-6500 A for delay times of 100, 200, 300, and 500 nS, and (iii) 110 torr from 7500-8000 A for delay times of 25, 50, 100, and 300 nS. Data were first taken with the shutter opened and then closed in order to obtain the background DC offset. Data set (i) contains numerous O^+ lines (about one every 10 A) and is probably too congested to analyze for continuum. Data set (ii) was taken with the aim of reproducing earlier spectra taken with the optical multichannel analyzer[11]. However, the signal-to-noise was too small for delay times below 100 nS to make any meaningful comparison. Data set (iii) was taken with the slits set at 25 μm. There are only two oxygen neutral lines in this spectral region. Among the three pressures, data at 110 torr

18

A. PRESENT DEFINITION OF TIME DELAY , ΔT

BOXCAR GATE

ΔT

LASER
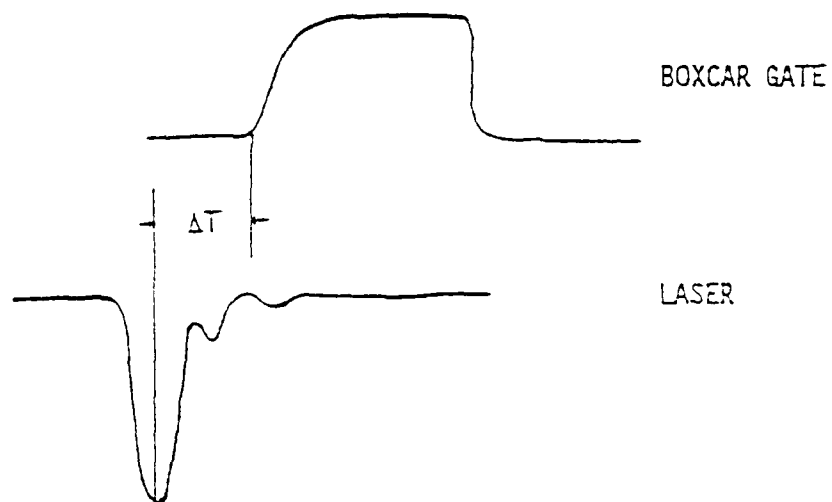
B. ΔT = -10 NS, WHEN NO EMISSION IS OBSERVED

BOXCAR GATE

ΔT

LASER
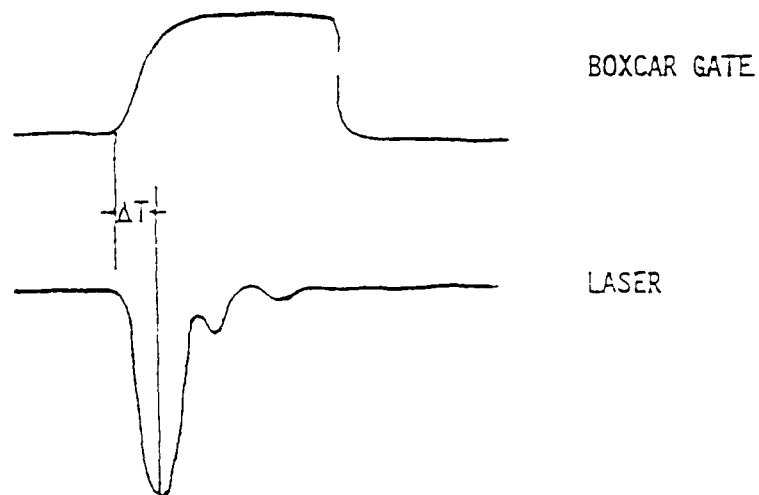
Figure III.1. LINUS time delay as monitored on the oscilloscope.

19

give the best signal-to-noise, hence a better chance of observing the continuum at early times. Consequently, data have been mostly collected at 110 torr from 5050 A to 8500 A.

Initially, data files were successfully transferred from the HP disks to a VAX and to a PC via the GL network. Later, data were transferred from the COCHISE HP-computer to the Zenith computer via the network and written onto IBM PC formatted diskettes.

Data analyses involve first correcting the data for the DC offset, and then calibrating against previously-obtained calibration curves. The calibrated 500A segments are then linked together and compared to blackbody and bremsstrahlung radiation curves obtained from theory.

Least squares fits of the calibration curves using a 4-term polynomial, shown in Figure III.2, give good results for wavelengths longer than 5500 A. However, the sinusoidal structure between 5000 A and 5500 A, arising from the transmission characteristics of the long-pass filter, could not be fitted using the same cubic polynomial or any polynomial which is between 4- to 10-term. To include the 5000-5500 A region as well, it will be necessary to refit the calibration curve using cubic splines.

Survey scans were subsequently taken with a wavelength increment of 1 A in order to obtain the general features of the visible continuum for various time delays. These scans have been calibrated and the results as a function of frequency (corresponding to wavelength of 5000-9000 A) for delay times of 500 to 0 nS are shown in Figure III.3.

D. DISCUSSION

From these time-resolved spectroscopic data, new and interesting observations have been made which have an important bearing on the understanding of the physical processes associated with the formation and evolution of the LINUS plasma.

From Figure III.3 it is observed that the continuum is steadily rising with increasing frequency. This is in contradiction to that expected from free-free bremsstrahlung emission in the field of an ion (see eq. II.4), which predicts an exponential decrease with frequency. The general shape is more consistent with blackbody emission, which would dominate if the plasma is optically thick at these times and if a homogeneous spark is assumed. The peak of the blackbody radiation curve

20
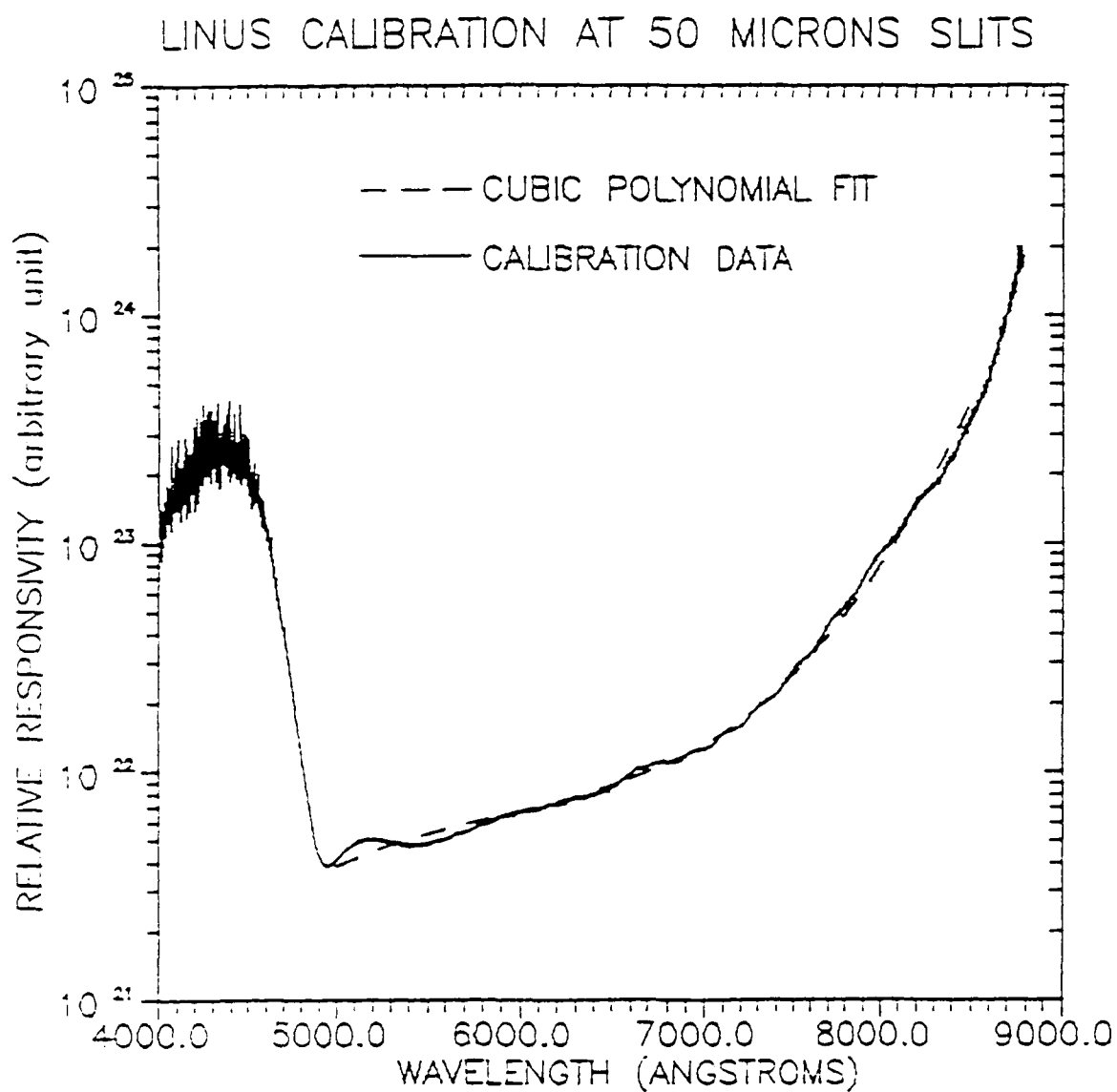
Figure III.2. LINUS relative calibration from 4000-9000 A and polynomial fit from 5000-8500 A for monochromator slitwidth of 50 μm.
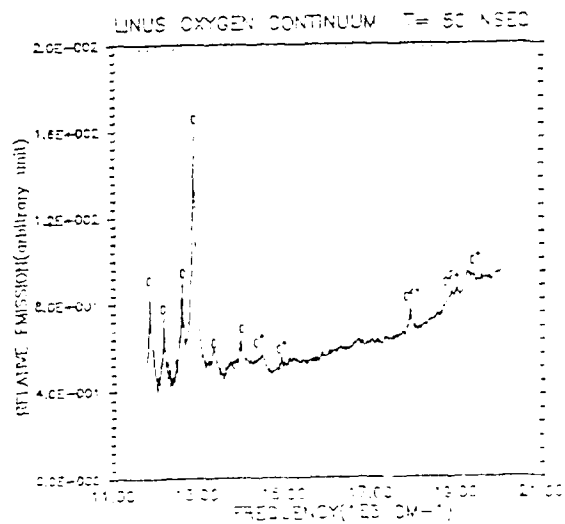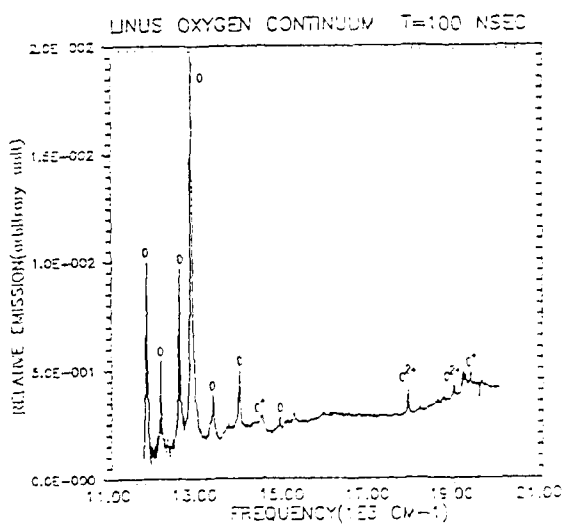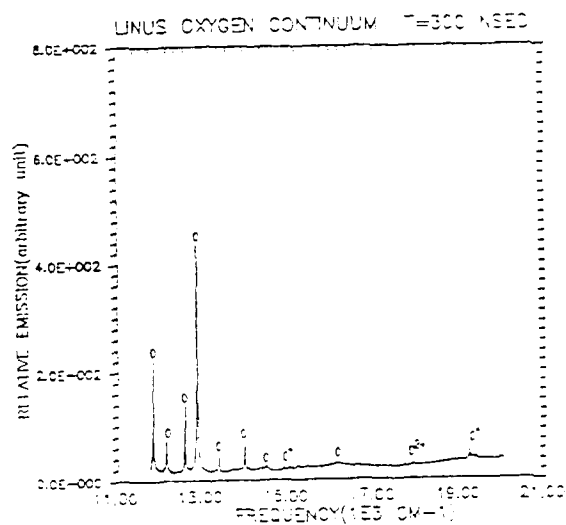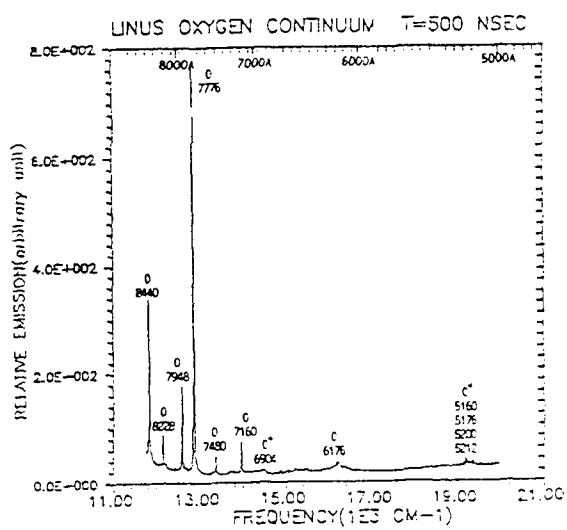
Figure III.3. LINUS relative calibrated oxygen emission for specified delay time.
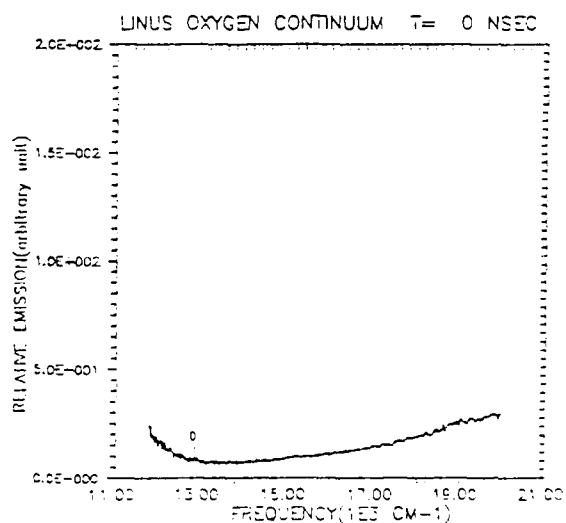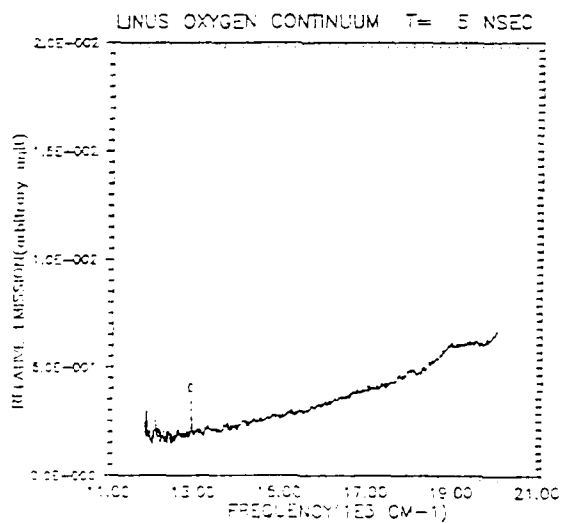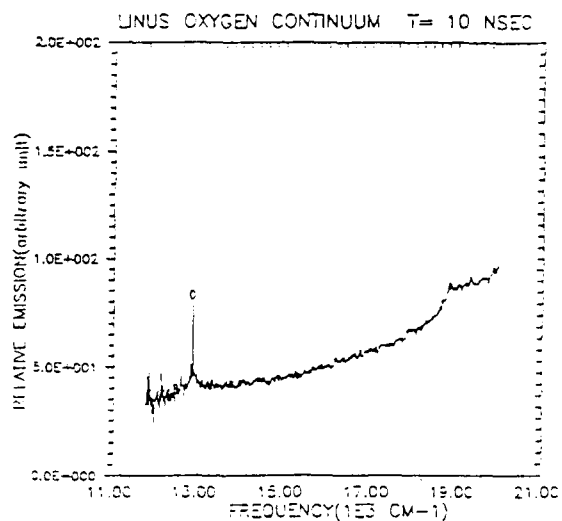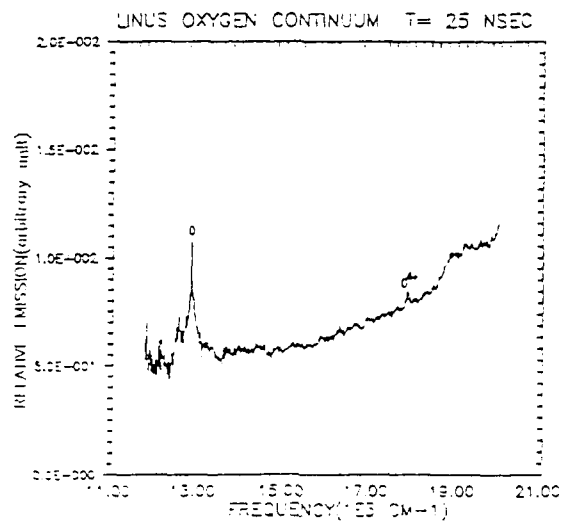
Figure III.3. LINUS relative calibrated oxygen emission for specified delay time.
(continued from previous page)

occurs at a frequency ν, related to the blackbody temperature, T, by $h\nu=2.82kT^4$. This is equivalent to $\lambda T \sim 0.5$, where λ is the peak wavelength in cm. If it is assumed that the temperature follows from the spectroscopic temperature measurements, then the early time temperature of 10^5 K results in a peak wavelength of ~500 A which lies in the x-ray region. In this case, continuum emission in the visible domain should increase with shorter wavelength. In order to perform fits to blackbody curves with different temperatures, more data are needed in the UV spectral region. If the data cannot be satisfactorily characterized by a blackbody temperature, it may be that the observed continuum is a combination of bremsstrahlung from the hot core and blackbody emission from the halo region surrounding the spark. To test this conjecture, spatially resolved experiments will be required.

The observed lines from these scans have been assigned to atomic oxygen ranging from neutral to O^{4+}. Identification of O^{3+} at times less than 25 nS is uncertain at the present because the only visible transition of O^{3+} listed for wavelengths longer than 5000 A is the multiplet at 5300 A. At this wavelength, transitions are also known which arise from oxygen neutral. Thus positive identification of O^{3+} at early times will have to await more data acquisition at wavelengths shorter than 5000 A where more O^{3+} transitions exist. There are two unassigned lines, a 5506 A line seen at 50, 100, and 500 nS and a 6580 A line observed at 100, 300, and 500 nS. The magnitude of the continuum is seen from Figure III.3 to be maximum at 25 nS.

Inspection of Figure III.4 indicates that the 7774 A emission due to the OI ^5P-^5S transition is strong at 300 nS and broadens at 100 nS. At 50 nS, this 7774 A transition shows a slightly resolved narrow line sitting on top of a broader emission peak. At 25 nS, this multiplet is completely resolved and the broad line underneath has disappeared. This narrow multiplet continues to appear at 10 nS and 5 nS. Similar observations, shown in Figure III.5, were made for the OI 8446 A line which arises from the ^3P-^3S transition. This multiplet, however, is not resolved under the present experimental conditions.

The presence of lines with narrow linewidths implies a cold gas surrounding condition. A possible explanation for the above observations could be that the narrow lines originate from x-ray/UV deposition/excitation of the relatively cold O_2 gas surrounding the fireball (i.e. O_2(cold) + $h\nu$ --> $2O^*$) and the broad emission arises from shock heating of the emission region and/or recombination events which dominate at late times. More experiments, however, need to be performed

24
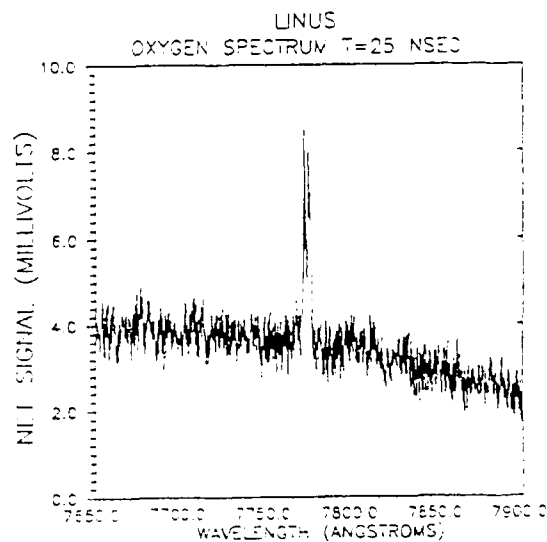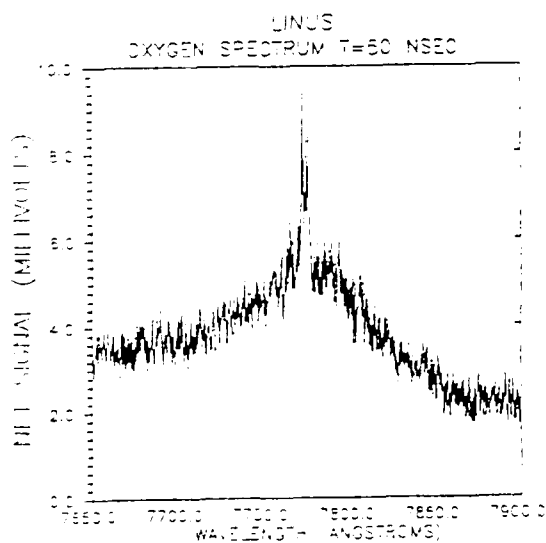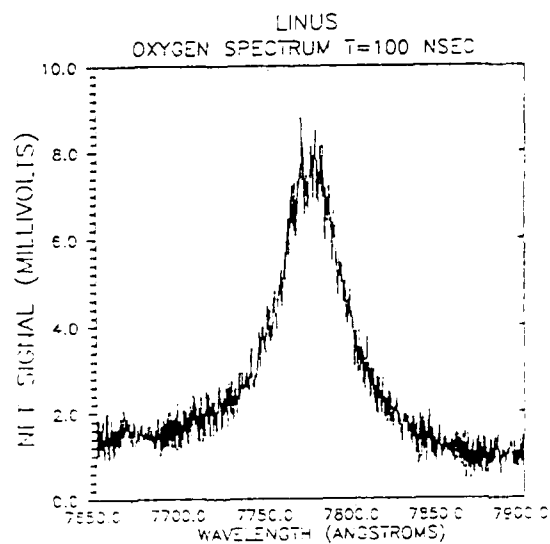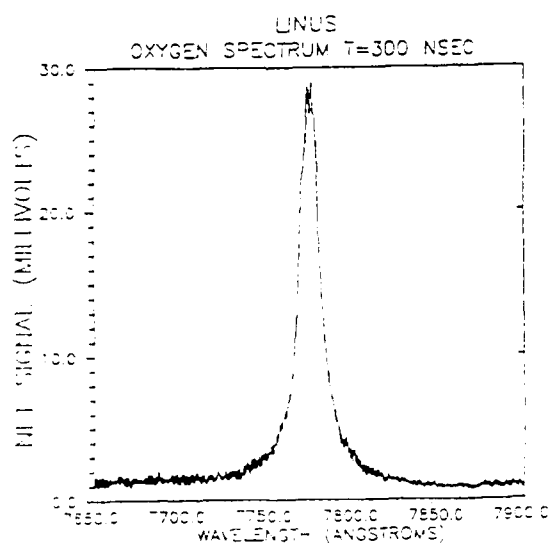
Figure III.4. LINUS OI 7774 A emission for specified delay time.
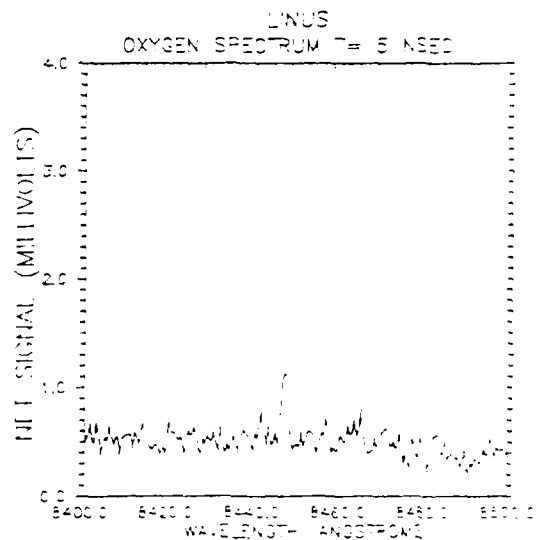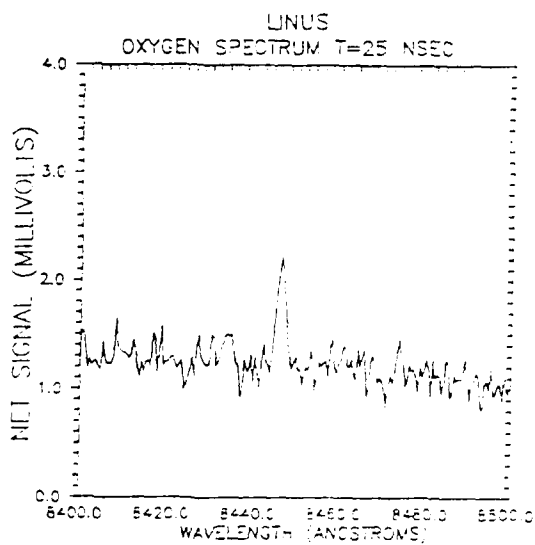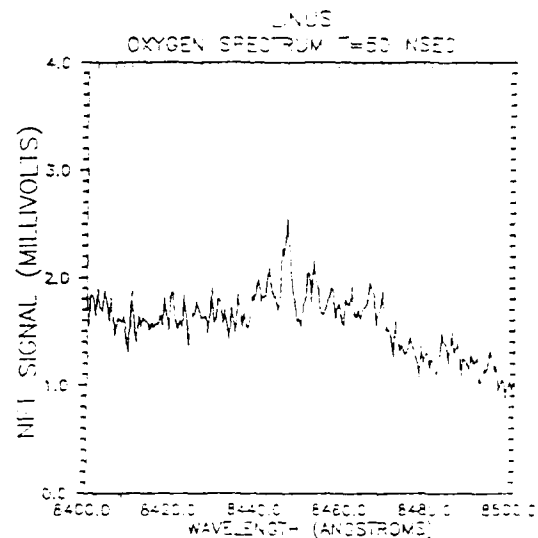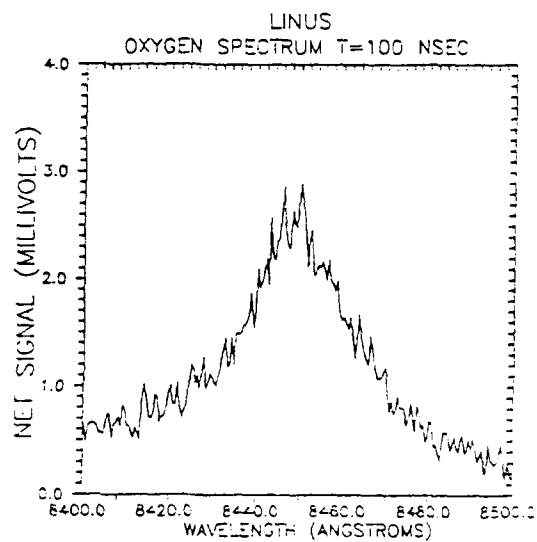
Figure III.5. LINUS OI 8446 A emission for specified delay time.

before more definitive conclusions can be drawn. For example, one experiment would be to monitor these transitions as a function of distance from the spark center. If the x-ray/UV excitation hypothesis is indeed correct, then one would still see the narrow lines in the halo region. This unexpected result could potentially lead to a series of interesting experiments on x-ray/UV excitation and deposition from fireballs.

Emissions which have been assigned to O^{4+} transitions have been identified in these experiments. At a delay time of 100 nS, the 5592 A emission shown in Figure III.6 arises from O^{2+} ^1P-$^1P^0$ transition. At 50 nS, a weak line at 5598 A starts to appear. At 25 nS, two sets of weak blended lines near 5582 A and 5598 A are observed on top of the continuum. These line positions and their 16 A separation agree with the position of the multiplet from O^{3+} ^3D-^3P transition as listed in Wiese[12]. In addition, a 5115 A line is observed at 25 nS and 50 nS (weak at this time) which corresponds to the O^{4+} $^1P^0$-^1S transition. From these observations, it appears that O^{3+} is present in the LINUS plasma at delay times of 25 nS and 50 nS.

A preliminary search for O^{5+} emission has been unsuccessful. There are very few transitions in the visible region for charged states higher than O^{4+}. For O^{5+} the only lines listed in ref. 12 are 4751 A, 5112 A, 5279 A, 5298 A, 5410 A, and 5602 A. The 5279 A line, which has the highest oscillator strength, is not observed in the present experiment. Although lines near 5112 A and 5602 A have been seen (see the above paragraph), they have weaker oscillator strengths than the 5279 A line and thus are more likely emissions from O^{4+}. This conclusion is further supported by the kinetics calculation in Chapter VI which shows that the O^{4+} density is higher than the O^{5+} density at 25 nS and 50 nS. From this discussion, it is clear that more data are required in the 2000 A to 5000 A region and a search should be conducted for charge states higher than O^{4+}.
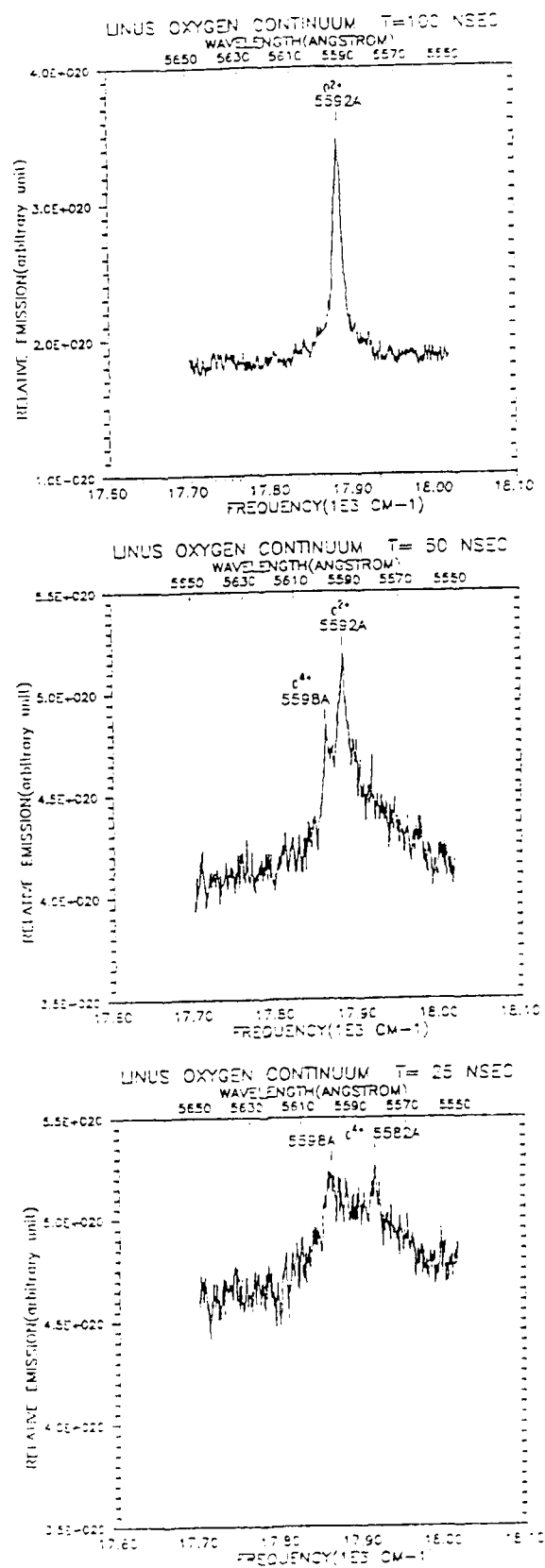
Figure III.6. LINUS oxygen emission near 5600 A for specified delay time illustrating the appearance of O^{2+} and O^{4+} multiplet.

IV. STARK BROADENING

A. GENERAL

In this chapter, we discuss the development of a line broadening code for calculating spectral emission in an oxygen plasma. This section addresses the use of spectral line broadening to determine plasma parameters. In Section IV.B, we describe the theory of Stark broadening applied to LINUS and the validity criteria of the approximations. In Section IV.C, the results of validation, benchmark, and comparison with experiments are presented.

The analysis of spectral lineshapes is commonly used to determine values for plasma parameters such as electron density, electron temperature, and electronic temperature. The lineshape intrinsically contains information on the interaction between the emitter and surrounding particles in the plasma environment. The dominant mechanism of line broadening in most plasmas is pressure broadening by charged particles, also known as Stark broadening. Previous work on line broadening has demonstrated Stark broadening to be a useful diagnostic for determining plasma parameters in the electron density range of 10^{14} to 10^{18} cm^{-3}[13]. The accepted standard for determining electron density is the H_β line of hydrogen (4861 A) and some lines in He^+ (3203 A, 4686 A). An accuracy of 5% to 20% for the electron density can be expected depending on the choice of lines used and the range of electron density. An important result from past work is that Stark broadening is relatively insensitive to electron temperature. This implies that while Stark broadening can be used to determine plasma parameters for systems not in local thermodynamic equilibrium (LTE), it cannot determine accurately the value for electron temperature. For example, the electron widths for most OI lines in Griem's table[14] show a change of less than a factor of two as the electron temperature varies from 5000 K to 40000 K.

In order to use Stark broadening for obtaining plasma parameters, one may either compare experimental and calculated lineshapes or compare experimental linewidths with those from previously studied lines with known plasma parameters. The advantage of calculating lineshapes for a wide range of wavelengths is that values for the electronic temperature, determined by relative level populations of the emitting species, may be obtained. The advantage of a linewidth comparison is that tables of calculated linewidths exist for many species as a function of electron density and temperature. For either lineshape or linewidth comparison, the

29

experimental data should be calibrated, instrument and opacity corrected, and Abel inverted before making the comparison[13].

The LINUS experimental line emission data for oxygen plasmas[15] show the presence of broad and narrow OI IR lines accompanied by small shifts. These IR lines arise from high-lying Rydberg states formed from plasma recombination processes. Figure IV.1 is a simplified Grotrian diagram illustrating the major IR transitions for atomic oxygen. For a 110 torr plasma at a delay time of 6 μS, the narrow lines typically have a full width half maximum (FWHM) of about twice the instrument resolution. The broad lines (e.g. 4 μm and 7.5 μm) have FWHM of about 5-7 times the instrument resolution. This observation suggests that if Stark broadening is found to be the dominant broadening mechanism in the LINUS plasma, it may be a useful diagnostic tool for LINUS data analyses. For application to LINUS, lineshape calculations are necessary since the linewidths of the OI infrared lines of interest are not listed in Griem's tables[14] and few experimental measurements exist. Therefore, the Stark line broadening code has been developed to:

1. characterize the broadening mechanisms giving rise to LINUS spectral lineshapes;

2. determine values for electron density, electron temperature, and electronic temperature;

3. predict line positions and intensities to guide future LINUS data acquisition in the MWIR and LWIR.

4. develop a basis for applying the LINUS data to understanding atmospheric plasma effects of nuclear weapons.

B. THEORY

1. GENERAL DISCUSSION

The general theory of atomic lineshape and linewidth has been widely studied and can be found in many spectroscopic texts (for example, see refs. 16 and 17). The present treatment of Stark broadening is based primarily on the theory of Griem[14] and that of Anderson[18].

The contribution to plasma linewidths arise from natural, Doppler, and collisional broadening. For most plasmas, natural broadening, which

30

SIMPLIFIED OI GROTRIAN DIAGRAM
(TRIPLET AND QUINTET SYSTEMS)
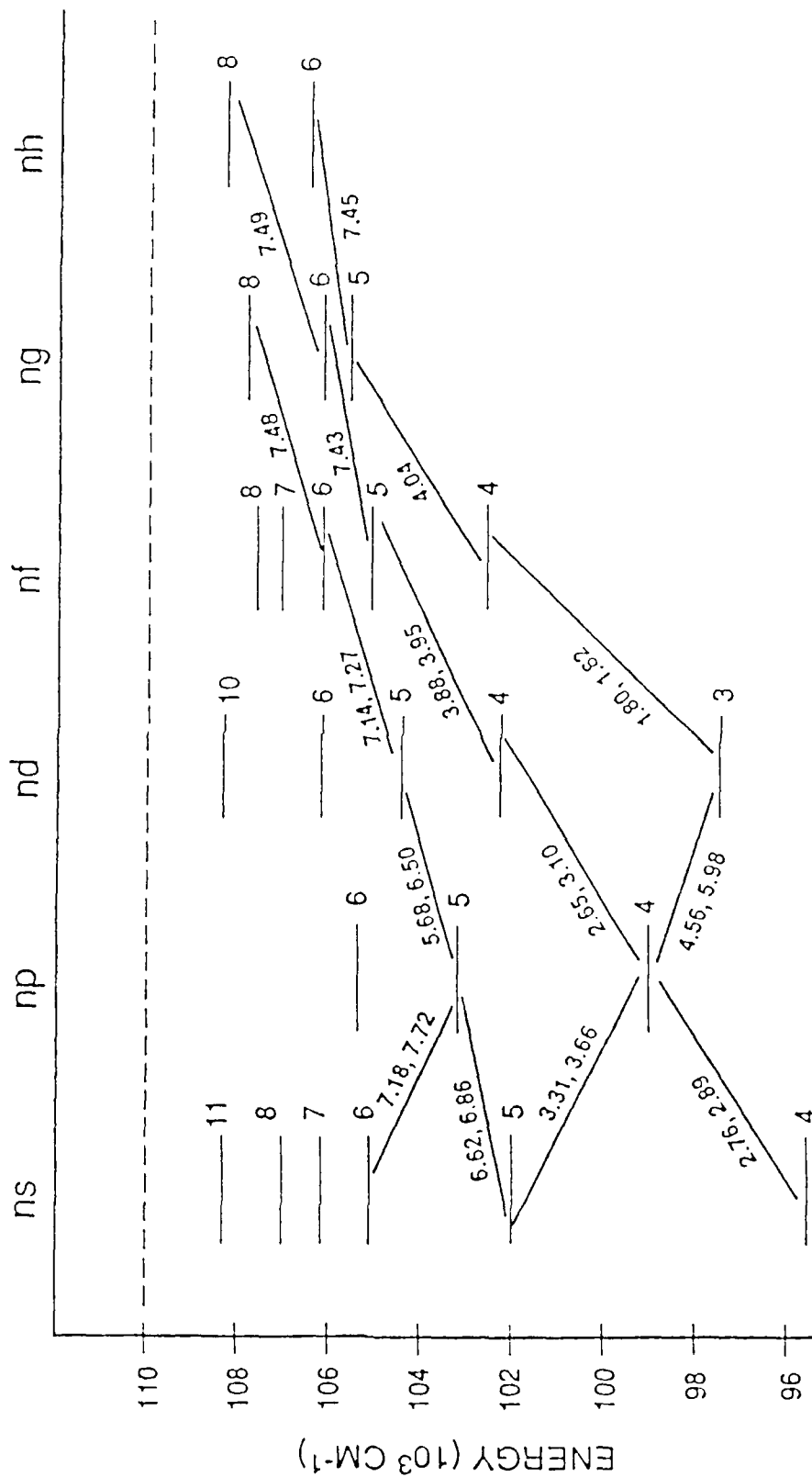
Figure IV.1. A simplified Grotrian diagram for OI illustrating the major IR transitions.

results from the Heisenberg uncertainty principle, is negligible. The importance of Doppler broadening is dependent on the experimental conditions. For the LINUS experiment, the Doppler width of an oxygen atom with a temperature of 10^6 K and a wavelength of 25 μm is 0.0045 μm. Under these conditions, the Doppler width is an order of magnitude smaller than the LINUS instrument resolution and can also be neglected. The dominant broadening mechanism in a plasma is usually Stark broadening because the emitters are subject to large effects from instantaneous local fields of the surrounding ions, and to collisional interactions with electrons.

Stark line broadening problems are frequently solved by treating ions in the quasistatic approximation and electrons in the impact approximation. The quasistatic approximation assumes that the motion of the ions are essentially stationary. This is valid if the splitting caused by the ion field, $\Delta\omega$, is large compared to the inverse ion collision time, $1/\tau_i$, or

$$\Delta\omega\tau_i \gg 1 \ . \tag{IV.1}$$

The collision time may be estimated by b_i/v_i where v_i is the velocity of the ion and b_i is the impact parameter. The impact parameter is given by[17]

$$(4\pi/3)Nb_i^3 \sim 1 \ . \tag{IV.2}$$

Once the ion density and temperature have been determined, the validity of using the quasistatic approximation may be verified using eqs. (IV.1) and (IV.2).

Electrons have been shown to have a significant broadening effect for lines which arise from high nl states with large polarizability[14]. The impact approximation assumes that the average collision is weak or that two strong collisions never occur simultaneously. The impact approximation holds in the region surrounding the line center where the distance from line center, $\Delta\omega$, is small compared to the inverse of the collision duration, τ_e, i.e.

$$\Delta\omega < 1/\tau_e \approx v_e/b_e \tag{IV.3}$$

where v_e is the velocity of the electron and b_e is the impact parameter. For long range Coulomb interactions, b_e may be approximated by the Debye length, λ_D. Therefore, eq. (IV.3) may be reduced to

$$\Delta\omega \leq \omega_{pe} \tag{IV.4}$$

where ω_{pe} is the electron plasma frequency, $(4\pi N_e e^2/m_e)^{1/2}$ (rad/sec). For example, if N_e is 10^{16} cm^{-3}, then the electron plasma frequency is 9.E11/sec. For emission at 4 μm, the impact approximation for electron broadening holds in the range 3.95 μm to 4.05 μm. Similarly, the impact approximation holds for ions in the region

$$\Delta\omega < \omega_{pi} << \omega_{pe} \qquad\qquad\qquad (IV.5)$$

where ω_{pi} is the ion plasma frequency.

2. ION BROADENING - APPROACH

The use of the quasistatic approximation for the ions is equivalent to representing the ions by a distribution of static electric fields which is dependent on the ion density and temperature. By adopting this physical picture for the ions, the standard quantum mechanical theory for Stark effect is applicable. To calculate the effect of the static field, one first defines the Stark Hamiltonian matrix for the system and subsequently diagonalizes this matrix for generating eigenvalues and eigenfunctions. The matrix diagonalization routines, based on Jacobian transforms, are taken from Press[19]. These routines have been checked by comparison with manually-calculated eigenvalues and eigenfunctions for 2x2 and 3x3 matrices. The basis set assumes ℓ-s coupling and is defined by s, the spin, n, the principal quantum number, ℓ, the orbital angular momentum, and m_ℓ, the magnetic quantum number.

The Stark Hamiltonian, H', is a product of the electric dipole moment, er, and electric field, F, i.e. H'=erF. The selection rules, which are identical to those for electric dipole induced transitions, are $\Delta s=0$, $\Delta\ell=+1,-1$, $\Delta m_\ell=+1,0,-1$. For all atoms except hydrogen, the presence of the Stark field removes the degeneracy of the m_1 magnetic substates with the amount of energy shifted being proportional to m_ℓ^2. Because of this dependence, the quadratic Stark effect gives rise to asymmetry in lineshape. In addition, lines arising from the split magnetic states are shifted and broadened. Furthermore, lines forbidden by the electric dipole selection rules emerge due to mixing of states.

Characterizing the temporal dependence of the ion field in a plasma is difficult both experimentally and theoretically. The accepted approach is to statistically simulate the effect of the quasistatic ions by a plasma microfield distribution. Using this approach, a microfield distribution has been calculated by Baranger and Mozer[20]. Hooper[21,22] refined the

33

theory by including correlation among all perturbers and allowing independent input for electron and ion density and temperature. The microfield distribution used in our line broadening code is calculated from Hooper's code[23]. Figures IV.2,3 show the low frequency electric microfield distribution at a neutral point for a series of electron density and temperature. Plotted is the probability as a function of ϵ, where $\epsilon=F/F_c$, the ratio of the field to the Holtsmark normal field[24], $F_0=2.603eN_e^{2/3}$.

The input for the Hamiltonian matrix is as follows. The diagonal matrix elements of the Hamiltonian are the zero field energy levels for oxygen atom. Most of the energy levels are taken from Moore[25]. For states not listed in Moore, the energy levels are calculated using polarization theory[26]. The off-diagonal matrix elements, which are the Stark Hamiltonian matrix elements, are calculated by multiplying the plasma field $(F=\epsilon F_0)$ by the dipole moment matrix elements. The dipole moment matrix elements consist of a radial and an angular part. The radial part is obtained from the calculations of Lin[27] which employ a frozen core representation of the oxygen wavefunctions. For transitions higher than $\ell'=5\rightarrow\ell''=4$, the radial matrix elements are calculated from the tables in ref. 28. The signs of these matrix elements may differ from those of Lin depending on whether n'-n" is even or odd. Formulas for the angular component, consisting of direction cosine matrix elements, can be found in ref. 29.

With the full Hamiltonian matrix defined, matrix diagonalization results in perturbed energy levels and wavefunctions which are field-dependent. After calculating the energy levels and wavefunctions for a particular field, the line intensity is weighted by the probability of occurrence of that field.

3. ELECTRON BROADENING APPROACH

To account for electron broadening, Anderson's theory for pressure broadening[18] is used. Collisional broadening theories before Anderson's are mostly based on Weisskopf's[30] treatment of collisions as changing the phase of the emitted wavetrains. These theories invoke the impact approximation, classical path assumption, and adiabatic approximation. The classical path assumption means that the trajectory for the electron is straight if emitters are neutrals and hyperbolic if they are charged. The adiabatic approximation assumes that collisions do not induce transitions among close-lying states of the emitting atom.
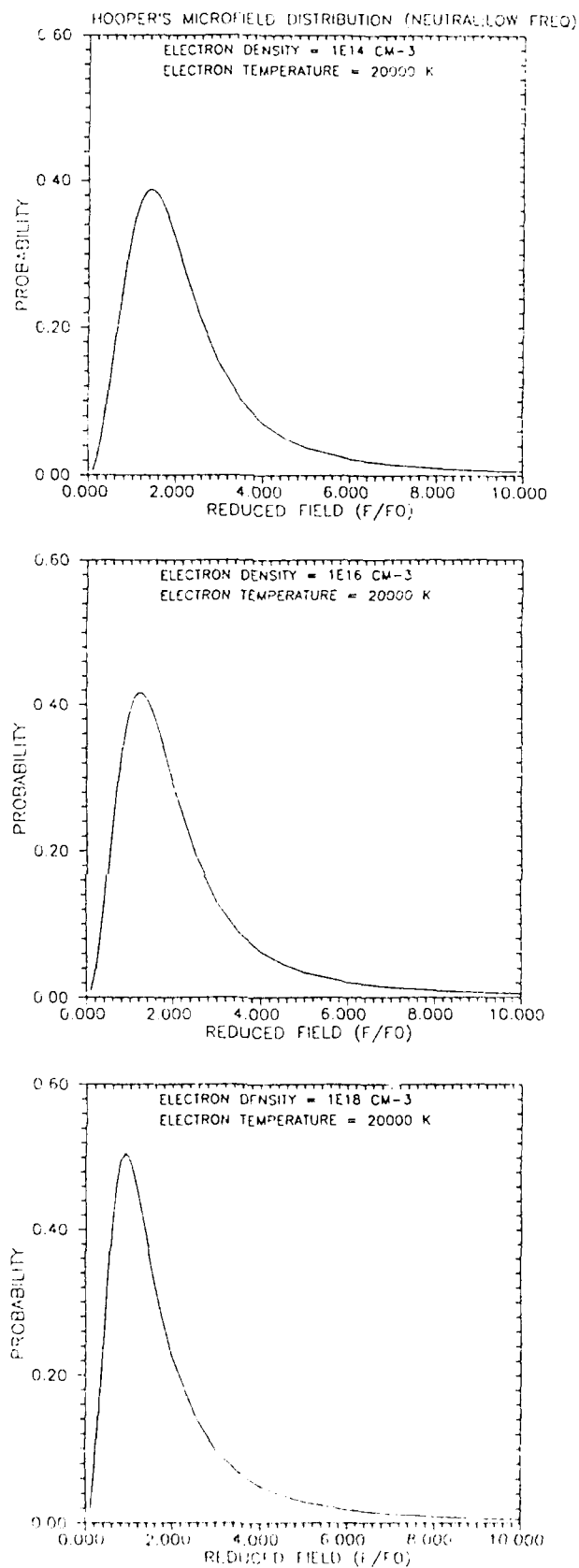
Figure IV.2. Hooper's electric microfield distribution at a neutral point as a function of electron density.
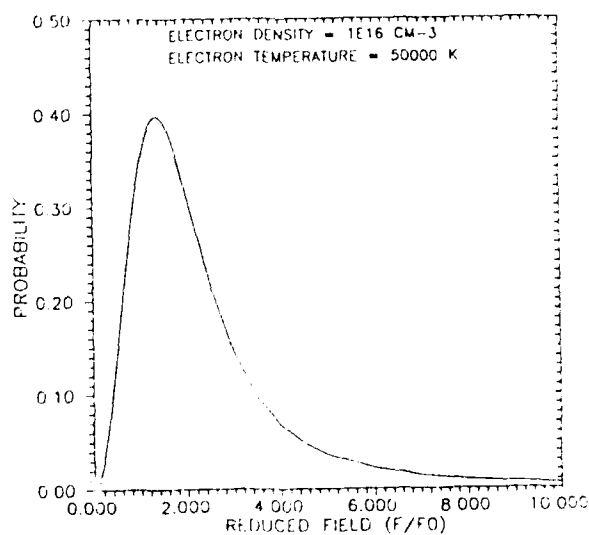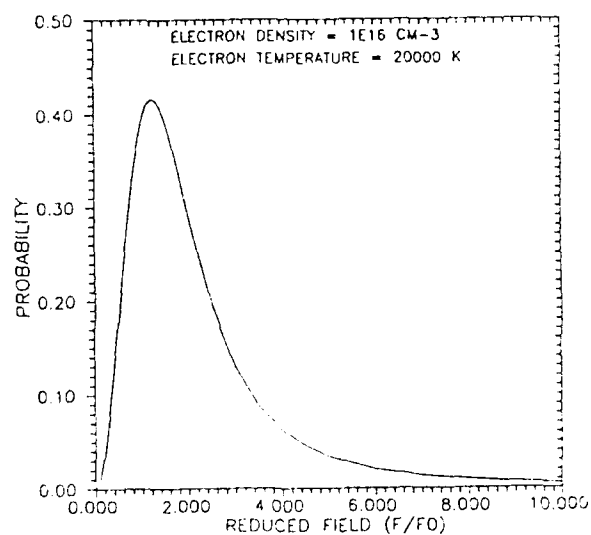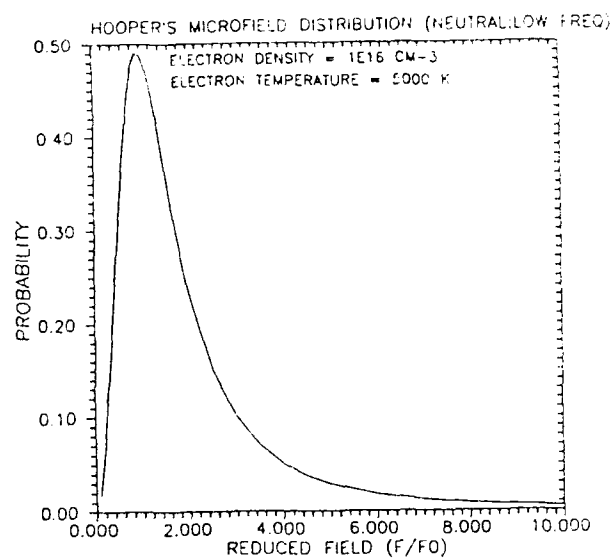
Figure IV.3. Hooper's electric microfield distribution at a neutral point as a function of electron temperature.

Anderson refined the impact theory by removing the assumption of adiabatic collisions. His theory specifically addressed inelastic collisions which, especially for electrons, have a significant contribution to linewidths. He used the impact approximation, classical path, and the assumption of degenerate states. After the work by Anderson, Baranger[31] and Griem[14] independently derived equations for broadening in a plasma in the semi-classical and quantum-mechanical formalisms. Griem and his coworkers removed the assumption of degenerate states and treated the problem of overlapping lines, i.e., lines arising from levels which are greatly broadened by electrons so that adjacent levels are blended. Because of the removal of the degeneracy assumption, Griem's theory is more accurate than Anderson's but considerably more complicated. Griem carried the work further by applying his theory to study broadening effects in hydrogen and helium plasmas. In addition, he tabulated the calculated widths and shifts for many atoms and ions in terms of the broadening parameters.

For application to the LINUS line broadening problem, Anderson's method is used because his approach is quite general and tractable and more physically intuitive. The test of his method lies in comparing the calculated spectra using one set of plasma parameters with experimental data over a wide spectral range. If the comparison results in disagreement which is within the uncertainty in the experimental data, then it is not necessary to use the more refined theory by Griem. The details of Anderson's theory are first discussed. The application of his theory to LINUS will then be presented.

The electron broadened halfwidth, $\Delta\nu$, is related to the electron collision cross section, σ, by

$$\Delta\nu \ (cm^{-1}) = (N_e v/2\pi c)\sigma \ , \tag{IV.6}$$

where N_e = electron density,
v = average electron velocity = $(8kT_e/\pi m_e)^{1/2}$.

The cross section may be calculated from

$$\sigma = \int_0^\infty 2\pi b S(b)db \ , \tag{IV.7}$$

where b is the impact parameter and S(b) is a weighting factor of the probability that electron collision interrupts the radiation. For strong collision, when b is small, S(b) may be defined to be unity. For large b, S(b) is given by a term $S_2(b)$ which gives the probability of a transition being caused by a collision. The problem reduces to the calculation of S_2, given by

$$S_2(b) = (1/2) \left[\sum_{m_i} \frac{|<im_i|P^2|im_i>|}{2\ell_i+1} + \sum_{m_f} \frac{|<fm_f|P^2|fm_f>|}{2\ell_f+1} \right] , \quad (IV.8)$$

where $|i>=|n_i\ell_i>$ and $|f>=|n_f\ell_f>$.

Inserting the identity $\sum_{n'\ell'm'} |n'\ell'm'><n'\ell'm'|=1$ into eq. (IV.8),

$$S_2(b) = (1/2) \left[\sum_{m_i} \sum_{n_i'\ell_i'm_i'} \frac{|<n_i\ell_i m_i|P|n_i'\ell_i'm_i'>|^2}{2\ell_i+1} \right.$$

$$\left. + \sum_{m_f} \sum_{n_f'\ell_f'm_f'} \frac{|<n_f\ell_f m_f|P|n_f'\ell_f'm_f'>|^2}{2\ell_f+1} \right] . \quad (IV.9)$$

The P matrix element is given by

$$<a|P|b> = (1/\hbar) \int_{-\infty}^{\infty} \exp(i\omega_{ab}t) <a|H_1(t)|b>dt , \quad (IV.10)$$

where t is time, ω_{ab} is the transition frequency, and H_1 is the interaction Hamiltonian. The states $<a|=<n\ell m|$ and $|b>=|n'\ell'm'>$ are the wavefunctions of the radiator.

To apply the model to the LINUS problem, the perturbation Hamiltonian is assumed to be

$$H_1 = -e^2/r_c + e^2/r , \quad (IV.11)$$

38

where the first term is the Coulomb attraction between the perturbing electron and the oxygen nucleus separated by $|r_c|$ and the second term is the Coulomb repulsion between the perturbing electron and the emitting electron separated by $|r|$. Vector quantities are represented in boldface.

Using the cosine law, the distance r may be further expressed in terms of r_c, r_a (radial vector between emitting electron and oxygen nucleus), and γ (angle between the vector from nucleus to emitting electron and the vector from nucleus to colliding electron). This results in the equation

$$H_i = \frac{-e^2}{r_c} + \frac{-e^2}{(r_c^2 - 2r_a r_c + r_a^2)^{1/2}} .$$ (IV.12)

All the parameters are illustrated in Figure IV.4.
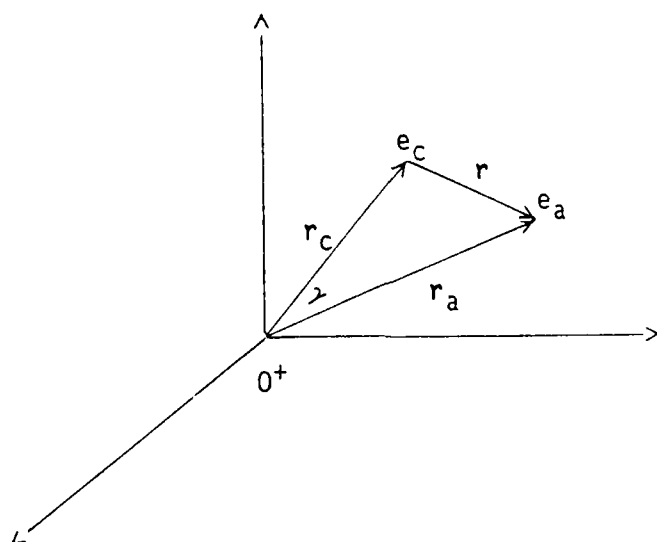
Figure IV.4. Illustration of parameters in the interaction Hamiltonian.

By expanding the second term in eq. (IV.12) in (r_a/r_c) and retaining terms to first order, the interaction Hamiltonian may be simplified to

$$H_1 = e^2 r_a \cos\gamma / r_c^2 . \qquad (IV.13)$$

Next the $\cos\gamma$ term is expressed in spherical polar coordinates,

$$\cos\gamma = \cos\theta_a \cos\theta_c + \sin\theta_a \sin\theta_c \cos(\phi_a - \phi_c) . \qquad (IV.14)$$

Since the electron-atom collision occurs in a plane, the azimuthal angle for the colliding electron, ϕ_c, is set to be zero. The angle, θ_c, is related to the collision parameters by

$$\cos\theta_c = vt/|r_c| \qquad (IV.15)$$

$$\sin\theta_c = b/|r_c| \qquad (IV.16)$$

$$|r_c^2| = b^2 + v^2 t^2 . \qquad (IV.17)$$

The angles, θ_a and ϕ_a, are related to the direction cosines, λ, by

$$\cos\theta_a = \lambda_{za} \qquad (IV.18)$$

$$\sin\theta_a \cos\phi_a = \lambda_{xa} . \qquad (IV.19)$$

By substituting these expressions into eq. (IV.12), the Hamiltonian becomes

$$H_1 = \frac{e^2 r_a}{r_c^3} (\lambda_{za} vt + \lambda_{xa} b) . \qquad (IV.20)$$

The matrix element of H_1 is

$$\langle a|H_1|b\rangle = \frac{e^2vt}{r_c^3} \langle a|r_a\lambda_{za}|b\rangle + \frac{e^2b}{r_c^3} \langle a|r_a\lambda_{xa}|b\rangle$$

$$= \frac{e^2vt}{r_c^3} M_{za} + \frac{e^2b}{r_c^3} M_{xa} \ , \tag{IV.21}$$

where $M_{za} = \langle a|r_a\lambda_{za}|b\rangle$ and $M_{xa} = \langle a|r_a\lambda_{xa}|b\rangle$. Eq. (IV.21) can be used to calculate the matrix element of P as follows:

$$\langle a|P|b\rangle = (1/\hbar)\int_{-t_D}^{t_D} \exp(i\omega_{ab}t)(\frac{e^2vt}{r_c^3} M_{za} + \frac{e^2b}{r_c^3} M_{xa})dt$$

$$= (e^2M_{za}/\hbar)\int \frac{vt}{r_c^3}\exp(i\omega_{ab}t)dt + (e^2M_{xa}/\hbar)\int \frac{b}{r_c^3}\exp(i\omega_{ab}t)dt$$

$$\tag{IV.22}$$

The first integral can be expanded into

$$\int [\frac{vt}{(b^2+v^2t^2)^{3/2}}\cos\omega_{ab}tdt + i\ \frac{vt}{(b^2+v^2t^2)^{3/2}}\sin\omega_{ab}tdt]$$

$$= 2i\int_0^{t_D}\frac{vt}{(b^2+v^2t^2)^{3/2}}\sin\omega_{ab}tdt \ . \tag{IV.23}$$

The first term of the integral does not contribute because its integrand is an odd function of t. Similarly, the second integral in eq. (IV.22) is

$$\int [\frac{b}{(b^2+v^2t^2)^{3/2}}\cos\omega_{ab}tdt + i\ \frac{b}{(b^2+v^2t^2)^{3/2}}\sin\omega_{ab}tdt]$$

$$= 2\int_0^{t_D}\frac{b}{(b^2+v^2t^2)^{3/2}}\cos\omega_{ab}tdt \ . \tag{IV.24}$$

41

Again, the second term may be omitted because its integrand is an odd function of t. Therefore, the P matrix element is simplified to

$$
\langle a|P|b \rangle = (2ie^2 M_{za}/\hbar) \int_0^{t_D} \frac{vt}{(b^2+v^2t^2)^{3/2}} \sin\omega_{ab}t\, dt
$$

$$
+ (2e^2 M_{xa}/\hbar) \int_0^{t_D} \frac{b}{(b^2+v^2t^2)^{3/2}} \cos\omega_{ab}t\, dt \; . \tag{IV.25}
$$

The integration limit, t_D, is calculated from

$$
\lambda_D^2 = b^2 + v^2 t_D^2 \; , \tag{IV.26}
$$

since the Coulomb field is shielded at distances larger than λ_D, the Debye length. Therefore,

$$
t_D = (1/v)(\lambda_D^2 - b^2)^{1/2} \; . \tag{IV.27}
$$

After the computation of the matrix element of the perturbation Hamiltonian, P may be calculated by numerical integration. The expression for P is then substituted into eq. (IV.9) to calculate S_2. To facilitate the treatment of strong collisions, S_2 is calculated from large to small impact parameters. The impact parameter at which S_2 is greater than unity is assumed to be the point where strong collisions take over. Below this impact parameter, S_2 is set to unity.

To summarize, the necessary steps to obtain the linewidth for one transition are:

a. Calculate the P matrix element at a certain electron velocity for a particular impact parameter. Romberg integration is used to compute the two collision integrals in eq. (IV.25).

b. Calculate S_2 from eq. (IV.9) by performing the summation over the perturbing states for both the initial and final states of the transition.

c. Repeat steps a and b for a series of impact parameters giving S_2 as a function of b. To obtain 10% precision in the linewidth, one needs to use a minimum of 50 impact parameters. Typically, the use of 200 impact parameters results in about 1% precision.

d. Calculate the collision cross section from eq. (IV.7) by numerical integration from 0 to λ_D.

e. Calculate the linewidth from eq. (IV.6).

In calculating the electron widths, the unperturbed case means that ion-unperturbed wavefunctions and energy levels are used to compute the S_2 matrix elements. In this case, the calculations are performed for transitions between two n, ℓ states. For the semi-perturbed case, unperturbed wavefunctions and ion-perturbed energy levels are employed. For the perturbed case, ion-perturbed wavefunctions and energy levels are used. For both the semi-perturbed and perturbed cases, the calculation of S_2 is performed for transitions between two n, ℓ, m states and omits the summation over m_i and division by $2\ell_i+1$.

4. LINESHAPE

The lineshape for an isolated line broadened by electrons is assumed to be a Lorentzian function, valid when the electrons can be described classically by a damped oscillator. Normalized to area, the Lorentzian function is

$$L(\nu) = \frac{w}{4(\nu-\nu_0)^2+w^2} \tag{IV.28}$$

where ν is the frequency, ν_0 is the transition frequency, and w is the full electron width.

The intensity, $I(\nu)$, of a line is given by

$$I(\nu) = N_{rel} \ A \ h\nu_0 \ L(\nu) \tag{IV.29}$$

43

where N_{rel} is the relative population (assumed to be Boltzmann), A is the Einstein A coefficient. The unit of I is watts/cm^3-cm^{-1}. In order to obtain spectral radiance, S(ν), one multiplies I(ν) by a pathlength of 1 cm and divides by a solid angle of 4π sr. Then S(ν) has the units of watts/cm^2-sr-cm^{-1}. In order to calculate S(λ) from S(ν), one divides the latter by λ^2. This results in a unit of watts/cm^2-sr-μm for S(λ), the proper quantity to compare with experimental data.

The calculated spectral radiance containing ion and electron broadening is convolved with the instrument resolution function of the monochromator. For a grating blazed at 6 μm and a monochromator slit width of 3 mm, the instrument resolution, $\Delta\lambda$, in μm is[32]

$$\Delta\lambda = -0.00176\lambda + 0.0426 . \qquad (IV.30)$$

The instrument-corrected lineshape is calculated by convolving the ion- and electron-broadened lineshape with a triangular slit width function usually assumed for a spectrometer with the same entrance and exit slitwidths. An area normalization is used for the triangle. The final output of the code is represented by spectral radiance as a function of wavelength.

C. RESULTS AND LINUS COMPARISONS

This section contains the results of the code validation, benchmark calculation, and comparison with LINUS data. While the latter two activities also serve as a validation of the code, the first one specifically addresses a comparison with a well-characterized plasma experiment and with an independent calculation.

1. VALIDATION

To validate the Stark code, two comparisons are made: (1) against Assous' experimental data with derived plasma parameters[33] and (2) against an independent calculation by Conner and Lin[34]. Other possible validations are against H, He experimental data and calculations[14] and O data from other work[35,36].

Experimental spectra were acquired by Assous[33] in an inductively-heated oxygen plasma. This experiment is relevant to the present work in that measurements of OI emission were made in the IR region and plasma parameters were determined. The digitized results for the OI 1.80 μm

44

(S=2 4f-3d) and 1.82 μm (S=1 4f-3d) lines are shown in Figure IV.5. The sharp peak on the red side of the 1.80 μm line is a reference line. These lines have been shifted by an amount equal to the difference between Assous' and our zero field line positions. From measurements of the linewidth of the H_β line, an electron density of 2.9×10^{16} cm^{-3} was obtained. Using this value of N_e in the Saha equation, the temperature was given as 11400 K. Based on this set of plasma parameters, our calculations at 1.80 μm and 1.82 μm are shown in Figures IV.6 and IV.7 for the unperturbed and semi-perturbed cases, respectively. The calculated spectra assume no instrument resolution and are generated using 7 basis states - 4s, 5s, 4p, 5p, 3d, 4d, and 4f. It is seen that the observed and calculated spectra at 1.82 μm agree well for the unperturbed case. For the 1.80 μm line there is a small difference in the line positions and the semi-perturbed case gives better agreement for the linewidth. The comparison is reasonable when one considers that the instrument resolution, baseline, and relative intensity of the lines are unclear in the experimental spectra displayed in the paper.

To compare the results from the present code with an independent calculation by Conner and Lin[34], OI calculations were performed from 5.5 μm to 8.5 μm using 31 basis states. The basis states and Conner's unperturbed energy levels for spins of 1 and 2 are listed in Table IV-1.

The calculations followed Conner's bundled approach for broadening by ion only, electron only, and ion+electron. The bundled scheme means that only certain close-lying states are allowed to interact with one another. The advantage of this method is that the runtime is considerably decreased. The grouping of the states is shown in the fourth column of Table IV-1; only states with the same group number can perturb one another. The conditions chosen were $N_e=2 \times 10^{16}$ cm^{-3}, $T_e=20000$ K, and $T_{el}=5000$ K. Figures IV.8 and IV.9 show, respectively, the calculations by Conner and Lin and the present code. The comparison is excellent for both zero field and ion only. However, for both the electron only and ion+electron calculations, Conner and Lin's result is narrower at 7.5 μm. The cause of this difference is not known yet. A comparison will be made of the numerical values for the line positions and electron widths from 7 μm to 8 μm to help resolve this discrepancy.

It should be noted that the instrument resolution in these calculations was not incorporated by convolving with a triangle but is simply added to the electron width in the Lorentzian expression. In addition, the abscissa in these plots is labeled relative intensity and
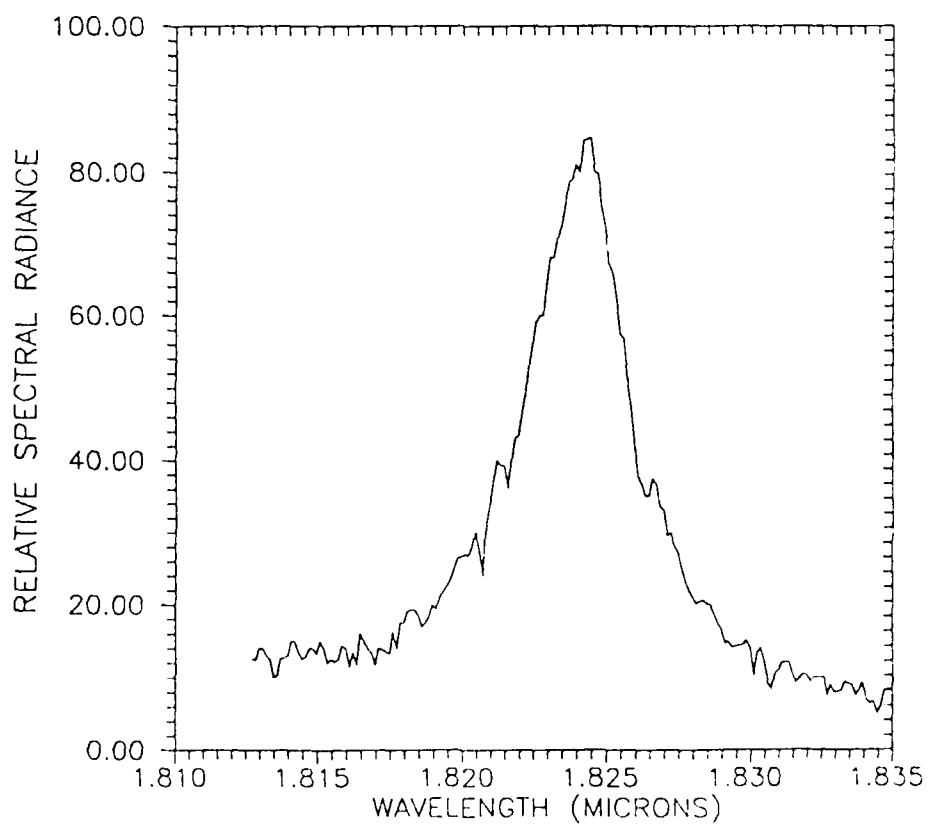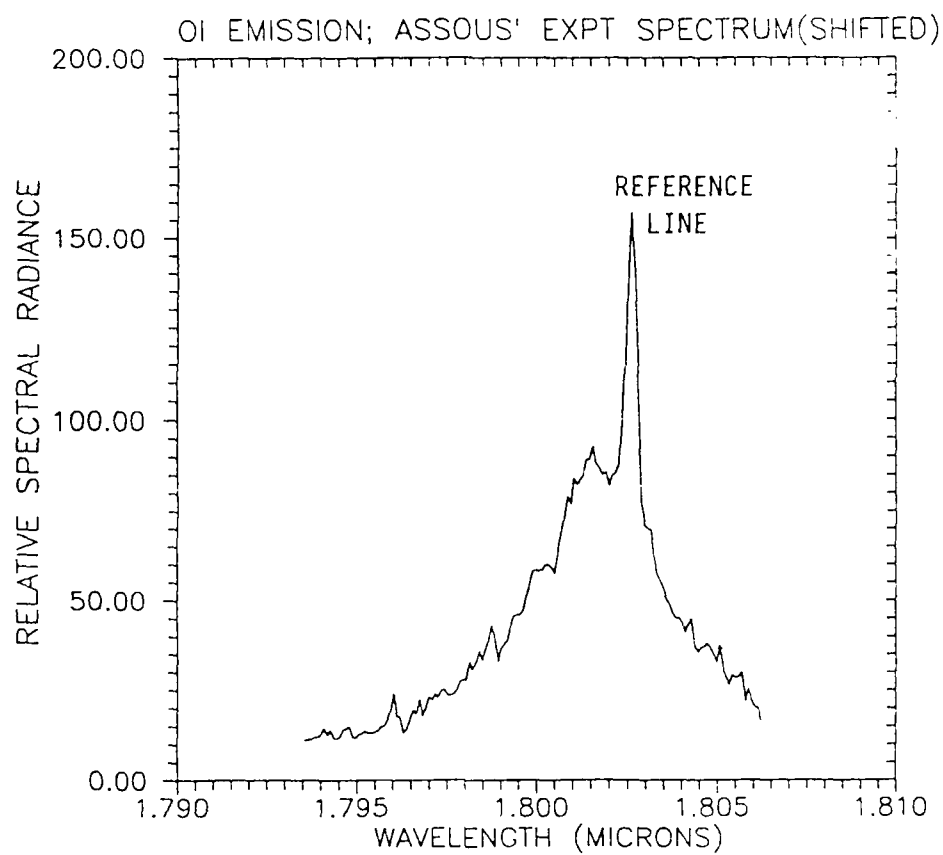
Figure IV.5. Assous' experimental OI spectra at 1.80 μm and 1.82 μm.
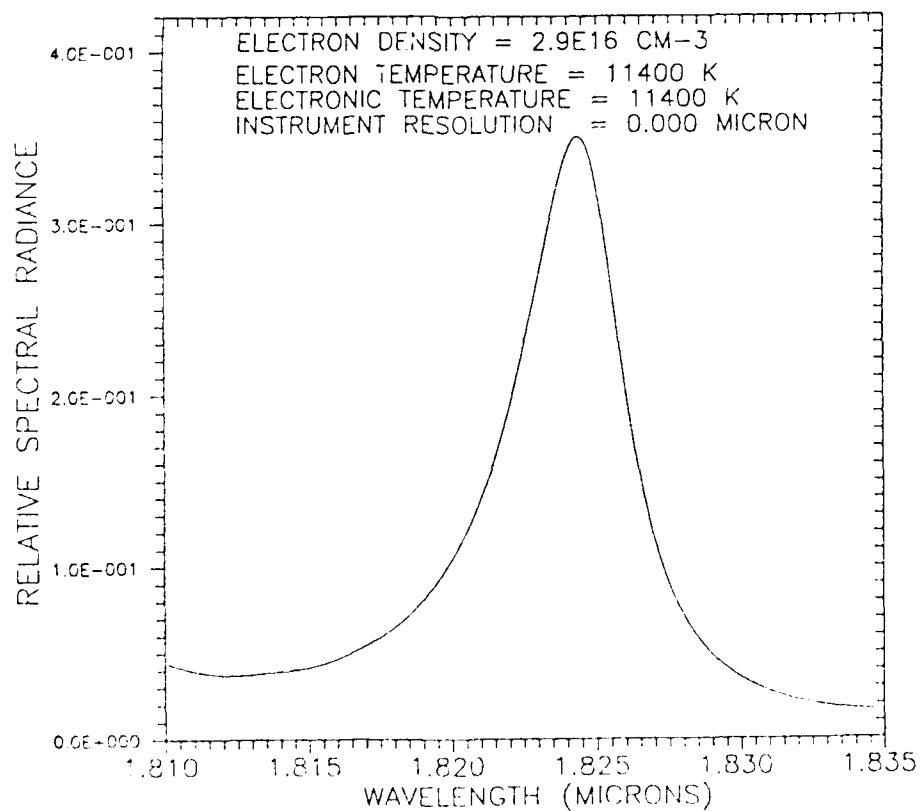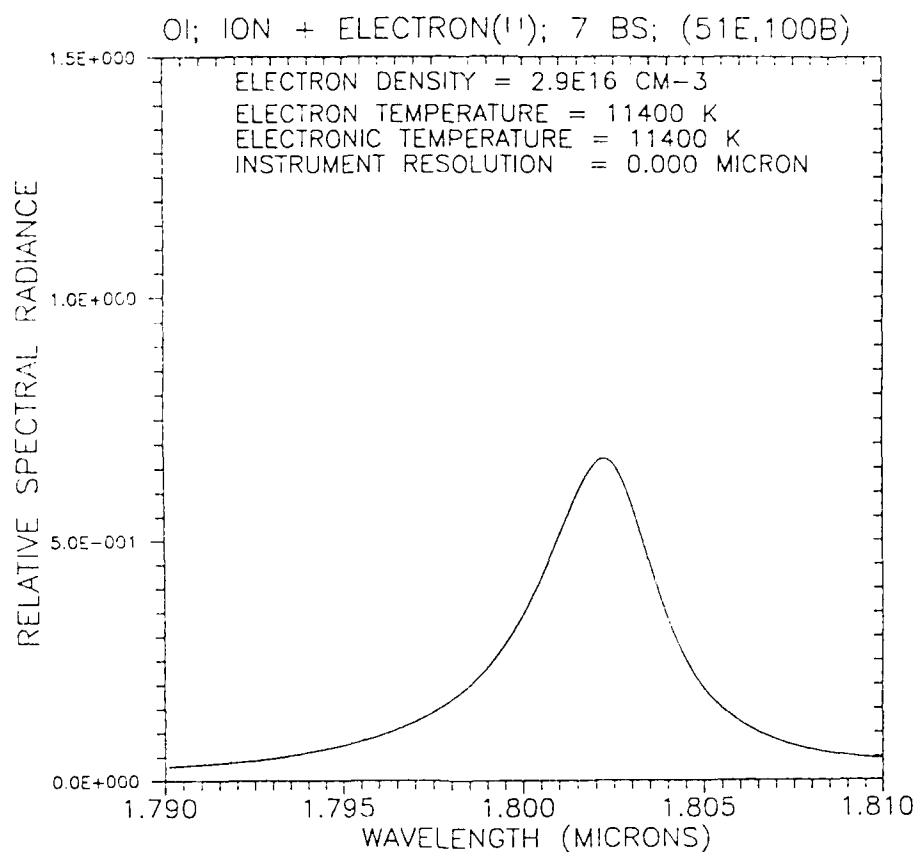
Figure IV.6. Calculated OI spectra at 1.80 μm and 1.82 μm using the unperturbed method when $N_e=2.9 \times 10^{16}$ cm^{-3}, $T_e=T_{el}=11400$ K.

OI; ION + ELECTRON(SP); 7 BS; (51E,50B)

ELECTRON DENSITY = 2.9E16 CM-3
ELECTRON TEMPERATURE = 11400 K
ELECTRONIC TEMPERATURE = 11400 K
INSTRUMENT RESOLUTION = 0.000 MICRON
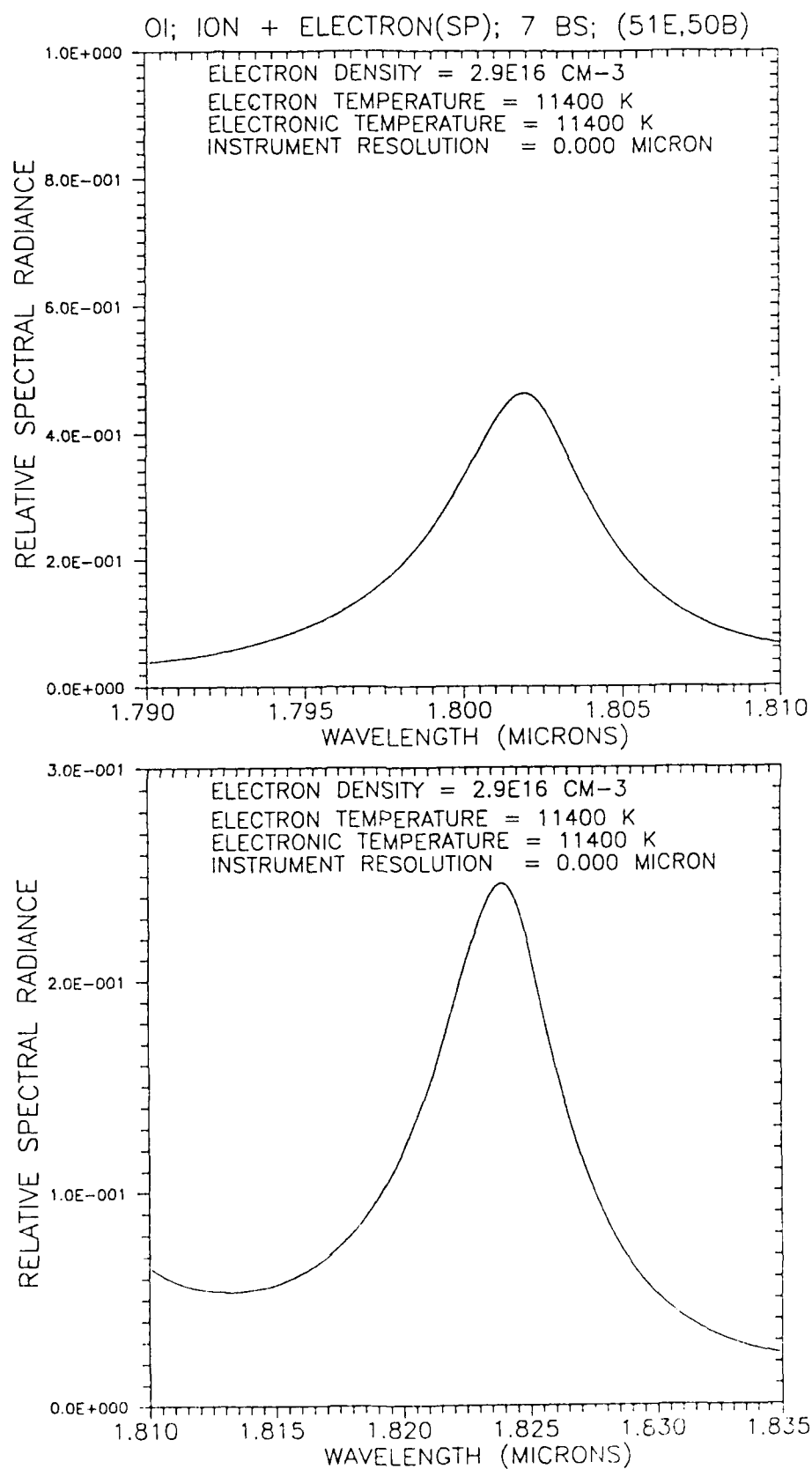
Figure IV.7. Calculated OI spectra at 1.80 μm and 1.82 μm using the semi-perturbed method when $N_e = 2.9 \times 10^{16}$ cm^{-3}, $T_e = T_{el} = 11400$ K.

TABLE IV-1.

Basis Set for Comparison with Conner's Bundled Stark Calculations

n	ℓ	$E_0(S=1)$ (cm^{-1})	$E_0(S=2)$ (cm^{-1})	Group #
8	7	108122.03	108122.03	6
8	6	108122.00	108122.00	6
7	6	107596.	107596.00	5
8	5	108121.	108121.00	6
7	5	107595.9	107595.90	5
6	5	106788.66	106788.66	4
8	4	108120.	108119.00	6
7	4	107595.6	107595.60	5
6	4	106788.65	106788.65	4
5	4	105447.3838	105447.3835	3
8	3	108118.	108115.00	6
7	3	107595.147	107595.140	5
6	3	106785.201	106785.160	4
5	3	105441.724	105441.645	3
4	3	102968.343	102968.249	2
8	2	108114.0	108106.08	6
7	2	107582.777	107573.487	5
6	2	106765.803	106751.4622	4
5	2	105409.008	105385.385	3
4	2	102908.420	102865.562	2
3	2	97488.489	97420.748	1
8	1	107785.	107739.2	5
7	1	107073.5	107002.	4
6	1	105912.031	105788.684	3
5	1	103870.0196	103626.273	2
4	1	99681.051	99094.065	1
8	0	107497.224	107446.036	5
7	0	106627.934	106545.354	4
6	0	105165.232	105019.307	3
5	0	102411.995	102116.698	2
4	0	96225.049	95476.728	1
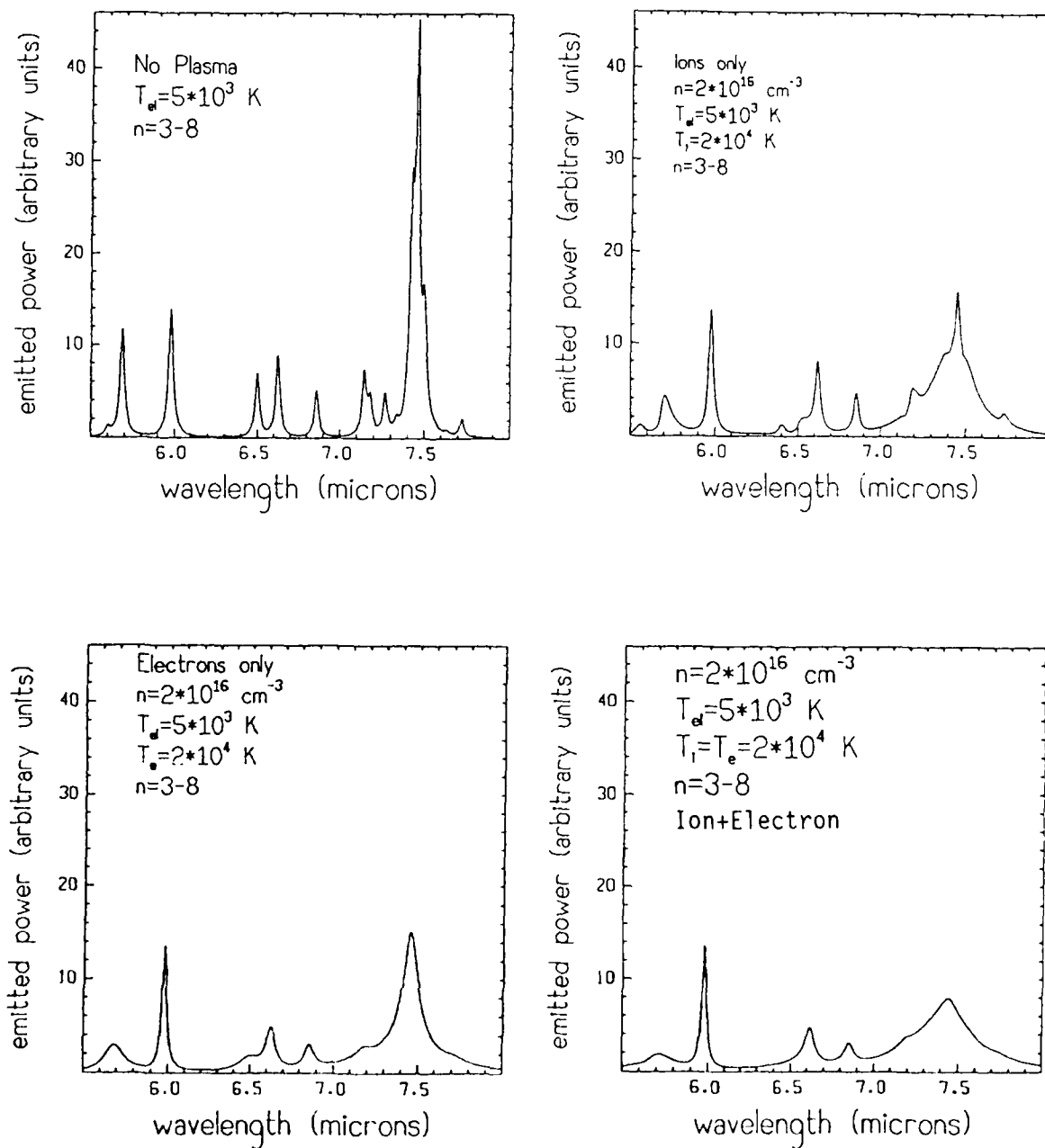
Figure IV.8. Conner's calculated OI spectra from 5.5 μm to 8.0 μm for zero field, ion only, electron only, and ion+electron when N_e=2x10^{16} cm^{-3}, T_e=20000 K, and T_{el}=5000 K.
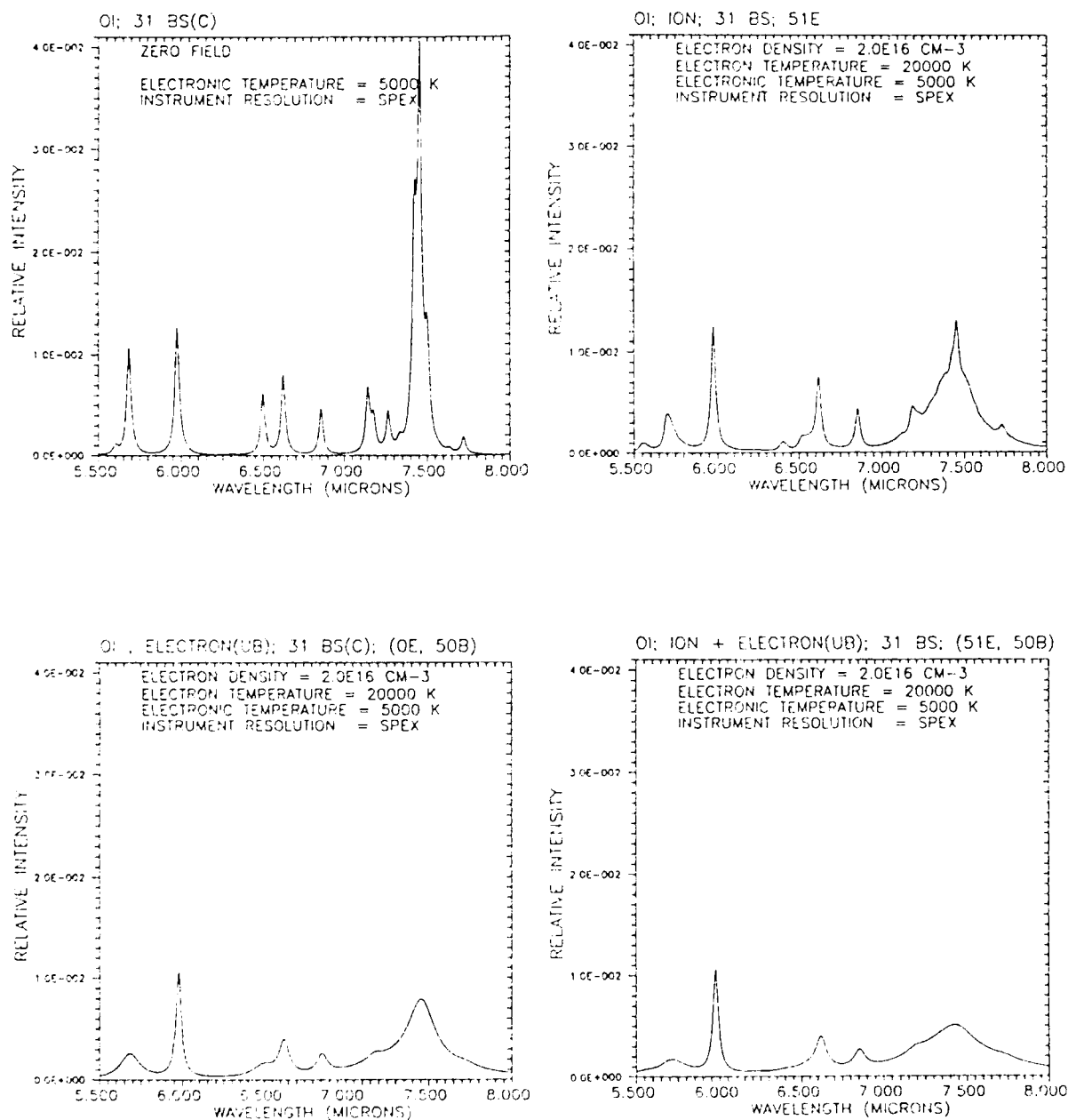
Figure IV.9. Present calculated OI spectra from 5.5 μm to 8.0 μm for zero field, ion only, electron only, and ion+electron when $N_e=2\times10^{15}$ cm^{-3}, $T_e=20000$ K, and $T_{el}=5000$ K.

emitted power because they have not been converted to spectral radiance in the wavelength unit. Hence, these plots can only be compared with one another and should not be compared with experimental data.

2. BENCHMARK

The purpose of the benchmark calculation is two-fold: first, to act as a validation of the code, i.e. verify the expected trend when values for the plasma parameters (electron density, electronic temperature, and electron temperature) are varied. Second, to provide a series of calculations to compare against when the code is being optimized for runtime efficiency or when the code is transported to a different machine.

Calculations have been performed for OI emission from 5.5 μm to 8.0 μm for a series of electron densities and temperatures. All the calculations use 31 basis states (listed in Table IV-2), 51 electric field samplings of the ion microfield distribution, and 50 impact parameters for calculating the electron widths. The origin of the energy levels listed in Table IV-2 has been discussed in Section IV.B.2. All states, unless forbidden by the selection rules, can perturb one another. The electron widths were calculated using unperturbed energies and wavefunctions.

Figure IV.10 shows the results of the calculations when the electron density is varied from zero to 10^{18} cm^{-3} with T_e=20000 K and T_{el}= 5000 K. Broadening is observed to be unimportant until the electron density is above 10^{14} cm^{-3} in the spectral region between 5.5 μm and 8.0 μm. The result shows that the lines become broader when the electron density is increased, as expected. In the LWIR, the critical electron density for broadening may be less than 10^{14} cm^{-3}; therefore, line broadening effects may be important for intermediate altitude nuclear plasmas.

Figure IV.11 illustrates the results when the electron temperature is changed from 5000 K to 50000 K with N_e=10^{16} cm^{-3} and T_{el}=5000 K. One can discern some differences in the 7.5 μm shoulders between the calculations at T_e=5000 K and 20000 K but little difference between those at T_e=20000 K and 50000 K. Therefore, as expected, the calculated spectra are fairly insensitive to T_e.

Figure IV.12 shows the calculations when the electronic temperature is changed from 5000 K to 16000 K with N_e=10^{16} cm^{-3} and T_e=20000 K. One can clearly see the changes in relative intensities of the 6 μm and the 7.5 μm lines as T_{el} is varied. The upper level of the transition responsible for

TABLE IV-2.

Basis Set for Unbundled Stark Calculations

n	ℓ	$E_0(S=1)$ (cm^{-1})	$E_0(S=2)$ (cm^{-1})
8	7	108122.41	108122.41
8	6	108122.38	108122.38
7	6	107597.48	107597.48
8	5	108122.29	108122.29
7	5	107597.36	107597.36
6	5	106788.58	106788.58
8	4	108122.02	108122.02
7	4	107596.96	107596.96
6	4	106787.891	106787.891
5	4	105446.29	105446.29
8	3	108120.79	108120.79
7	3	107595.147	107595.140
6	3	106785.201	106785.160
5	3	105441.724	105441.645
4	3	102968.343	102968.249
8	2	108114.0	108106.079
7	2	107582.777	107573.487
6	2	106765.803	106751.462
5	2	105409.008	105385.385
4	2	102908.420	102865.562
3	2	97488.476	97420.748
8	1	107778.	107720.
7	1	107072.	106982.
6	1	105912.031	105788.684
5	1	103870.020	103626.273
4	1	99681.051	99094.065
8	0	107497.224	107446.036
7	0	106627.934	106545.354
6	0	105165.232	105019.307
5	0	102411.995	102116.698
4	0	96225.049	95476.728

OI; NO PLASMA; 31 BS
ZERO FIELD
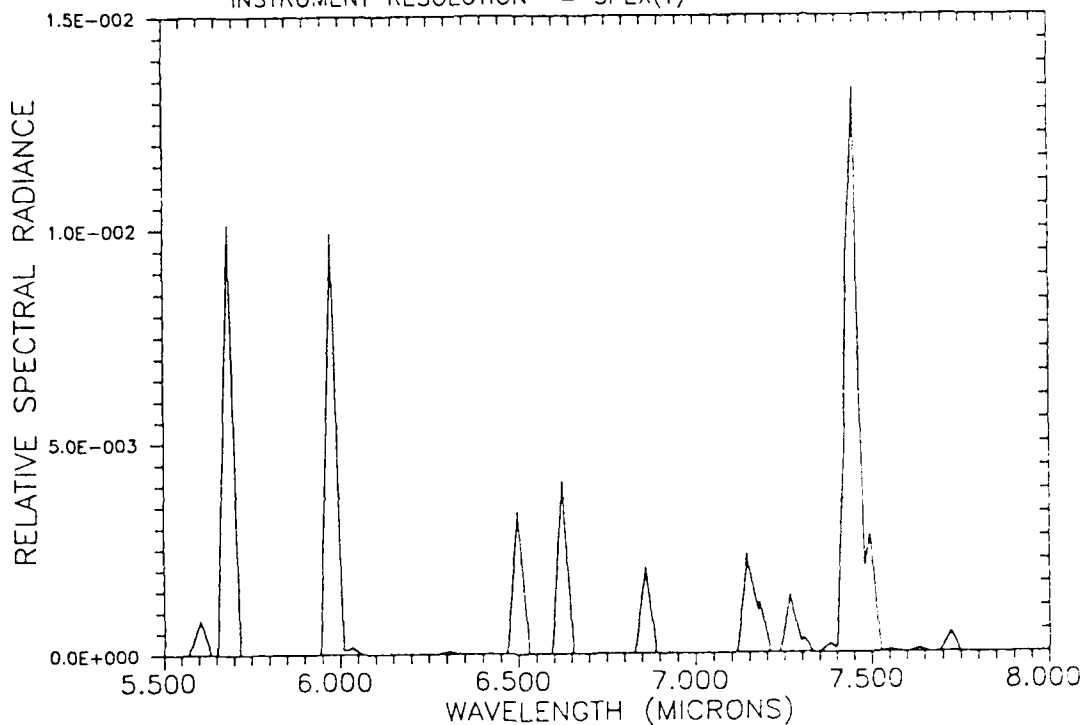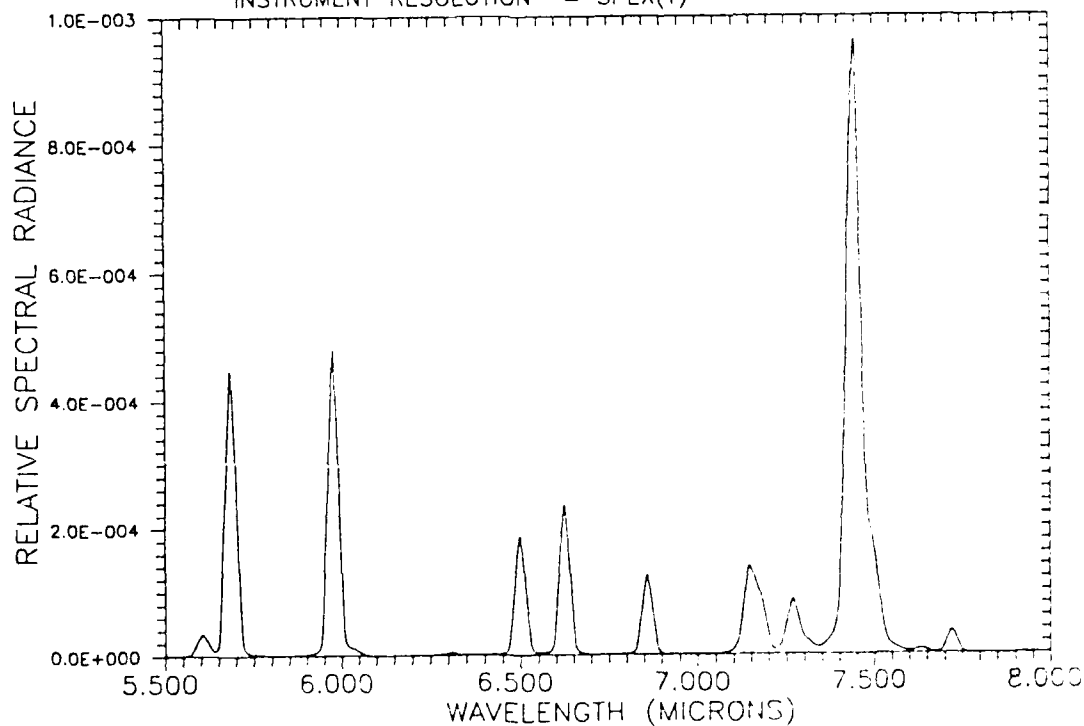
ELECTRONIC TEMPERATURE = 5000 K
INSTRUMENT RESOLUTION = SPEX(T)

Figure IV.10. Calculated OI spectra from 5.5 μm to 8.0 μm
as a function of electron density.

54
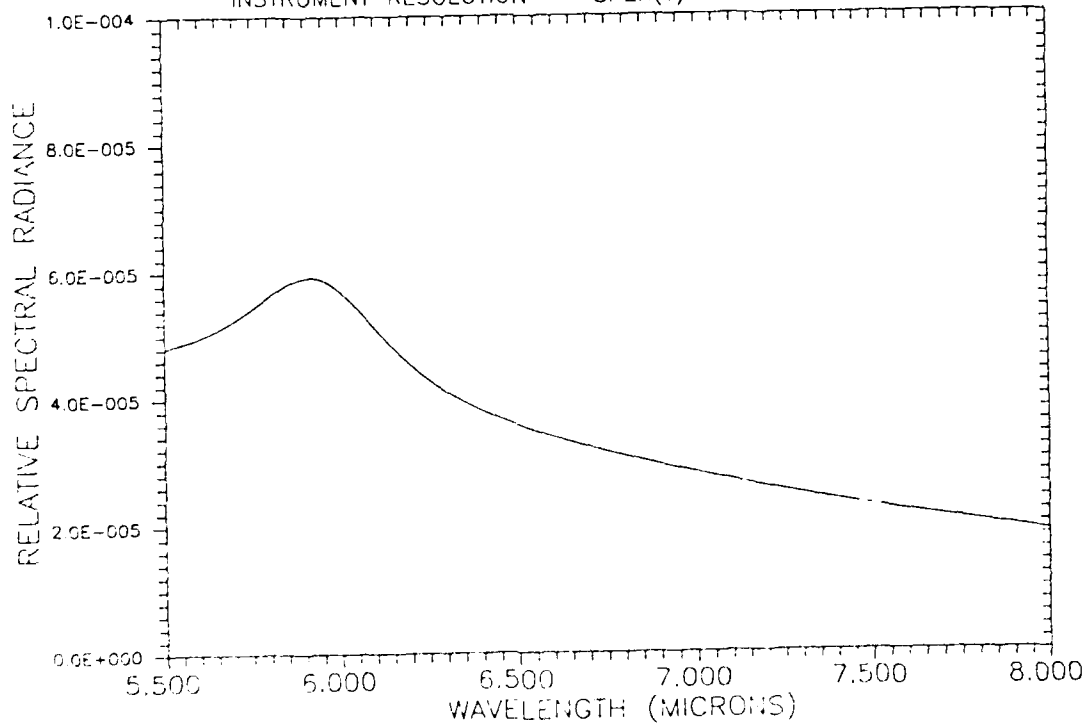
Figure IV.10. Calculated OI spectra from 5.5 μm to 8.0 μm
as a function of electron density.
(continued from previous page)
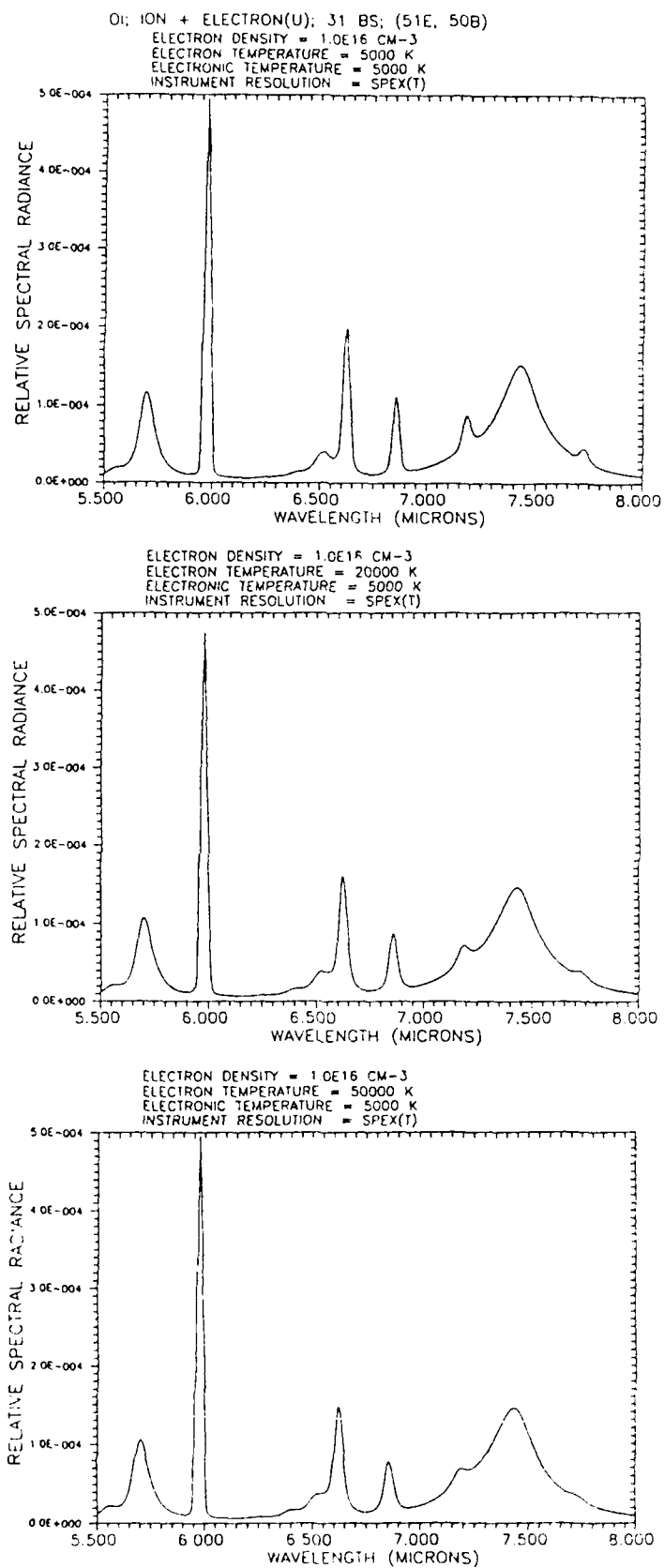
Figure IV.11. Calculated OI spectra from 5.5 μm to 8.0 μm
as a function of electron temperature.

OI; ION + ELECTRON(U); 31 BS; (51E, 50B)
ELECTRON DENSITY = 1.0E16 CM−3
ELECTRON TEMPERATURE = 20000 K
ELECTRONIC TEMPERATURE = 5000 K
INSTRUMENT RESOLUTION = SPEX(T)
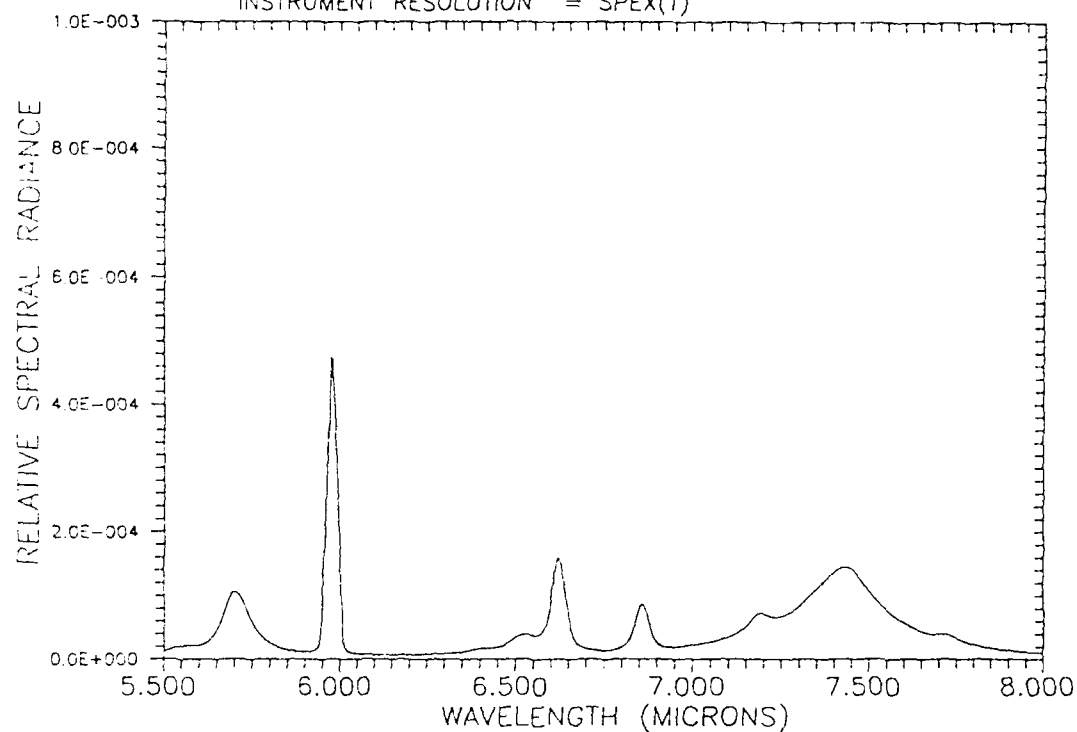
ELECTRON DENSITY = 1.0E16 CM−3
ELECTRON TEMPERATURE = 20000 K
ELECTRONIC TEMPERATURE = 8500 K
INSTRUMENT RESOLUTION = SPEX(T)

Figure IV.12. Calculated OI spectra from 5.5 μm to 8.0 μm
as a function of electronic temperature.

57

OI; ION + ELECTRON(U); 31 BS; (51E, 50B)
ELECTRON DENSITY = 1.0E16 CM-3
ELECTRON TEMPERATURE = 20000 K
ELECTRONIC TEMPERATURE = 12000 K
INSTRUMENT RESOLUTION = SPEX(T)
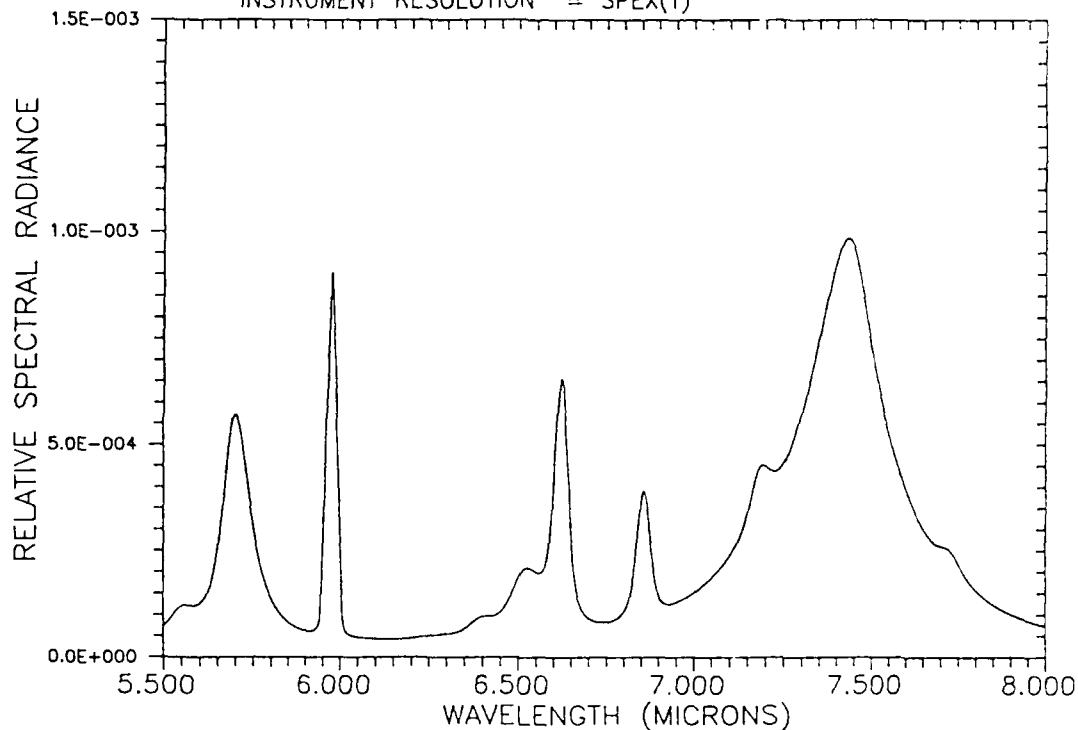
ELECTRON DENSITY = 1.0E16 CM-3
ELECTRON TEMPERATURE = 20000 K
ELECTRONIC TEMPERATURE = 16000 K
INSTRUMENT RESOLUTION = SPEX(T)
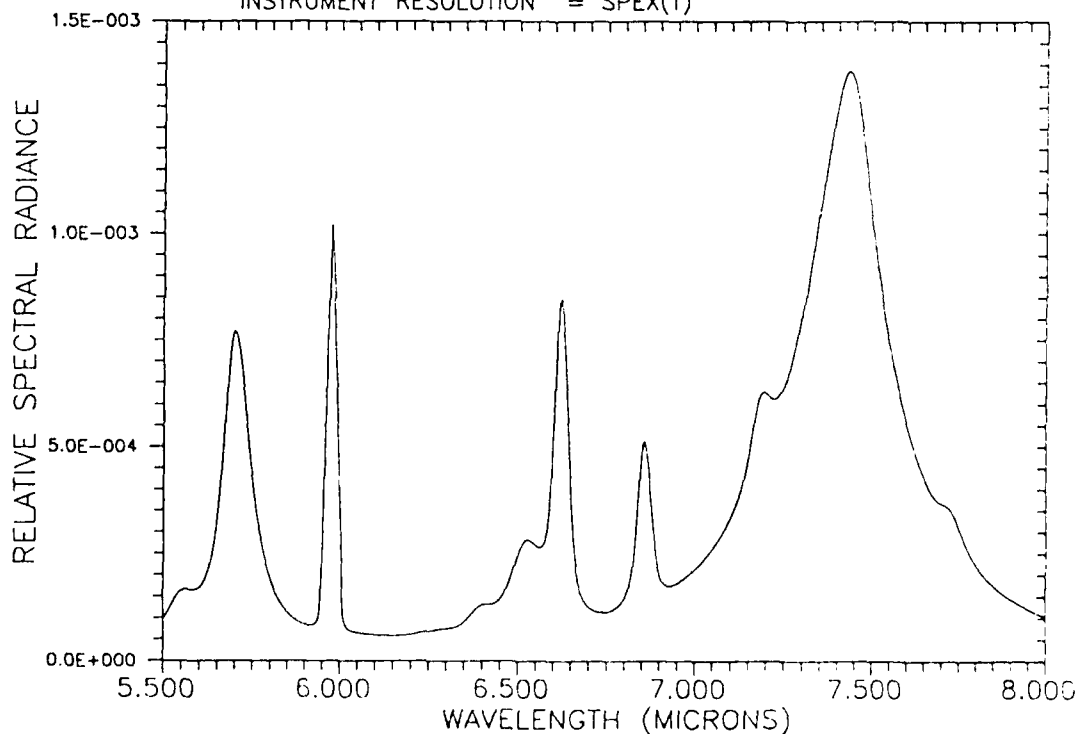
Figure IV.12. Calculated OI spectra from 5.5 μm to 8.0 μm as a function of electronic temperature. (continued from previous page)

58

the 6 μm line is n=4, whereas the upper level of the dominant transition in the 7.5 μm region is n=6. When T_{el} is increased, there is relatively more population in higher n states.

From the above discussion, we conclude that the benchmark calculations are producing trends which are consistent with the physical picture in our model. To summarize, the results are found to be highly sensitive to electron density and electron<u>ic</u> temperature but less sensitive to electron temperature.

3. DATA COMPARISON

The objective of the comparison with LINUS data is to find plasma parameters which give good agreement between calculated and experimental spectra over a wide spectral range at different delay times. Since these parameters have not been experimentally measured, a strategy was adopted to determine them theoretically. The rationale behind this strategy is based on the observation in the previous section that the calculated spectra are highly sensitive to N_e and T_{el} and less sensitive to T_e. The procedure is to first vary N_e to fit the broadest feature, i.e. the 7.5 μm multiplet, then to vary T_{el} to match the relative spectral radiance of the lines, and finally to set T_e equal to T_{el}. The last two steps are based on the assumption of LTE at late times, valid when collisional processes are more important than radiative processes. Since electrons are more effective than atoms or ions in collisional excitation and deexcitation, the electron temperature is used to define the temperature in the Boltzmann equation.

The LINUS OI experimental spectra from 5.5 μm to 8 μm for delay times of 6 μS and 12 μS are shown in Figures IV.13 and IV.14 respectively. These spectra have been calibrated for instrument responsivity but have neither been corrected for spatial inhomogeneity nor optical opacity. The continuum background has been arbitrarily fitted to a polynomial function and subtracted.

Comparing Figures IV.13 and IV.12, it can be seen that the general features of the calculated and experimental (at 6 μS) spectra agree quite well when N_e=1x10^{16} cm^{-3}, T_e=20000 K, and T_{el}=8500 K. These spectra have approximately the same line positions, line widths, and relative intensities. There are three differences: first, the 5.7 μm calculation is narrower than the data. One reason is that the calculation was performed with basis states up to n=8. It is known that transitions from n=9→6 lie in the 5.8 μm to 5.9 μm region. These lines, although weak compared to the

OXYGEN SPECTRUM

P(torr)= 118   Delay(microseconds)= 6.8
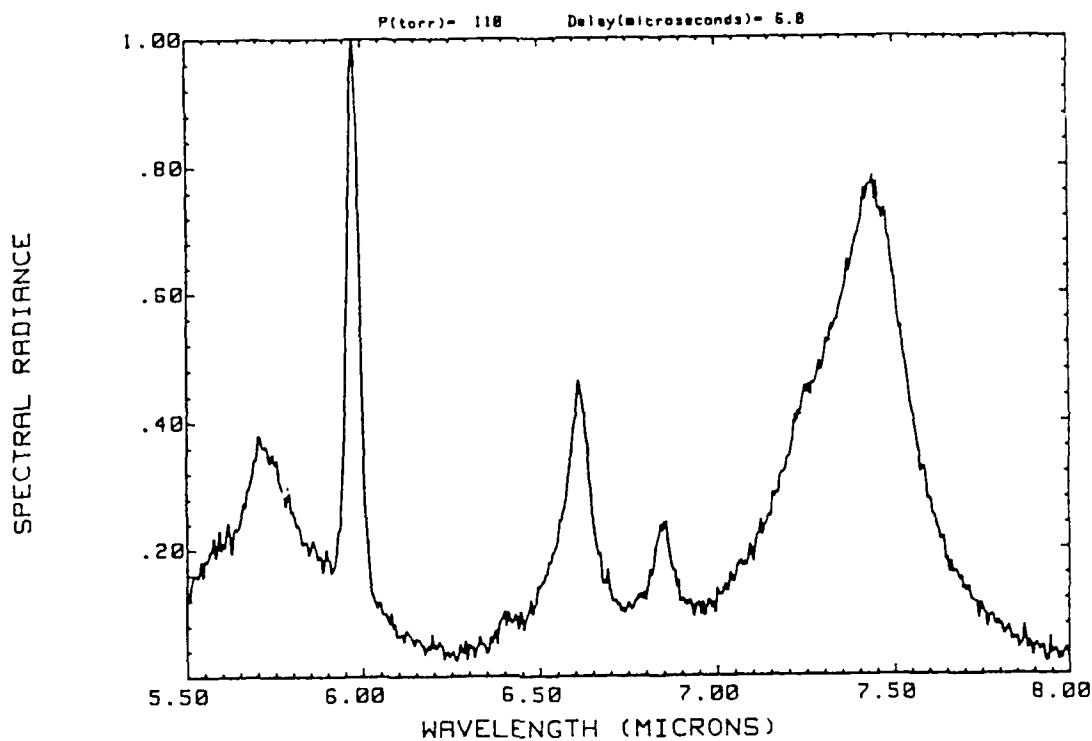
Figure IV.13. LINUS experimental OI spectrum from 5.5 μm to 8.0 μm at delay time of 6 μS.

OXYGEN SPECTRUM

P(torr)= 118   Delay(microseconds)= 12.8
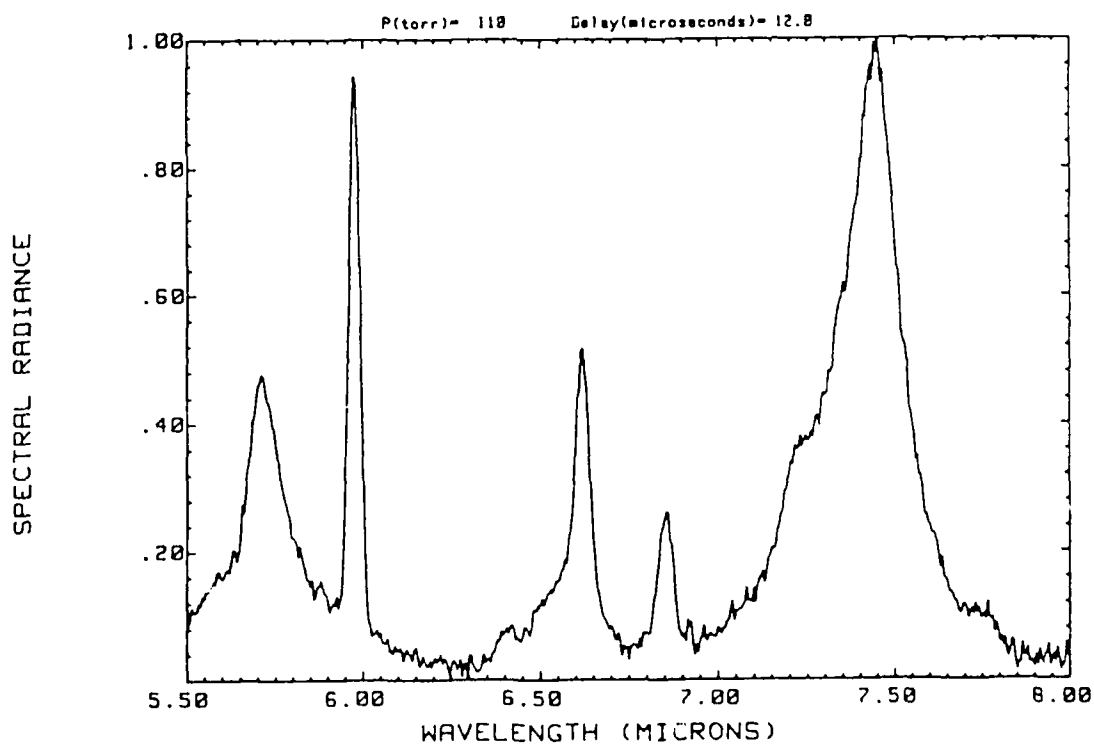
Figure IV.14. LINUS experimental OI spectrum from 5.5 μm to 8.0 μm at delay time of 12 μS.

5.7 μm line, may add intensity to the red wing of the 5.7 μm line. Second, the experimental data do not exhibit the two shoulders on the 7.5 μm calculation. A possible explanation is that the present method of calculating electron widths employs unperturbed wavefunctions and energy levels. It was shown previously in the 1.8 μm calculation (Section IV.C.1) that the use of ion-perturbed energy levels augments the electron widths. Therefore, it is expected that the semi-perturbed method will also broaden the 7.5 μm lines in which case the two shoulders may disappear. Lines other than the 7.5 μm will be broadened as well and it may be necessary to decrease the electron density to fit the data. Third, there are minor differences in the relative spectral radiance of the lines. This implies that the electronic temperature is not yet optimized and needs to be further adjusted.

Preliminary fitting of the 12 μS LINUS data indicates an electron density around 7×10^{15} cm^{-3}. This is consistent with the 6 μS result in that the electron density should be lower at longer delay times. The electronic temperature is still in the process of being determined. From the above comparisons and considering the uncertainties in the experimental data, the agreement between data and the calculation is excellent. It is interesting to note that the value for the electron density at 6 μS is comparable to the value arrived at using the SALE/ARCHON chemical dynamics approach (see Chapter VI). In order to understand in more detail the mechanism responsible for the broadening, more investigation into the causes of the differences discussed above is necessary. There are two logical calculations to perform: first, OI emission including basis states higher than n=8, and second, OI emission using the semi-perturbed method.

D. DISCUSSION

The present model of the Stark line broadening problem is based on a simple physical approach. In this section we summarize the limitations arising from the assumptions used in this model. The areas which warrant caution and investigation are addressed.

1. The model assumes the quasistatic and impact approximations. The results should be trusted only for cases where the validity criteria are met. These criteria were discussed in Section IV.B.

2. The model is only applicable in a certain range of electron densities. At low electron density, the Debye length is large and hence the integration limit in the collision time integrals (see eq. IV.25) is

large. This implies that the integrand oscillates over a large time scale which makes the integral difficult to converge. Therefore, the calculation of electron widths is increasingly inaccurate as the electron density is decreased. Fortunately, it is observed that the electron widths at $N_e=10^{14}$ cm^{-3} are about an order of magnitude smaller than the instrument width. Below this density it can safely be assumed that the electron widths are negligible. At high electron density, the off-diagonal matrix elements in the Hamiltonian are no longer small compared to the diagonal matrix elements, implying that the second-order perturbative treatment of Stark field is no longer applicable.

3. The model assumes that the lineshape for overlapping lines is the sum of the lineshapes for individual lines. This is not entirely valid as it is well known that interference effects arise which may alter the lineshape for overlapping lines. The expression for the lineshape function for overlapping lines is given in ref. 14.

4. The assumption of Boltzmann population distribution is valid when collisional processes dominate radiative processes, i.e. when the electron density is high. It is generally applicable for high-lying states near the ionization limit but is not as valid for low-lying states which are further apart. This implies that the use of an electronic temperature may not result in relative spectral radiance in agreement with experiment. To calculate the relative population would require a detailed model accounting for all collisional and radiative processes among the states of interest.

5. The model uses a semi-classical approach to calculate the electron broadening cross section. The effect on the cross section calculated by a quantum-mechanical approach should be assessed.

6. The model assumes no energy level shift due to electrons. An examination of the table of electron shift in ref. 14 shows that this quantity is small for most OI lines listed. The largest shift is 2.29 A for the 5330 A (S=2 5d-3p) line at $N_e=10^{16}$ cm^{-3} and $T_e=5000$ K. If one assumes an order of magnitude increase in the shift for higher n transitions, the shift would be 0.0029 μm, which is less than the experimental step size of 0.005 μm. Therefore, it is reasonable to conclude that error in line positions due to neglect of electron shift would not be discernible.

7. The model includes only dipole interaction. The effect of quadrupole interaction may be important and is discussed in ref. 14.

8. The model does not account for effect due to ion motion. Recent results in line broadening theory have demonstrated that ion dynamics may play an important role in the line broadening problem[37] at high temperatures.

9. The model uses atomic properties (e.g. dipole moment) which are based on an unperturbed atom. Recent results have shown that the plasma microfield may effect atomic properties[38].

Each of these areas will be investigated and resolved as the code development matures.

V. HYDRODYNAMIC CALCULATIONS

A. GENERAL

The purpose of this chapter is to present a hydrodynamic model of the LINUS plasma and the results of this modelling effort. Section V.B discusses the SALE (Simplified Arbitrary Lagrangian Eulerian) hydrodynamic code[39] and its application to LINUS. Section V.C discusses the results of the hydrodynamic calculation which has produced important information on the LINUS discharge region. Section V.D examines the assumptions behind the model and their validity.

The objective in performing hydrodynamic calculations is to model the general morphology of the LINUS plasma expansion, and to understand its effects on recombination and radiative properties. The output of such a calculation gives spatial and temporal information on hydrodynamic quantities such as pressure, density, velocity, and specific internal energy. There are two important applications. First, the calculated spatial and temporal information may be used as a guide in the experimental expansion measurements to determine the location and time that data should be taken. Second, if one assumes that the electron temperature is coupled to the heavy particle temperature, then the temporal profile of heavy particle temperature derived from SALE may subsequently be used in a kinetics calculation to drive the chemistry inside the discharge region. The chemistry calculation gives insights into the temporal history of the destruction and formation of different charged species. The results may be compared with experimental observations.

To understand the LINUS expansion dynamics of the discharge region, the SALE code (originally written by Amsden et al. of Los Alamos National Laboratory and subsequently adapted by Cosner of MRC/Santa Barbara) has been applied to elucidate the spatial and temporal properties of the gas after deposition of laser energy. The important hydrodynamic processes to be examined are the generation of shock fronts and initial expansion due to laser energy deposition, shock front effects, post-shock cooling, and pressure recovery.

In order to validate the results of the SALE calculation, experimental spatial-temporal measurement of the spark is required. At the moment, however, there is only a visual description of the spark. The laser-induced oxygen spark (Figure V.1) is an intense silver-blue color and is generally cigar-shaped along the laser axis. Its shape and size change

as a function of pressure. At 110 torr (pressure at which the SALE calculation is performed), the spark is about 1 mm wide and 4 mm long. The core is surrounded by a light blue halo which is shaped like an atomic p orbital with the lobe dimension about 4 mm in diameter. The p-orbital structure is further surrounded by a thin oblong layer which gives an overall dimension (including the halo) of width 6 mm and length 10 mm. The shape is symmetrical with respect to the focal point. This picture supports the experimental data of the spark structure of N_2 at 200 torr previously obtained[40]. The only inconsistency is that the previously reported ring structure surrounding the focal point cannot be reproduced at the present time. As is expected, the spark gets smaller when the pressure is decreased. At 10 torr, only a faint bluish dot can be seen. As the pressure increases, the spark gets brighter and changes from a symmetric to an asymmetric shape. The asymmetry is shown clearly at 250 torr — the top lobe (the side farther away from the laser) has broken up and become distorted with a shape resembling a mushroom with ragged edges. The larger lobe is likely due to appreciable absorption of the laser energy in the region which is nearer the laser. The ragged edges most likely arise from expansion instabilities. Although the visual description of the spark is time-integrated, it should still be reproduced by the hydrodynamic results.

Figure V.1. Visual morphology of the LINUS discharge vs. pressure.

B. SALE CODE AND HYDRODYNAMIC MODEL

SALE is a general fluid code which uses a simplified numerical fluid dynamics computing technique to calculate two-dimensional fluid flows. It is based on the solution to the Navier-Stokes fluid equation of motion and the mass and internal energy equations. It can handle flow speed from the incompressible to the supersonic limit in the Lagrangian or the Eulerian mode, or somewhere in between. In the Lagrangian mode, the cell vertices move with the fluid, whereas in the Eulerian mode the grid remains stationary and the variables at a fixed point in space change as a function of time. The code has been widely used and well tested[41]. Its potential limitations for the present application are single fluid treatment and no allowance (yet) for energy loss.

Previous hydrodynamic calculations of the LINUS plasma using the SALE code with no regrid capability showed that the shock wave had already reached the boundary of the computing mesh at 5 nS[42]. In order to acquire hydrodynamic information at later times, Dr. Ken Cosner of MRC/SB has provided a regrid routine, which when coupled to the SALE code, allows the calculation to be extended to times of greater than 3 nS. At present, the regrid routine is set up in such a way that a regrid is triggered whenever either the vertical component of the velocity vector at the next to last top boundary or the horizontal component of the velocity vector at the next to last right boundary is greater than 200 cm/S. During a regrid, the number of cells in the grid remains constant but the dimension of the cell is doubled in both the x- and y-directions. The MRC-modified SALE code has a regrid capability for Eulerian calculation and conserves total energy.

The calculation of the shock front and expansion characteristics in the LINUS plasma has been initiated by assuming that the plasma behaves like an ordinary fluid, the motion of which obeys the Navier-Stokes equation. One begins by specifying the geometry of the computing mesh, assumed to be a set of quadrilateral cells. For each cell, the code calculates momentum, position, volume, energy, mass density, and pressure. The pressure is calculated from the specified equation of state (described later).

The initial computing mesh consists of 40 by 40 cells with dimension 5 μm by 5 μm per cell. The laser propagation axis is the left boundary of the mesh, also the symmetry axis in the cylindrical coordinate system. The direction of laser propagation is pointing upwards. The amount of energy deposited is based on measurements of the transmitted laser power after passage through the gas cell as a function of pressure[43]. For a pressure

of 110 torr, the amount of laser energy absorbed has been interpolated from measurements to be about 13% of the initial laser energy of 1 J, or 130 mJ. Since the spark is symmetrical at this pressure, only one quadrant of the spark is simulated.

Historically[10,11], the focal length of the lens used in the experiment has been reported to be 5.6 to 5.8 cm but subsequent measurements[43] show that the focal length is 4.1 cm; this value is adopted in the present calculation. From geometrical optics formulas[10], a 4.1 cm focal length lens gives a focal region of radius 10 μm and length 54 μm. The important quantity is the distance where the laser intensity equals the threshold breakdown intensity. Using a threshold intensity of 6×10^{11} W/cm^2 (obtained at 110 torr from ref. 10) and assuming a Gaussian laser pulse with peak intensity of 4×10^{12} W/cm^2, the axial distance where breakdown threshold is reached is 90 μm. It is therefore assumed that the first dose of energy is uniformly deposited into a 10 μm by 90 μm region.

The observed spark shape is simulated by incorporating the time-dependent coupling of laser energy at the expanding high density shock regions which lie along the laser axial region. The laser profile is assumed to be a 10^{-8} S square wave. The amount of energy deposited into a cell, E_{cell}, at each time step, δt, is given by

$$E_{cell} = \frac{\delta t}{10^{-8}} \left(\frac{\rho_{cell}}{\rho_{total}} \right)^2 E_{total} , \qquad (V.1)$$

where E_{total} is the amount of laser energy absorbed, ρ_{cell} and ρ_{total} are, respectively, the cell and total mass density. The weighting of the density is based on the assumption of an inverse bremsstrahlung absorption mechanism.

The choice of an equation of state (EOS) for the SALE code poses some problems because its use implies the system is in thermodynamic equilibrium, a condition which is most likely invalid in LINUS. In the absence of more information, however, the use of an EOS is a reasonable approximation. Since the early-time temperature in LINUS is extremely high, all the molecules should have dissociated and the only gaseous species present would be monatomic. Hence, there is no need to include excitation of internal degrees of freedom such as vibration and rotation. Under such circumstances, the use of any real EOS is probably not justified. Given the above considerations, it is thought that the ideal

67

gas EOS is a reasonably good approximation and is therefore assumed in the SALE calculation. It is given by

$$p = (\gamma - 1)\rho I \qquad\qquad (V.2)$$

where p is the pressure, γ is the ratio of specific heats (equal to 1.67 for monatomic gas), ρ is the mass density, and I is the specific internal energy.

For the present calculation, no chemistry or radiative loss is included. The importance of these processes will be discussed below. The reflective nature of plasmas is also neglected as it has been shown to be unimportant since the laser frequency is greater than the electron plasma frequency (see Chapter II). An implicit Eulerian calculation is carried out.

C. RESULTS

The results of the calculation, shown in Figures V.2-8 are represented in contour plots for the parameters pressure, density, speed, and energy for times of 1 nS, 10 nS, 70 nS, 0.12 μS, 0.5 μS, 1 μS, and 5 μS. The spatial coordinates shown are the cell-centered values in cm. All units are given in the cgs system: dyne/cm^2 for pressure, g/cm^3 for mass density, erg/g for specific internal energy, and cm/sec for speed.

These plots clearly show the formation and elongated expansion of the shock front, defined by a large amplitude disturbance. The disturbance occurs in a region where the thermodynamic quantities are undergoing extremely rapid changes compared to the region adjacent to it. The mass density at the shock front is about a factor of two higher than ambient. However, at the core region it has decreased by about an order of magnitude. This verifies the intuitively expected picture of a rapid expansion when a large quantity of energy is suddenly deposited into a small volume. The hot and compressed gas in the core region expands rapidly and initiates a pressure wave in the surrounding gas. It is this rarefaction of the region behind the shock front which allows the observation of long-lived emission in LINUS.

The various hydrodynamic quantities as a function of the radial coordinates, x, with the axial distance, y, at 0.288 cm are shown in a two-dimensional configuration in Figure V.9, for t=120 nS. From this figure, it is seen that the mass density has dropped by about an order of magnitude

Figure V.2. SALE contour plots for labelled parameters at 1 nS for a pressure of 110 torr with continuous laser energy deposition.

PRESSURE T=10 NS(C)

DENSITY T=10 NS(C)

SPECIFIC INTERNAL ENERGY T=10 NS(C)

SPEED T=10 NS(C)

Figure V.3. SALE contour plots for labelled parameters at 10 nS for a pressure of 110 torr with continuous laser energy deposition.

PRESSURE T=70 NS(C)

DENSITY T=70 NS(C)

SPECIFIC INTERNAL ENERGY T=70 NS(C)

SPEED T=70 NS(C)
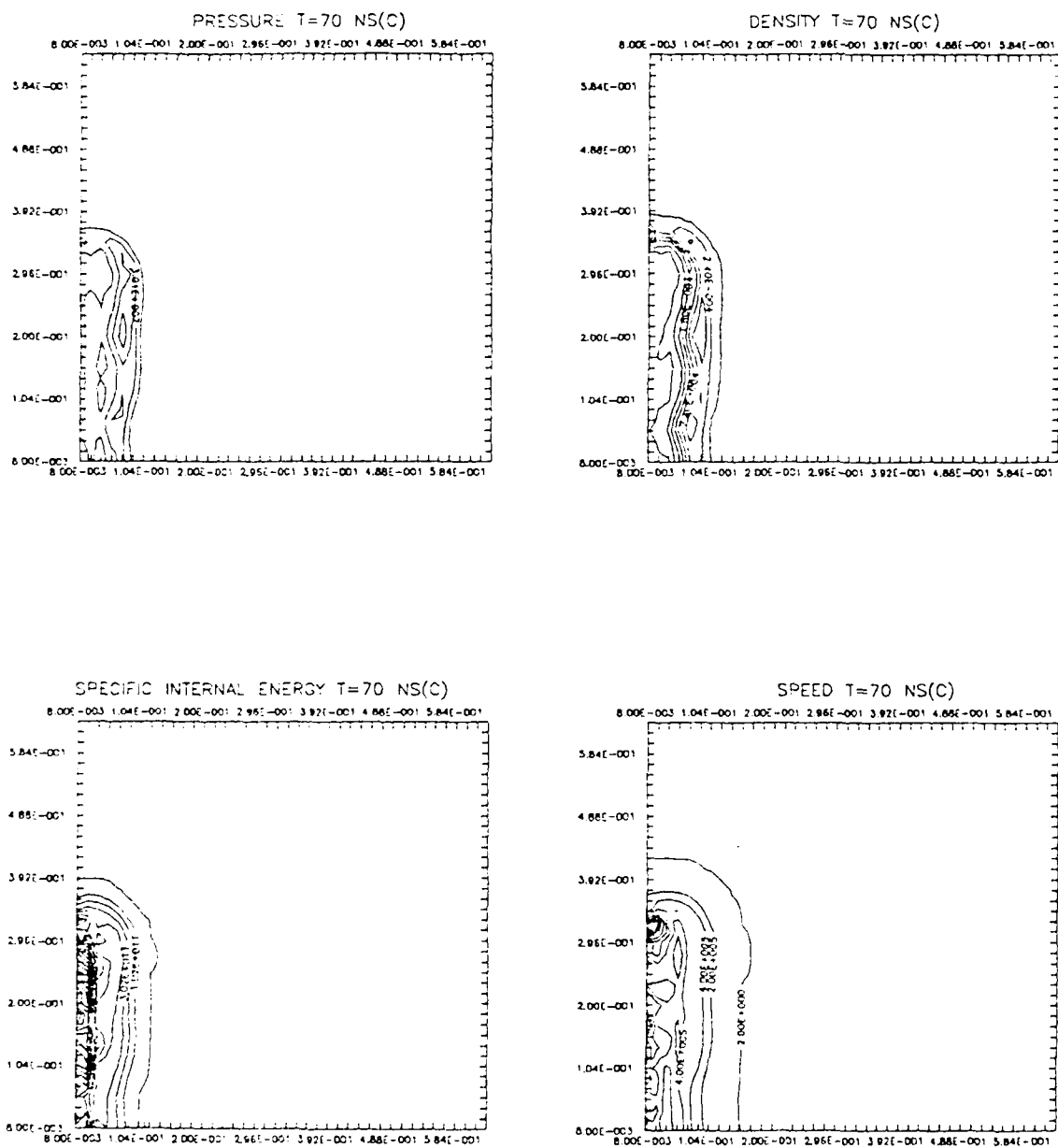
Figure V.4. SALE contour plots for labelled parameters at 70 nS for a pressure of 110 torr with continuous laser energy deposition.

71

PRESSURE T=0.12 MICROS(C)

DENSITY T=0.12 MICROS(C)

SPECIFIC INTERNAL ENERGY T=0.12 MICROS(C)

SPEED T=0.12 MICROS(C)

Figure V.5. SALE contour plots for labelled parameters at 0.12 μS for a
pressure of 110 torr with continuous laser energy deposition.

72

PRESSURE T=0.5 MICROS(C)

DENSITY T=0.5 MICROS(C)

SPECIFIC INTERNAL ENERGY T=0.5 MICROS(C)

SPEED T=0.5 MICROS(C)

Figure V.6. SALE contour plots for labelled parameters at 0.5 μS for a
pressure of 110 torr with continuous laser energy deposition.

73

Figure V.7. SALE contour plots for labelled parameters at 1 μS for a pressure of 110 torr with continuous laser energy deposition.

74

Figure V.8. SALE contour plots for labelled parameters at 5 μS for a
pressure of 110 torr with continuous laser energy deposition.
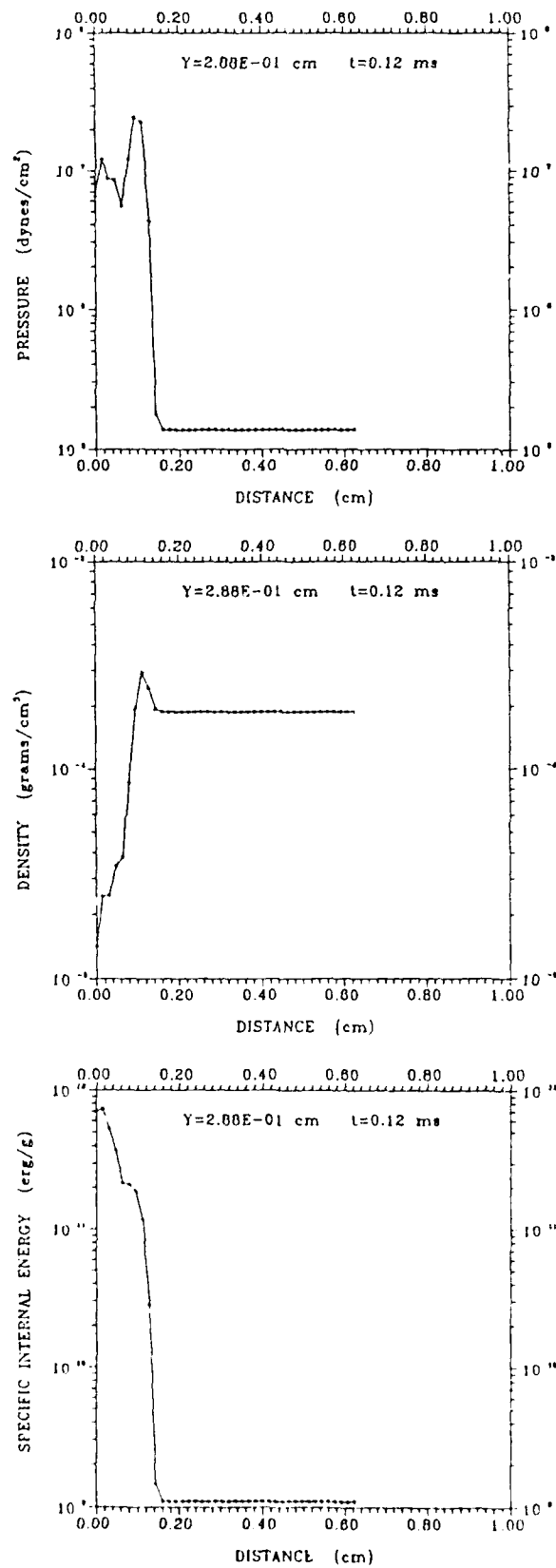
Figure V.9. Plots of SALE-derived parameters at 0.28 cm from the laser axis for a time of 120 nS after continuous laser energy deposition.

behind the shock front while the pressure remains virtually constant for the same spatial location. Therefore, the temperature must rise to compensate. This expected behavior of the temperature is consistent with its calculation from specific internal energy.

An estimate of the visible spark size from the present hydrodynamic calculation can be made. We define the time to be that at which energy at the shock front has dissipated below that required to dissociate the gas. The temperature at the shock front which corresponds to the dissociation energy of O_2 (5.2 eV) occurs around 45 nS. From the plots at this time, it is estimated that the spark is approximately 6 mm long by 2 mm wide. This is in approximate agreement with the observed spark core size. The larger "halo" is not believed to originate from the hydrodynamic effects. As discussed in Chapter III, the halo is most likely due to ultraviolet and x-ray deposition originating from the core region.

A second calculation was performed which employs a different temporal profile to simulate the initial laser pulse. In this case, the laser energy deposition profile is assumed to be ten pulses, each containing 1/10 of the total energy deposited, spaced 1 nS apart. The results are shown in Figure V.10-16 for times of 1 nS, 10 nS, 54 nS, 0.1 μS, 0.5 μS, 1 μS, and 5 μS. Compared to the continuous simulation discussed above, the pulsed simulation gives a spark which is more elongated at early times but more spherical at late times. The shape of the calculated spark also appears less like a "p-orbital". This is one of the reasons why it is important to understand the details of the laser pulse. The result at late times is not surprising since a large quantity of energy is being deposited into a focal region miniscule with respect to the spark size and within a temporal element which is short compared to microseconds.

D. DISCUSSION

The present calculation gives good qualitative agreement with experiment and blast wave theory[42]. It has, however, some limitations in th·· the code neglects several issues which may be important and thus must be addressed.

(1) The calculation is single-fluid. It does not account for the differential presence of electrons and ions. However, the collision rate is sufficiently high that this is not a serious limitation on the application. The determination of whether this assumption is valid is based on the equilibration time of the electrons and ions. At early times,

PRESSURE T=1 NS(P)

DENSITY T=1 NS(P)

SPECIFIC INTERNAL ENERGY T=1 NS(P)

SPEED T=1 NS(P)
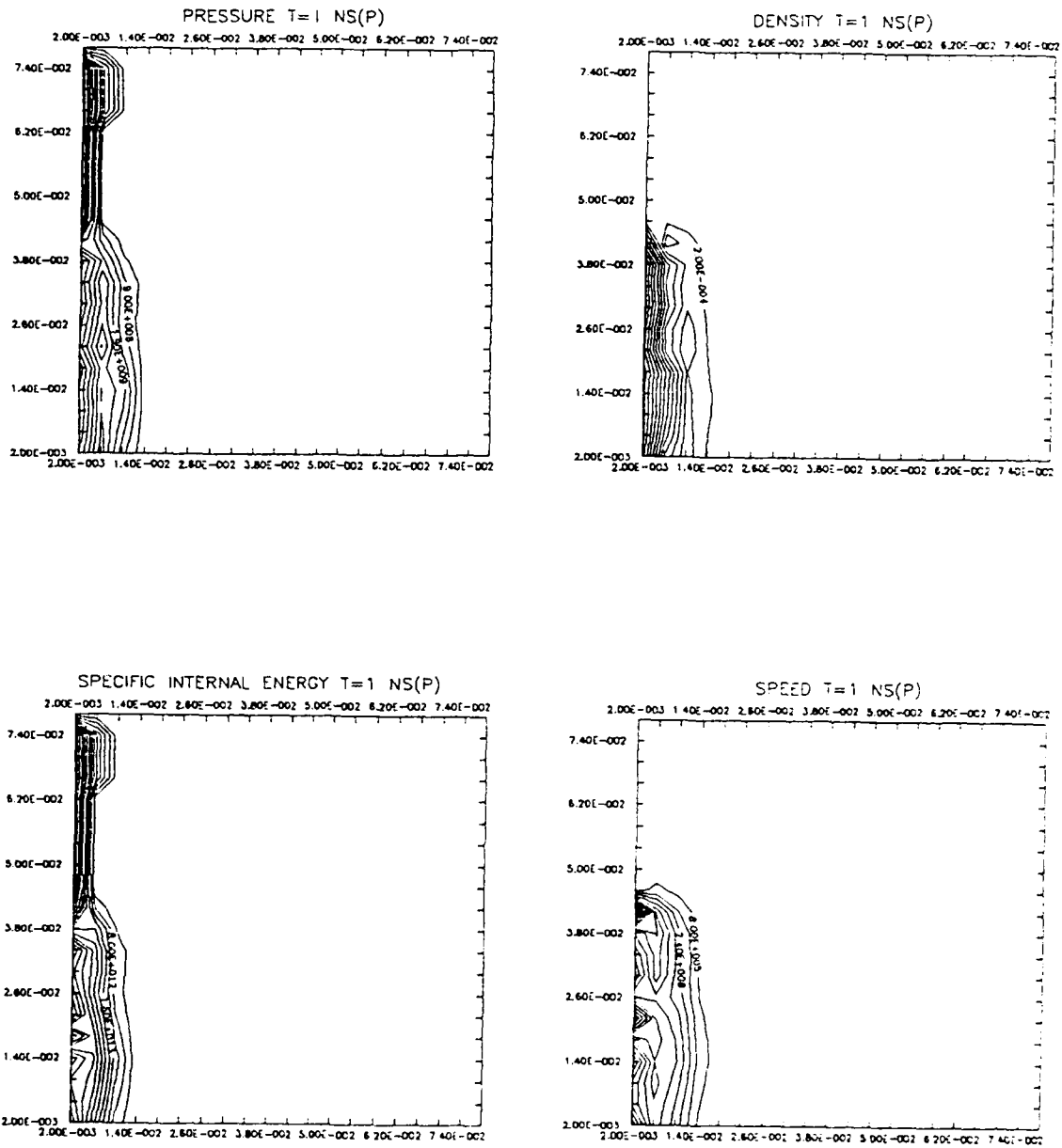
Figure V.10. SALE contour plots for labelled parameters at 1 nS for a
pressure of 110 torr with pulsed laser energy deposition.

78

PRESSURE T=10 NS(P)

DENSITY T=10 NS(P)

SPECIFIC INTERNAL ENERGY T=10 NS(P)
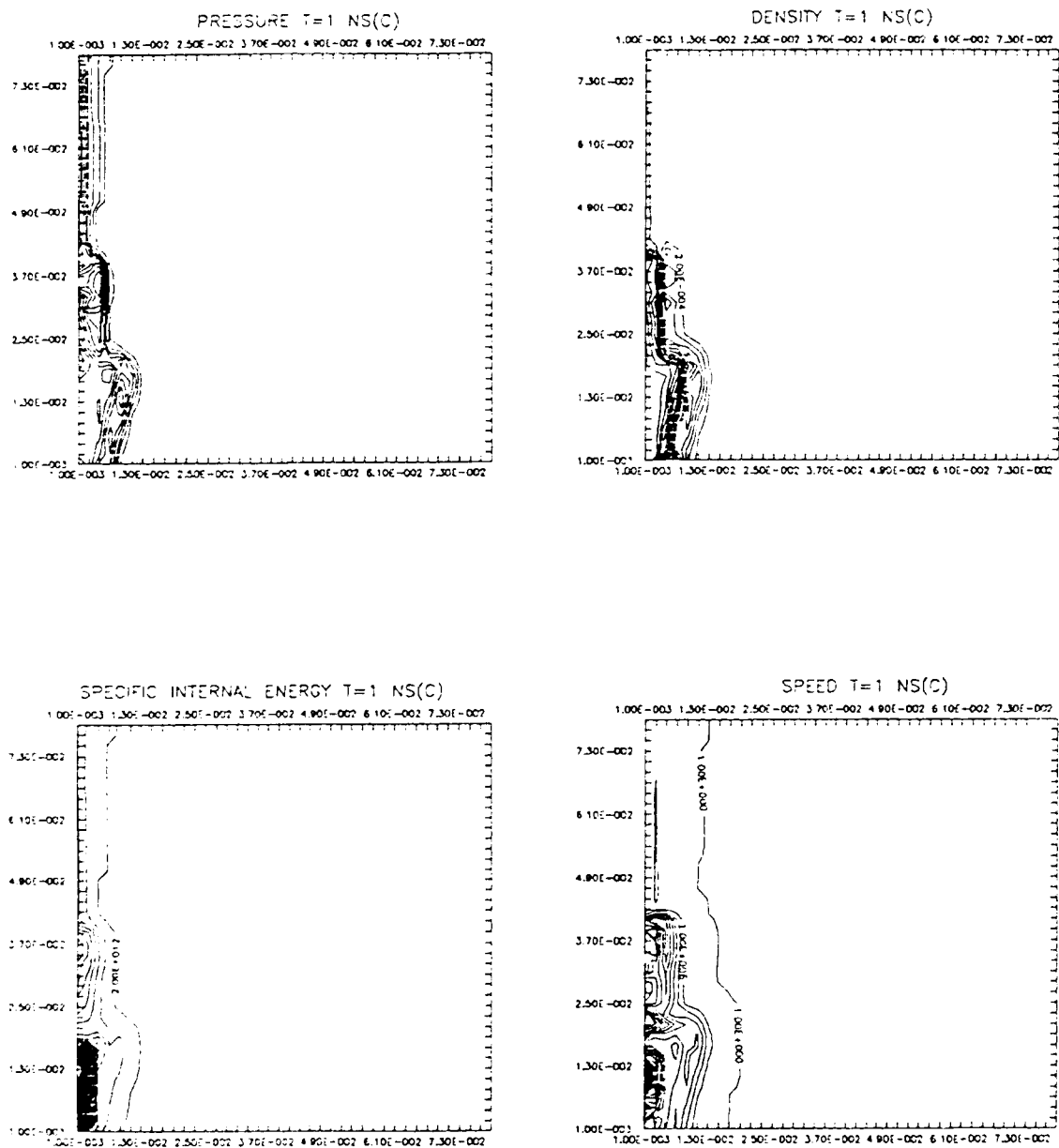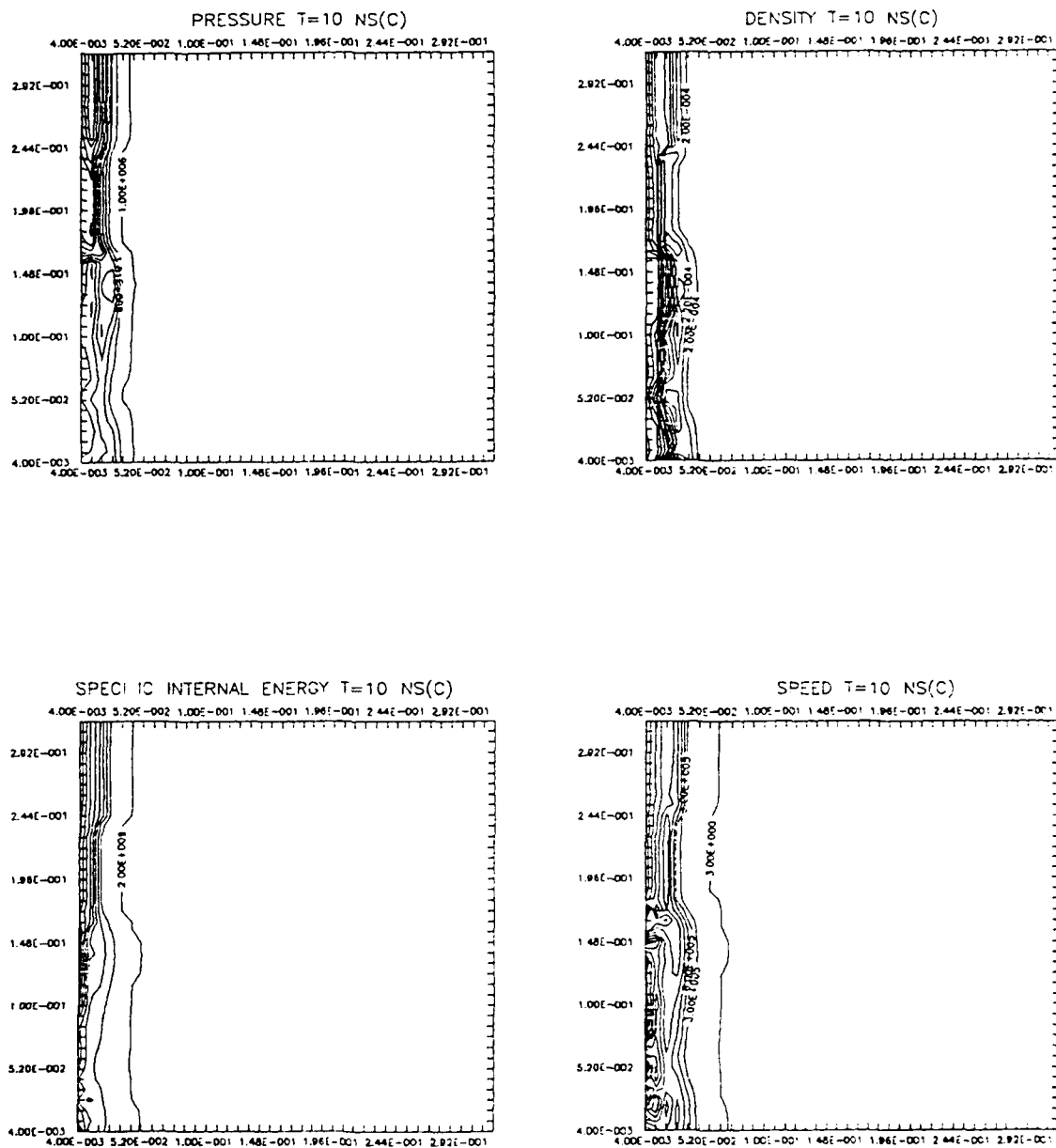
SPEED T=10 NS(P)
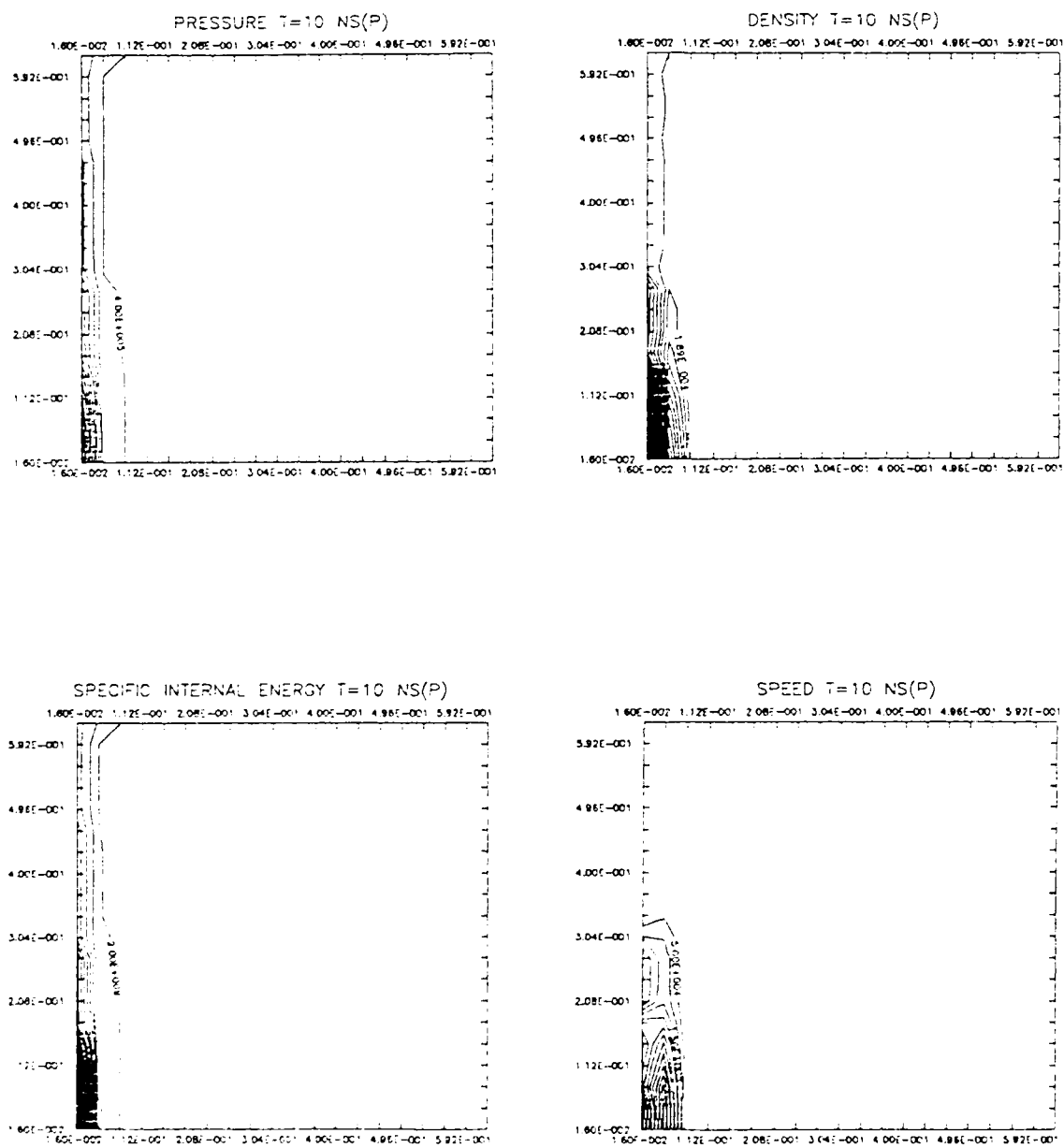
Figure V.11. SALE contour plots for labelled parameters at 10 nS for a pressure of 110 torr with pulsed laser energy deposition.

79
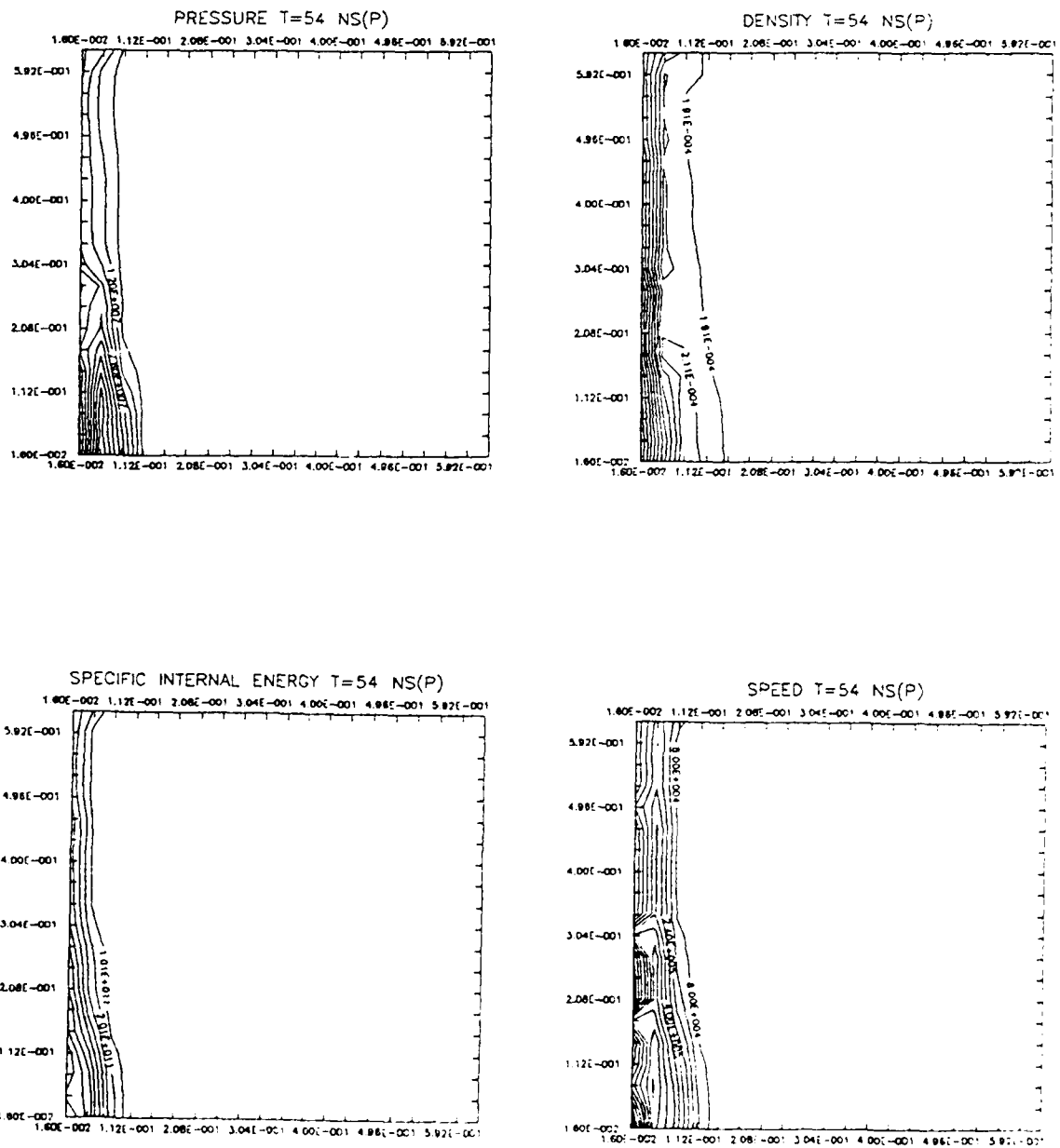
Figure V.12. SALE contour plots for labelled parameters at 54 nS for a pressure of 110 torr with pulsed laser energy deposition.

PRESSURE T=0.1 MICROS(P)

DENSITY T=0.1 MICROS(P)

SPECIFIC INTERNAL ENERGY T=0.1 MICROS(P)

SPEED T=0.1 MICROS(P)

Figure V.13. SALE contour plots for labelled parameters at 0.1 μS for a pressure of 110 torr with pulsed laser energy deposition.

PRESSURE T=0.5 MICROS(P)

DENSITY T=0.5 MICROS(P)

SPECIFIC INTERNAL ENERGY T=0.5 MICROS(P)

SPEED T=0.5 MICROS(P)
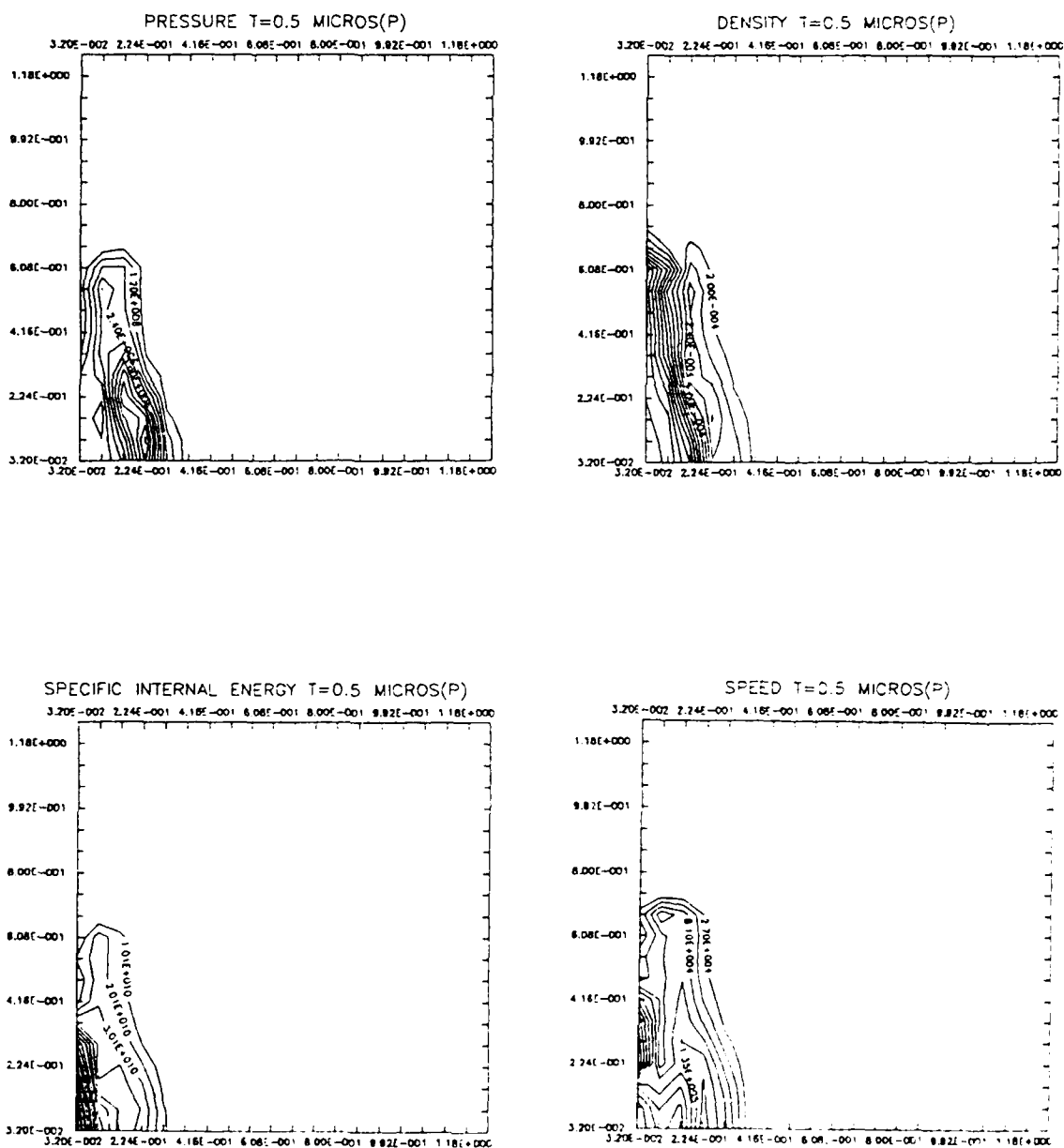
Figure V.14. SALE contour plots for labelled parameters at 0.5 μS for a pressure of 110 torr with pulsed laser energy deposition.

PRESSURE T=1 MICROS(P)

DENSITY T=1 MICROS(P)

SPECIFIC INTERNAL ENERGY T=1 MICROS(P)

SPEED T=1 MICROS(P)
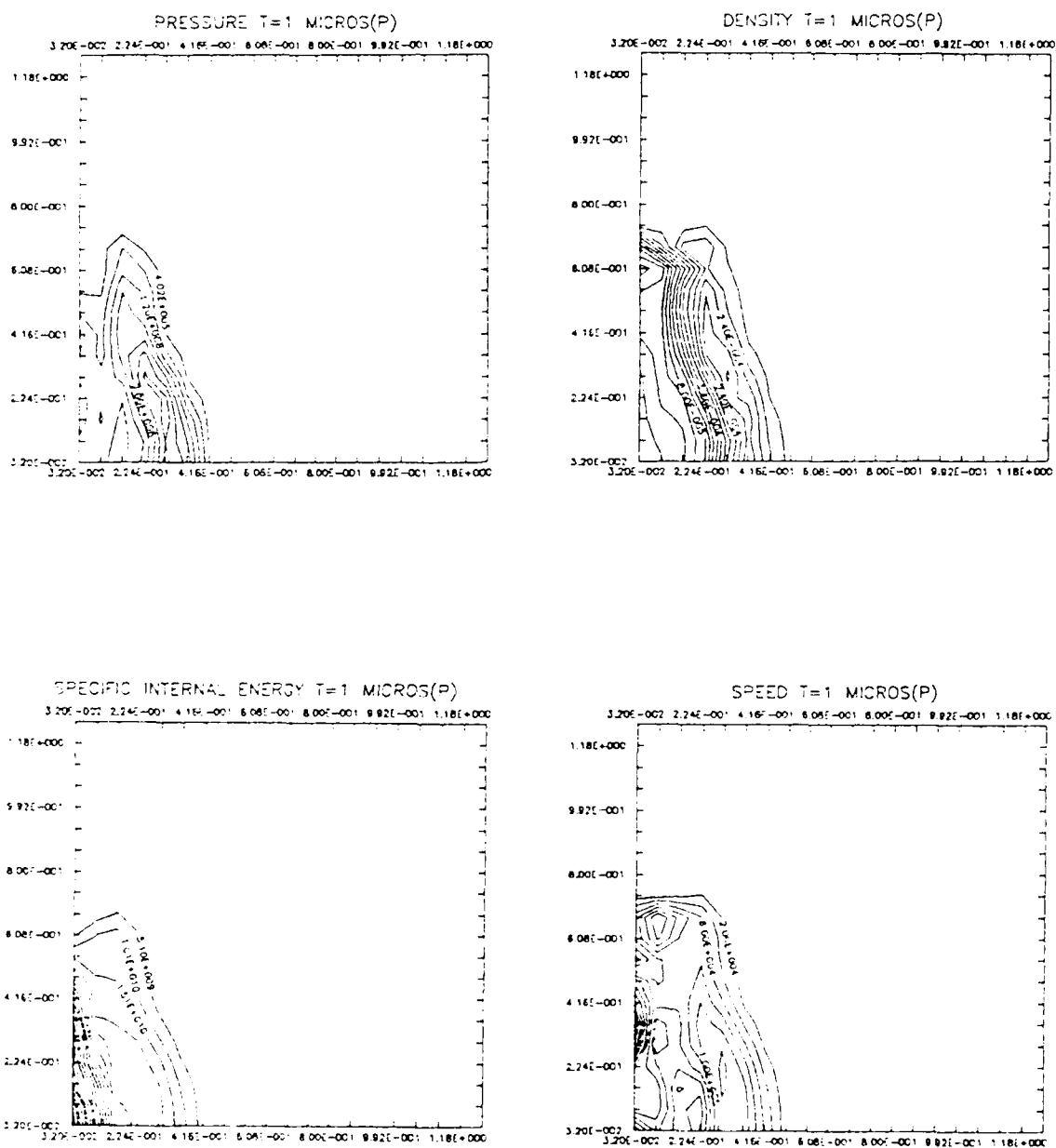
Figure V.15. SALE contour plots for labelled parameters at 1 μS for a pressure of 110 torr with pulsed laser energy deposition.

83
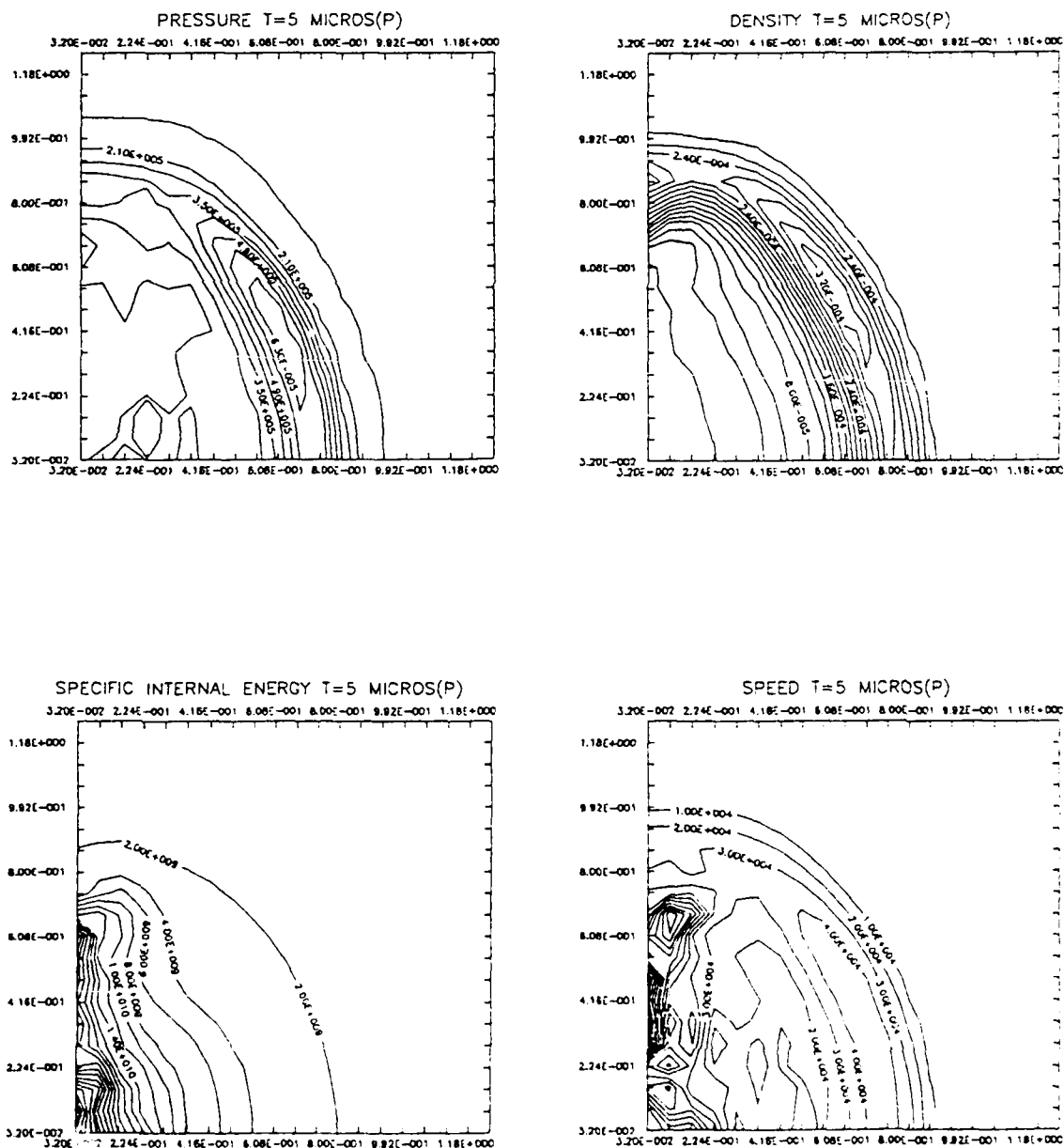
Figure V.16. SALE contour plots for labelled parameters at 5 µS for a pressure of 110 torr with pulsed laser energy deposition.
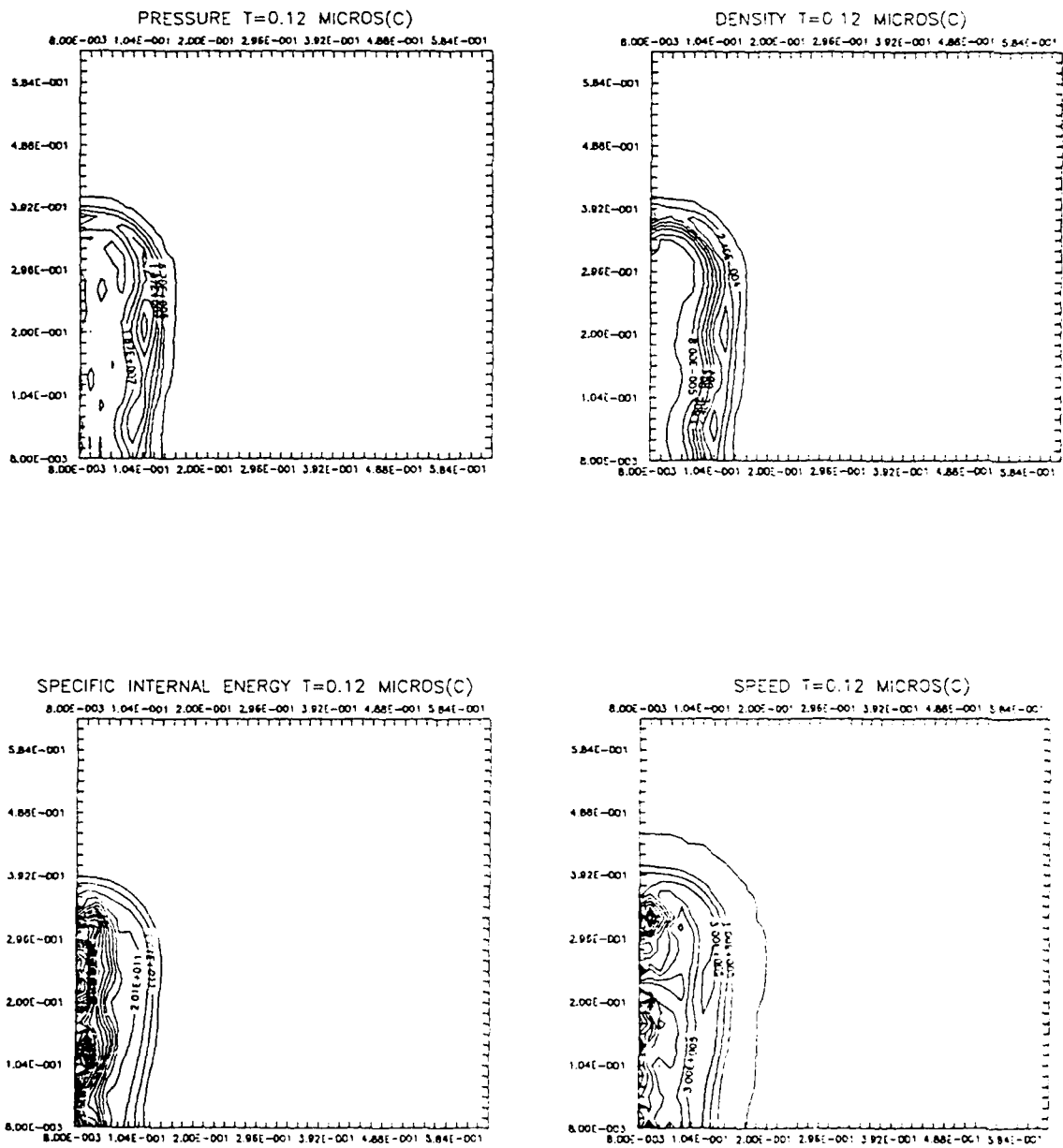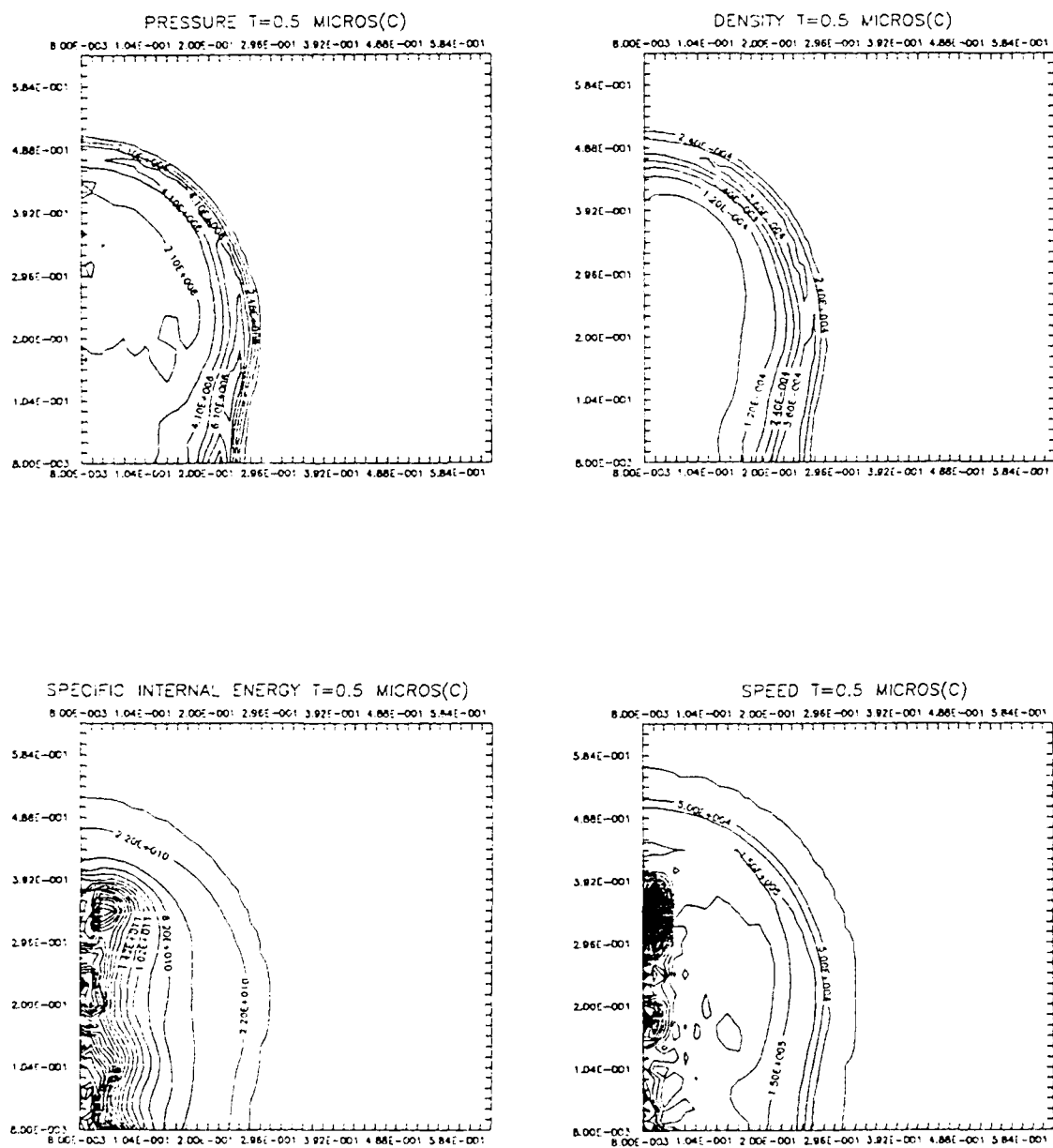
neutrals are not present. Such equilibration is discussed in detail by Spitzer[44]. The salient features are presented here.

The characteristic collision time for energy accommodation of <u>like</u> particles, in this case electrons, from gas kinetic theory is given approximately by

$$\tau_{ee} = \frac{m_e^{1/2}(3kT_e)^{3/2}}{5.71\pi n_e(Ze)^4 \ln\Lambda} \quad (S) \tag{V.3}$$

where the variables have their usual meaning; the constant, 5.71, comes from the product of 8 (statistical particle motion over 4π isotrcpic geometry) and 0.714 (statistical error function); and

$\ln\Lambda$ = coulomb cut-off range $\equiv \lambda_d/r_0$ (Debye length/radius) $\simeq 10$

Thus for electron-electron equilibration, Z=1 and

$$\tau_{ee} = \frac{8.84 \times 10^{12} \, m_e^{1/2} T_e^{3/2}}{n_e \ln\Lambda} \quad (S). \tag{V.4}$$

The characteristic time for energy accommodating collisions between <u>unlike</u> particles (electron-ion) is much longer than that for like particles. This is due to the relatively inefficient energy transfer between particles of different masses. The relationship between the electron-electron equilibration and the electron-ion equilibration is

$$\tau_{ei} \simeq \frac{m_i}{2m_e Z_i} \tau_{ee} \quad (S). \tag{V.5}$$

Inspection cf the SALE calculations yields the specific internal energy of the gas as a function of time and grid position. The temperature can be related to the internal energy via the relation $E = (3/2)kT$. At 1 nS after the laser pulse, the temperature at the shock front is 4.1×10^6K. We know from the rate coefficient investigations that at early times where $T \sim 10^6$ K, the lifetime for ionizing O^{4+} to O^{5+} at an electron density like the gas density at this temperature is 1.5×10^{-10} S. Thus the charge number is at least Z=5. After the shock front traverses a grid cell, the density is decreased due to the hydrodynamic effects to $\sim 0.1 \, N_0$. After the shock front passage, the temperature is $\sim 2 \times 10^5$ K, and the electron density is 5 x

85

$0.1(2N_0) \sim 4 \times 10^{18}$ cm^{-3}. Thus from eqs. (V.4) and (V.5) respectively, the electron-electron and electron-ion equilibration times at 10 nS after the laser pulse are

$$\tau_{ee} \sim 6 \times 10^{-13} \text{ S}$$

and

$$\tau_{ei} \sim 2 \times 10^{-9} \text{ S}$$

These times will be shorter in the shock front where the density and temperature are higher. Thus it is concluded that the SALE-derived heavy particle temperature is also a measure of the electron temperature at times comparable to the laser pulse time. Note that this argues only for kinetic equilibration, and specifically <u>does not</u> imply anything about equilibration of internal electronic excitation of the heavy particles, i.e. thermodynamic equilibrium cannot be assumed on the basis of this argument.

One can also estimate the time for electron-neutral equilibration after the shock front has passed. To first order, neglecting the atomic polarizability, Zel'dovich and Raizer[4] gives

$$\tau_{en} \approx (m/2m_e)(N_n v_e \sigma_{e,elast})^{-1} \tag{V.6}$$

where m and N_n are respectively the mass and density of the neutral species, and $\sigma_{e,elast}$ is the average cross section for elastic electron-atom collisions which can be assumed to be that for a hard sphere or gas kinetic collision. Since the smallest impact parameter is on the scale of atomic dimension, or the Bohr radius, a_0,

$$\sigma_{e,elast} \sim \pi a_0^2 \sim 10^{-16} \text{ cm}^2, \text{ and}$$

$$\tau_{en} \sim 10^{16}(m/2m_e)(N_n v_e)^{-1} \qquad (S). \tag{V.7}$$

Assuming 10% ionization (for late times), the neutral density is then 1/10 of the ion density. Using $T = 2 \times 10^5$ K and $N_n = 8 \times 10^{16}$ cm^{-3} in eq. (V.7)

$$\tau_{en} \sim 6 \times 10^{-6} \text{ S}.$$

This is considerably longer than the electron-ion equilibration time as expected because (1) the electron-neutral interaction is short ranged so that energy transfer is not as effective as in a Coulomb interaction, and (2) neutral density behind the shock front is less than the ion density. However, there is no reason to believe that the ion-neutral motion is ever

86

decoupled in LINUS since the heavy-particle collision rates are so high. Thus it is expected that the electron-neutral equilibration is given by the shortest electron-heavy particle time, in this case the electron-ion equilibration time. The single-fluid assumption for the application of SALE to LINUS is appropriate.

(2) The SALE calculation has not accounted for energy losses which arise from dissociation, excitation, ionization, and chemical reactions. It is instructive to compare these energy losses to the maximum amount of energy which could be deposited into each O_2 molecule. The number of molecules in the laser focal volume, n, is given by

$$n = NV, \tag{V.8}$$

where N = number density of molecules, and V = focal volume of the laser. For a pressure of 110 torr at room temperature, $N=3.5\times10^{18}$ cm^{-3}. The focal volume, V, is

$$V = \pi r^2 l, \tag{V.9}$$

where r = focal radius, and l = length of the focal region. It has been shown earlier that r = 10 μm and l = 54 μm, resulting in a focal volume of 2×10^{-8} cm^3. Hence, the number of O_2 molecules in the focal volume is $\sim10^{11}$ cm^{-3}. The initial laser energy is ~1 J per pulse. At 110 torr, typically $\sim13\%$ of this energy is absorbed[43]. Therefore, the maximum energy deposited is $\sim10^7$ eV per O_2 molecule.

The dissociation energy of O_2 is 5.2 eV. The oxygen ionization potentials for all charge states are 13.6, 35.2, 54.9, 77.4, 113.9, 138.1, 739.1, and 871.1 eV. Thus the generation of two O^{8+} ions from one O_2 molecule requires energy of 4.1×10^3 eV, a minute fraction of the maximum energy deposited per molecule. This implies that most of the energy is converted into PV (pressure volume) work and the energy expended in chemistry should have a small effect on the initial hydrodynamic expansion of the shock wave. At later times, the shock wave expansion would have dissipated a part of the initial laser energy as a result of PV work. The energy expended in chemistry would then have a larger effect on the hydrodynamics. The end result would be a slowing down of the shock front expansion.

(3) The SALE calculation has neglected radiation loss which may effect the shock wave expansion dynamics. It has been shown in ref. 42 that this assumption of no energy loss is valid at early times, i.e. the

emission of radiation is unimportant on the time scale of the rapid expansion of the shock wave. Thus, ignoring radiation loss is expected to have minor consequences on the hydrodynamic results.

(4) The influence of radiation on the shock front has been neglected. The large amount of energy deposited, which should result in a highly stripped core region, is precursor to the production of hard UV and soft x-ray by the highly heated gas plasma. From detonation theory, the shock speed for a point explosion behaves as $E^{1/5}$, where E is the energy in the shock. As a result of the weak dependence on energy, the effect of radiation emitted on the shock front will be minimal.

(5) The radiation emitted may partially ionize gas in front of the shock front and the pre-dosed region may then effect the propagation of the shock front. From blast wave theory[4], it is seen that the dependence of the shock pressure on heat capacity occurs via the term $1/(\gamma+1)$. Hence, any change in the heat capacity should have a small effect on the shock front parameters.

We conclude that the approach adopted for the SALE calculation gives a good estimate of both the spark size and shape. The major objective in applying the SALE code is to study the generic effects of shock wave expansion dynamics in LINUS. This goal has been successfully achieved. The behavior of the energy dissipation in the shock front is consistent with the radiative loss mechanism under nuclear conditions. The results from the coupled SALE/ARCHON calculation show that the shock formed is sufficiently strong that highly ionized states are created and recombined with electrons to form high n,l states which can emit radiation in the UV/VIS/IR region.

There are three additional LINUS-SALE-related items which are needed in order to facilitate the kinetics calculations discussed in Chapter VI. These calculations are:

(1) addition of an ultraviolet radiation loss term to account for the effect of radiative energy loss at later times. The same term used in the MICE code will be used.

(2) inclusion of partial Lagrangian character to give a more realistic description of the plasma expansion process. Because real fluids move, they cannot be accurately modelled in a totally Eulerian mode. The drawback of a full Lagrangian calculation is that the cells may become

overly distorted and unrealistic results are obtained. Therefore, a combined Lagrangian-Eulerian approach should be used.

(3) use of marker cells or particles to specifically identify the local parameters of density, pressure and temperature. This allows the tracing of the moving fluid and shows more precisely where the fluid lies within the computing mesh. In addition, it shows the manner in which the fluid configuration is changing and gives direct information of how the various hydrodynamic parameters vary as a function of time and spatial location.

VI. LINUS REACTION KINETICS MODEL

A. GENERAL

The purpose of this chapter is to present a simplified model of the kinetics in the LINUS plasma. Section VI.B explains the approach adopted for determining the expressions for the rate coefficients of the various reactions. Section VI.C discusses the reaction set and initial temperature profiles. Section VI.D shows the results of the kinetic calculation.

One of the key issues in understanding laser-induced plasma relaxation is a knowledge of the time profiles of the electron, ion and neutral densities and temperature. The reason is that, as described in Chapter II of this report, these parameters determine the characteristics of free-free, free-bound and bound-bound emission. The lack of thermodynamic equilibrium complicates a detailed analytical understanding of these parameters, thus a numerical kinetic approach is required. Significant progress has been made in developing such a numerical model, but several technical issues are still as yet unresolved. The approach is to stipulate the initial concentration of species that have been detected in spectral studies of oxygen, namely O, O^+, O^{2+}, O^{3+} and O^{4+} (O^{5+} is included as well but has yet to be spectrally identified in the plasma). Temperature-dependent analytical rate descriptions are then defined for recombination (three-body, dielectronic and radiative) and collisional re-ionization processes.

The temporal profile of the electron temperature must be determined to drive the time-dependent kinetics. Although this has yet to be experimentally measured, there is both spectral data and hydrodynamics SALE calculations to support the profile determination. The temperature-dependent rate coefficients are then determined using this profile. The numerical solution to the coupled rate equation model is performed using the chemical dynamics code ARCHON, currently under development by MRC for DNA. ARCHON uses a variable expansion series, depending on accuracy required, and analytically treats "stiffness". Thus accuracy is conserved as finite step differences approach small numbers. It will also accurately include the flux-divergence (concentration gain or loss with bulk gas velocity). The advantages of using this code are: (1) it is completely modular so that any set of coupled rate equations can be solved independently with step-by-step updating of the rate coefficients, and (2)

it is sufficiently efficient so that analyses such as required for LINUS are fully achievable on PC-level computers.

The results of this model are subject to uncertainty both in our knowledge of the recombination and re-ionization functions and in the temporal-spatial behavior of the LINUS expanding plasma. However, the results obtained at 6 μS and 12 μS are in reasonable agreement with the results inferred from comparisons of synthetic and experimental spectral data discussed in Chapter IV of this report. Efforts are continuing, to understand both recombination/re-ionization and spatial dynamics. The model will be updated as new information becomes available.

B. RECOMBINATION/RE-IONIZATION

The recombination/re-ionization rate coefficient expressions in the present model are based mainly on theoretical arguments. There is significant uncertainty in both charge-state scaling and applicable temperature range. Three-body recombination and electron-impact re-ionization are probably most discussed in the literature and the best understood. This is fortunate since for experiment times > 10 nS, the dominant recombination process for times of interest is via the three-body channel using the temperature profiles chosen. Dielectronic recombination is an area of rather intense research at the present time and radiative recombination is also an area of active research, although with less intensity. Thus these rate coefficient expressions are subject to updating as more information is made available.

The model at present treats each ion and atom as a single entity, without following every energy level. It is based on recombination into unspecified levels and re-ionization out of the ground state of the species, which is what the LINUS data indicate. This approach is not quantitative, but gives a qualitative picture of the species' time history. As the model is further developed, refinements on level-dependent rates will be made for higher fidelity calculations. Further spatial data from the experiments and temperature calculations from modifications to the SALE code will be incorporated for kinetics calculations on a two-dimensional grid (assuming a single plane of symmetry).

Electron Impact Re-ionization:

Electron impact ionization is discussed in Zel'dovich and Raizer (ref. 4, p389). The expression derived for the rate coefficient, k_i, is

$$k_i = \sigma_e \bar{v}_e [(I/kT_e) + 2] \exp(-I/kT_e) \qquad (cm^3 S^{-1}) \qquad (VI.1)$$

where

σ_e = interaction cross section = CkT_e (C = constant given by Zel'dovich and Raizer for the O-atom, $0.6E\text{-}17$ cm^2 eV^{-1})

$\bar{v}_e$ = electron velocity function = $(8kT_e/\pi m_e)^{\frac{1}{2}}$

I = ionization potential of the ground state

and other variables have their usual meaning. Inspection of (VI.1) shows a two-function pre-exponential behavior with temperature, $T^{1/2}$ for $kT_e < I$ and $T^{3/2}$ for $kT_e > I$. In the derivation of the final expression used in the model, it is assumed that re-ionization when $kT_e < I$ is relatively negligible, hence $kT_e > I$, and equation (VI.1) reduces to

$$k_i = 2[CkT_e][8kT_e/\pi m_e]^{\frac{1}{2}}\exp(-I/kT_e) = C'T_e^{3/2}\exp(-I/kT_e) \ (cm^3 S^{-1}) \qquad (VI.2)$$

Derivation of the scaling of C' with charge-state z is based on the discussion in Zel'dovich and Raizer (ref. 4, p395) that for constant $I(z)/kT$, $k_i(z) = k_i(1)/Z^3$. C' is then calculated by deriving the corresponding temperature for constant $I(z)/kT$ and scaling the derived rate coefficient at the corresponding temperature following Z^{-3}. The strong dependence of C' with 7 reflects the decreased effective interaction radius of the ions. Therefore, k_i in the model scales as Z^{-3}, as $T^{3/2}$, and as $\exp(-I/kT_e)$.

Inherent in this derivation is that re-ionization occurs primarily from the ground level of the species. In thermodynamic equilibrium at high temperatures, this is inaccurate. However, thermodynamic equilibrium is not obtained in LINUS, as evidenced by different spectroscopic "temperatures" for different species. Thus there is insufficient information at this time to include ionization from upper electronic levels but will be a point of continued research. This issue is discussed below.

Three-Body Recombination:

As with electron impact ionization, three-body recombination is discussed in some detail in Zel'dovich and Raizer (ref. 4, p407). The expression given for this process, k_t, is

$$k_t = \frac{2^6 \pi (2\pi)^{\frac{1}{2}} e^{10} Z_i^3}{3^5} \frac{1}{m_e^{\frac{1}{2}}} (kT_e)^{-9/2} \qquad (cm^6 S^{-1}) \qquad (VI.3)$$

where the variables have their usual meaning. This reduces numerically to

$$k_t = 7.4E\text{-}20 \; Z_i^3 \; (T/300)^{-9/2} \qquad (cm^6 S^{-1}) \qquad (VI.4)$$

which is the expression used in the model. Thus k_t scales as Z_i^3 and $T^{-9/2}$.

Dielectronic Recombination:

Deriving a rate coefficient for dielectronic recombination is more problematic than with either impact ionization or three-body recombination. The process is complex and not well understood, since a resonant stabilizing transition must occur simultaneously with the electron capture. This obviously is a function of both the available energy levels in the specific species and the dynamic population of those levels. Bates[45] presents a discussion for singly-charged oxygen and nitrogen. The expression for oxygen dielectronic recombination, k_d, is (modified to include the term $(T/300)^b$)

$$k_d = 6.9E\text{-}12 \; (T_e/300)^{-3/2} \exp(\epsilon/kT_e) \qquad (cm^3 S^{-1}) \qquad (VI.5)$$

where

ϵ = required stabilizing energy, 0.48 eV for O^+,

and other variables have their usual meaning.

The variable, ϵ, is specific to the individual charged species and has not been characterized for higher charge states in oxygen. For want of a better value for the higher charged species, this value is assumed as invariant, although this is very likely incorrect. It is also assumed for this model that the Coulomb attraction potential plays some role, thus $k_d \propto Z^2$.

Radiative recombination:

For the rate coefficient for radiative recombination, k_r, the expression in the DNA handbook[46] is assumed as

$$k_r = 3.5E\text{-}12 \; (T/300)^{-0.7} \qquad (cm^3S^{-1}) \qquad (VI.6)$$

Kim and Pratt[47] discuss the derivation of expressions for radiative recombination which scale as $Z_{eff}^4 = [0.5(Z + Z_i)]^4$ where Z is the nuclear charge and Z_i is the ion charge state. Since in this case, Z is constant and Kim and Pratt discuss other work as suggesting scaling as Z_i^4, the fourth-power scaling with charge state is assumed here. There is certainly a large uncertainty in the rate coefficient for radiative recombination in the model and will receive attention as more information is available.

Although considerable uncertainty is exhibited in dielectronic and radiative recombination rate coefficients, for experiment times > 10 nS, three-body recombination is the dominant recombining channel for the temperature profiles chosen. Thus the actual uncertainty in total effective recombination rate is concentrated in the process for which the analytical expression is most certain.

C. INITIAL CONDITIONS AND TEMPERATURE PROFILE

The reaction set model, along with the rate coefficients is shown in Table VI-1. The ionization charge-state limit is currently set at O^{5+}, although the highest charge state detected to-date in the spectroscopic investigations is O^{4+}.

The initial conditions for the start of the calculation are somewhat *ad hoc* but the results are found to be quite insensitive to the starting conditions chosen. It is assumed that the emission of interest does not come directly from the focal region of the laser excitation, but from the

94

TABLE VI-1

Reaction Set For LINUS Recombination Model

	REACTION	TYPE	$k(t)=a(T/300)^b e^{-c/T}$		
			a	b	c
1.	$O^{5+} + e + e \longrightarrow O^{4+} + e$	k_t	8.7E-18	-4.5	0
2.	$O^{5+} + e \longrightarrow O^{4+}$	k_d	1.7E-10	-1.5	5.6E3
3.	$O^{5+} + e \longrightarrow O^{4+}$	k_r	2.2E-9	-0.7	0
4.	$O^{4+} + e + e \longrightarrow O^{3+} + e$	k_t	4.5E-18	-4.5	0
5.	$O^{4+} + e \longrightarrow O^{3+}$	k_d	1.1E-10	-1.5	5.6E3
6.	$O^{4+} + e \longrightarrow O^{3+}$	k_r	8.9E-10	-0.7	0
7.	$O^{3+} + e + e \longrightarrow O^{2+} + e$	k_t	1.9E-18	-4.5	0
8.	$O^{3+} + e \longrightarrow O^{2+}$	k_d	6.2E-11	-1.5	5.6E3
9.	$O^{3+} + e \longrightarrow O^{2+}$	k_r	2.8E-11	-0.7	0
10.	$O^{2+} + e + e \longrightarrow O^{+} + e$	k_t	5.6E-19	-4.5	0
11.	$O^{2+} + e \longrightarrow O^{+}$	k_d	2.8E-11	-1.5	5.6E3
12.	$O^{2+} + e \longrightarrow O^{+}$	k_r	5.6E-11	-0.7	0
13.	$O^{+} + e + e \longrightarrow O + e$	k_t	7.4E-20	-4.5	0
14.	$O^{+} + e \longrightarrow O$	k_d	6.9E-12	-1.5	5.6E3
15.	$O^{+} + e \longrightarrow O$	k_r	3.5E-12	-0.7	0
16.	$O + e \longrightarrow O^{+} + e + e$	k_i	3.9E-12	1.5	1.6E5
17.	$O^{+} + e \longrightarrow O^{2+} + e + e$	k_i	1.2E-13	1.5	4.0E5
18.	$O^{2+} + e \longrightarrow O^{3+} + e + e$	k_i	1.8E-14	1.5	6.4E5
19.	$O^{3+} + e \longrightarrow O^{4+} + e + e$	k_i	4.7E-15	1.5	8.9E5
20.	$O^{4+} + e \longrightarrow O^{5+} + e + e$	k_i	1.3E-15	1.5	1.3E6

k_t=three-body k_d=dielectronic k_r=radiative k_i=re-ionization

UV and shock heated region surrounding the focal region. While this assumption yields results consistent with the observations, a detailed description of the focal core region is as yet undetermined. LINUS discussions[48] have led to the suggestion that the core region is fully ionized in which case it will have to be treated in more detail. (The code RADHY, presently under development at MRC/Santa Barbara will be applicable to this region). Computationally, it is found that the high initial temperatures coupled with the temperature-dependent ionization rates for t<9 nS (discussed below) establish the species concentrations independent of reasonable externally chosen starting conditions. For these calculations, a cell pressure of 110 torr O_2 was assumed to match a set of experimental conditions for which LINUS data has been obtained.

The temperature-time profile is calculated using two separate techniques. The first temperature profile was derived from the spectroscopic temperatures obtained by Dzelzkalns[49]. As discussed in ref. 42, the results using this profile were inconsistent with experimental observations, thus a more detailed approach is necessary. That the kinetic results obtained from this temperature profile do not agree with experimental data is, in retrospect, not surprising. First, in order for the electrons to be strongly coupled to the emitting levels within ~kT of the ionization limit, collisional probability arguments require that the population of those levels would have to approach the species concentration. Given that the radiative rates for optically-allowed transitions from these levels is typically of order one nanosecond, and the ion-ion collision time is of order 10^{-11} S, such a population inversion is highly unlikely. Thus, electron-thermalizing collisions will more likely occur with electronically relaxed species. Second, inspection of the experimental data on spectroscopic temperatures indicates that at any given time, the electronic temperature is a function of the charge state, Z. Hence a unique temperature cannot be assigned. As a result of this investigation, it is concluded that the spectroscopic temperatures exhibited in the spectral analysis are not a reliable indicator of the electron kinetic temperature.

The more detailed temperature profile was derived from examination of the conditions just behind the shock front in the SALE calculations described in Chapter V of this report. It has been shown in Chapter V that the electron temperature, the critical parameter for recombination, is coupled to the heavy particle temperature. The latter temperature is obtained from the SALE specific internal energy, I, calculations via the equation

$$T = mI/(k(\gamma-1)) \qquad (K) \qquad\qquad (VI.8)$$

where m = mass of oxygen atom, k = Boltzmann constant, and γ = ratio of specific heats. The results at the point $x = 0.05$ cm and $y = 0.288$ cm are listed in Table VI-2.

TABLE VI-2

SALE-Derived Electron Kinetic Temperature at x=0.05 cm and y=0.288 cm

Time (sec)	Temperature (K)
0.100000E-09	300.0
0.150000E-07	1806.0
0.200000E-07	18035.9
0.250000E-07	50648.3
0.360000E-07	94310.4
0.400000E-07	96753.4
0.450000E-07	92899.2
0.500000E-07	85828.8
0.700000E-07	53616.0
0.120000E-06	45230.4
0.500000E-06	26808.0
0.100000E-05	20492.8
0.500000E-05	8359.4

From these values, an analytical expression for the temperature is obtained. This expression is used in the ARCHON rates driver module to update the temperature-dependent rate coefficients for driving the kinetics. The temporal profile of the heavy particle temperature from SALE is shown in Figure VI.1. Also shown is the code-interpolated temperature driver for the rate coefficient update. The two are slightly different due to the size of the time step in the integration. The difference is not important.

D. KINETIC RESULTS AND DISCUSSION

The kinetic results using the more detailed derivation of the temperature profile obtained from the SALE calculations are shown in Figure VI.2. In this case, the initial concentrations were determined from the SALE result showing that behind the shock front, $N \sim 0.1N_0$, i.e. it is assumed that the UV deposition dissociates and ionizes the oxygen to a mixture of 90% 0 and 10% 0^+. The interesting result from examining this figure is that *for this cell*, the electron density after 10^{-5} S still
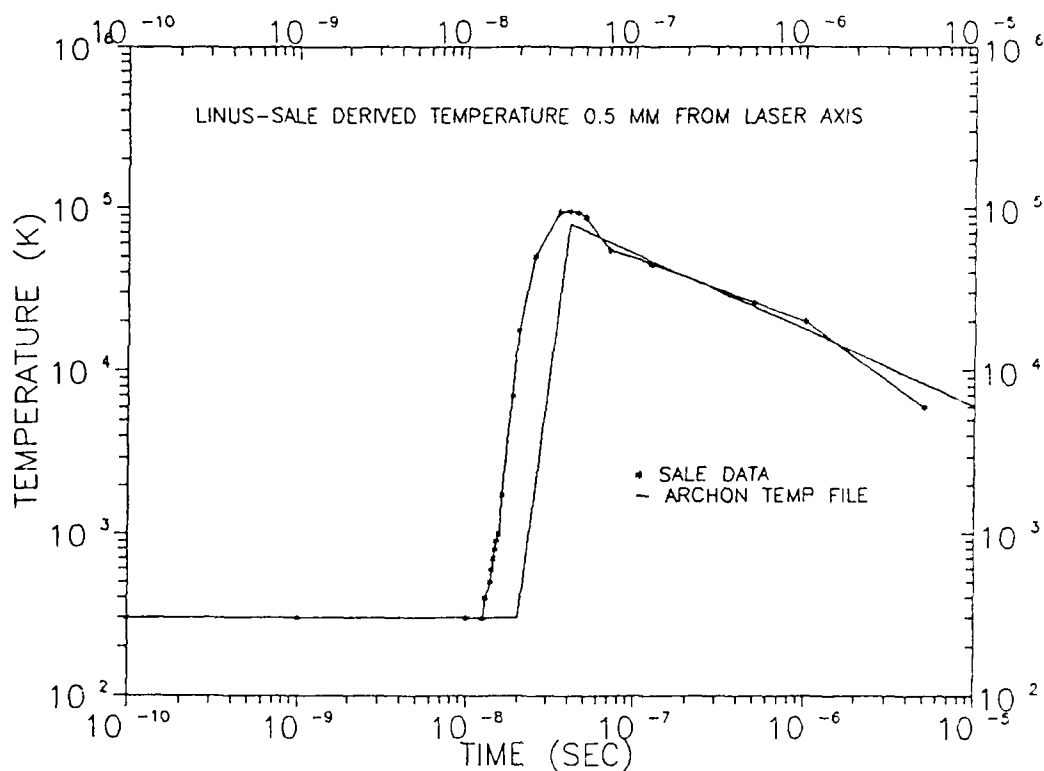
97

Figure VI.1. Temperature profile derived from the post-shock front region
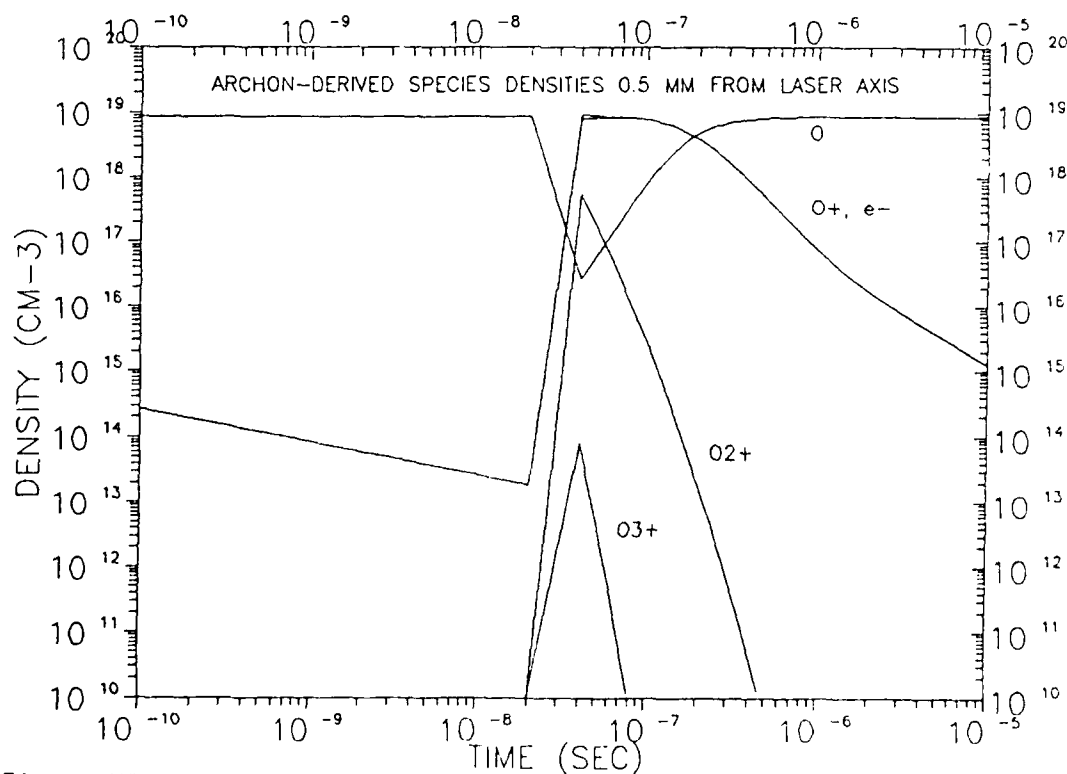of the SALE calculations.

Figure VI.2. Temporal profile of species concentrations following the
temperature profile of figure VI.1. The initial cell
pressure was taken as 110 torr.

exceeds 10^{15} cm^{-3}. This is consistent with the Stark calculation which indicates an electron density of about 7×10^{15} cm^{-3} for delay time of 12 μS. It is also clear from Figure VI.2 that when the shock front hits the cell at ~1.5E-8 S, the ionization is virtually instantaneous.

Comparison of this kinetic calculation with the experimental data results in some agreement and some anomalies. The consistent results are:

1. The electron density is comparable to the Stark result at 6 μS and 12 μS. This is important since, as discussed in Chapter II, the electron density is one of the determining parameters in radiance calculations.

2. At times less than ~10 nS, emission from the plasma is dominated by continuum. The calculation indicates that the species O^{5+} disappears rapidly after this time, consistent with the fact that it is not identified in the spectral data.

3. Between 25 nS and 50 nS, O^{4+} is identified in the spectra as described in Chapter III. It is not present in the spectra after this time, as predicted by the kinetic calculations.

4. Except for two narrow O-neutral lines seen at early times (discussed in Chapter III), O-atom emission does not occur much earlier than ~25 nS, and is seen well beyond 1 μS.

5. O^{3+}, O^{2+} and O^+ appear in sequence at approximately the times suggested by the calculations.

There are discrepancies, however, which lead one to conclude that additional detail is required to completely understand the kinetic behavior. These are:

1. Spectroscopic identification of O^{2+} and O^{3+} extends to times greater than 400 nS. The kinetic model does not predict such behavior.

2. There is no indication from strict kinetic arguments that the early emission of O-neutral should be present.

Both the agreement and the discrepancies can be explained in terms that point to a fundamental requirement to obtain time-resolved _spatial_ data from the LINUS experiment to determine the region of emission. In

discussions at Los Alamos[48], it has been argued that at early experimental times, three distinct spatial regions exist, each with their own temperature/density character. They are:

1. The "core" region, defined by the original focal region, where there is sufficient laser intensity to completely strip the oxygen to O^{8+}. Radiation from this region will initially be in the x-ray and hard UV spectral regions. The core will relax at a different rate than the modeled shock-region, and may be the source of the extended O^{3+} and O^{2+} emission. This has yet to be investigated.

2. The hydrodynamic region, described by the SALE calculations, where the emission is determined by the conditions behind the expanding shock front. This is described in Chapter V and is the driver for the kinetics calculations described above.

3. The radiation-dosed region, where the emission is due to excitation from x-ray and UV deposition into the surrounding gas. The cross section for x-ray absorption by O_2 is of order 10^{-18} cm^2 (varies as ν^{-3}, but ν has not yet been characterized) and the oxygen concentration is ~4×10^{18} cm^{-3}. Thus the characteristic e^{-1} length for absorption is ~2.5 mm, which is approximately the lateral extent of the visible spark. The spectrally narrow emission from O-neutral at very early times has been tentatively attributed to radiation dosing in the initially cool surrounding gas. The fact that it evolves into a very broad feature with time is consistent with the shock passage through the region subsequent to radiation deposition.

Inspection of the data on spectroscopic temperatures indicates emission from distinctively separate spatial regions of the plasma. The O^{3+} and O^{2+} both exhibit time dependent electronic temperatures, relaxing as the plasma relaxes. However, both O^+ and O-neutral show a much less marked temperature decay. This is difficult to reconcile under the same plasma relaxation conditions. It is possible that the lower-energy O and O^+ emit early from the outer regions of the spark, excited initially by UV and x-ray deposition and later from the relaxing inner plasma region described in the kinetic model above. However, this is only conjecture, and cannot be further confirmed without the spatially resolved data.

A final observation is in order concerning the applicability of kinetic calculations that do not account for differential rate processes

from excited-state levels. Clearly re-ionization and recombination do occur from excited levels. However, the three-body rate dominates recombination under these conditions, with a time constant of the same order as typical optically-allowed radiative time constants (~1 nS). The same is also true of the mid-time re-ionization (10 nS <t <100 nS). Furthermore, Zel'dovich and Raizer (ref. 4, p394 and 410) discuss the effect of excited species on both the recombination and ionization rates. The argument is based on the case where a Boltzmann distribution can be defined, i.e. where there is some definable temperature. It is found that both ionization and capture rates increase with principal quantum number, n (capture rate is related to, but not the same as recombination rate since capture into a slightly bound level, $\Delta E < kT$, usually results in re-ionization). The ratio of capture to ionization is given as (Zel'dovich nomenclature)

$$\frac{\beta_{n,n-1}}{\alpha_{n-1,n}} = \frac{(n-1)^2}{n^2} \, \exp(\Delta E/kT) \qquad\qquad (VI.10)$$

where β = capture rate and α = ionization rate. Thus as n becomes large and ΔE becomes less than kT, the rates approach one another. Therefore it can be argued that these kinetic calculations, while perhaps not quantitative, qualitatively represent the plasma behavior. Such a conclusion is supported by the independent agreement of the present kinetic calculation and that involving the Stark broadening-spectral data comparisons. However, to perform a truly time-dependent quantitative calculation, both spatial information and state-dependent detail will have to be included in the model.

This type of analysis assumes, of course, that the conditions along the optical line-of-sight are uniform. This is not generally true although at late times after shock transit and significant relaxation, it may be approximately true. Further development of this point will await additional spatial/temporal investigations in LINUS.

VII. SUMMARY AND RECOMMENDATIONS

A. OBSERVATIONS

In the course of analyzing the LINUS experiment, emphasis has been placed on phenomenological applicability of the experimental results to the validation of present models of nuclear plasma emissions. Early observations of both visible and infrared line emission indicate that the line positions predicted in the models via energy defect calculations are approximately correct but there are indications that the predicted relative line strengths are not as observed. It is yet unclear, however, whether any apparent differences are due to the experimental conditions, since LINUS initial pressures are higher than that normally obtained for model application. It has, nevertheless, been obvious from the initiation of the experiment that interesting relevant results could be obtained even at the high initial pressures. This is due in part to the extremely high temperatures achieved in the core that, in turn, causes a shock expansion behind which much reduced pressure conditions obtain. Indeed, this initial core along with the attendant shock may make the LINUS experiment more like an airburst than originally expected (this is not necessarily equivalent to simulation).

In spite of the very interesting observations from LINUS during this contract period, much more detail is required in both the data obtained and the analysis of that data in order to proceed with transition of the results to nuclear plasma understanding. The visual observations indicate a complex spatial structure, and spectroscopic results have clearly shown the lack of thermodynamic equilibrium. Supporting hydrodynamic calculations indicate an exceedingly rapid initial expansion consistent with the large amount of energy deposited in the gas. The observation of early narrow line emission was totally unexpected and theoretical arguments of Stark line broadening effects indicate that the spectra will be substantially affected at critical electron densities obtained in LINUS. In Section II of this report, the analytic relationships describing the plasma emission behavior were reviewed in terms of the requirement to determine *local* parameters of density and temperature, not the average values across highly variable conditions. Thus further progress in LINUS understanding requires a very detailed approach to both data acquisition and analytical treatments.

The major findings during this contract period as reported in this document are summarized below with emphasis on setting direction for further work.

1. The SALE code is apparently quite applicable to the LINUS experiment with relatively few minor modifications. The code results are consistent with the macroscopic observation of the elongated discharge region. It has been demonstrated that the effect of gas optical pre-dosing will have little effect on the shock behavior since its energy is negligible compared to the laser input energy. The major results are: (i) The shock expansion is very rapid, achieving observed spark dimensions on the same time scale as the laser pulse width. This means that time-resolved observations of the shock expansion will be very difficult. (ii) The region behind the shock is reduced in pressure about an order- of-magnitude below cell ambient. This coupled with the very high SALE-derived heavy particle temperature may account for the persistence of high electron densities (see below).

2. The theoretical Stark calculations of the effect of ions on electronic state mixing and the effect of electrons on level broadening indicate that Stark broadening may have a major impact on our understanding of LWIR plasma emissions, especially under multi-burst conditions. High electron density mixes and broadens high-lying atomic energy levels and dramatically changes the spectral character of the resulting emission. This effect has been shown to be quite useful as an internal monitor of electron density, electronic temperature, and to a lesser degree the electron temperature in the LINUS experiment. It is important to note that such changes in emission character under nuclear burst conditions is not presently modeled in any nuclear plasma code.

3. Kinetic modeling based on temperatures derived from the SALE calculations yields electron densities consistent with those argued from the Stark calculations. The predicted sequential appearance of charged species is approximately correct, but the observed persistence of emission from charge states is not yet accounted for in the model. Thus additional level-dependent detail is required for general model applicability. Nevertheless, the model appears to be useful for approximate predictions of electron densities, and that the SALE-derived heavy-particle temperatures are a valid measure of the local electron temperatures due to the rapid electron-ion kinetic equilibration.

4. The early-time continuum experiments indicate that the observed background continuum behaves spectrally as a blackbody if a homogeneous emission region is assumed. This would indicate that the observed emission is optically thick and may not be a reliable measure of free-free or free-bound emission. At later times (>1 μS) however, the continuum appears to be consistent with free-free/neutral emission. This is important since free-free neutral emission is one of the areas of significant uncertainty in NWE codes. The results to-date have been based on data obtained in limited spectral and temporal regions. More data must be acquired before firm conclusions can be drawn.

One of the more dramatic experimental observations in the continuum investigation was the existence of early narrow-line emission followed by broadening of the lines with time. This is consistent with cold atomic emission due to x-ray/UV deposition followed by shock heating of the emission region. This surprising result may form the basis for extended LINUS investigations into optical deposition/excitation.

B. RECOMMENDATIONS

Based on the results summarized above, recommendations for continued investigations are made. These recommendations strongly suggest the requirement for a very detailed experimental and analytical approach to push LINUS beyond integrated phenomenological observations.

EXPERIMENTAL DEVELOPMENT

E-1. _Time and spatially_ resolved data at all wavelengths is a requirement for further interpretation of the LINUS results. The Stark and kinetics calculations presently assume a homogeneous emission region. Spectroscopic data on which the spectroscopic temperatures and continuum analyses are based are spatially integrated. There is reason to believe that there are at least three distinct emitting regimes in the LINUS discharge: (a) an initially completely stripped core region, (b) a hydrodynamic region where shock effects determine the emission behavior, and (c) a region where x-ray and U.V. deposition pre-excites the surrounding gas to electronically excited but kinetically cold conditions. Spatially

104

resolved data will result in detailed Abel analyses of the radial behavior to validate the SALE results and determine whether the spectroscopic temperatures derived from the spectral data represent different emitting regions. Spatially integrated data will not allow further analysis of such behavior.

E-2. Time-resolved spectral coverage from LINUS should be extended to include the LWIR for verification of the Stark predictions and continuum results. The former may form the basis for a major upgrade to nuclear plasma models as they affect system filter design, and the latter may aid in validation of the free-free and free-bound models. There is not yet sufficient spectroscopic information to verify and validate the models of these effects.

E-3. Values for the electron density and electron temperature should be experimentally measured by seeding the oxygen plasma with 1 % to 3% hydrogen. The broadening characteristics of the hydrogen H_β line at 4861 A has been well studied and the electron density can be determined from line width measurements to about 10 % accuracy.

E-4. Detailed data should be taken on the early-time narrow-line emission. This surprising observation has strong potential to lead to experimental data on x-ray and ultraviolet energy deposition and excitation. This is a major area of uncertainty in the present nuclear models.

E-5. Experimental design and hardware acquisition should be pursued to allow LINUS extension into lower pressure regimes. This is not suggested at this time to be a high priority since much remains to be learned from the present configuration. However, planning should begin now for future LINUS applications.

MODEL DEVELOPMENT:

M-1. The Stark line broadening code should be improved upon by adding a restart capability in the calculation of electron widths. Problems related to calculating the electron widths at electron densities below 10^{14} cm^{-3} should be investigated. Comparisons of the electron widths calculated by the unperturbed method versus the semi-perturbed and fully-perturbed methods should be made.

M-2. The SALE/LINUS code should be further developed only to the extent of including the UV loss term, marker cells, and Lagrangian character. It will then be a very useful general purpose tool for LINUS temperature/density characterization as a function of input energy. It will also be useful for systematic investigations of the effects of optical pre-dosing and spectral energy loss on the shock expansion behavior. Further development of SALE/LINUS to include chemistry is probably inappropriate since the RADHY code, which is currently under development, will handle such details.

M-3. The kinetics model should be further developed to include state-dependent kinetics. In its present form, it appears to adequately describe the general electron behavior but does not yet correctly model the charge-state emission details. Further development will require detailed descriptions of distribution of level populations from recombination, and collisional-radiative level de-populations. This may suggest a major atomic-physics effort, but it is yet premature to determine this.

M-4. The LINUS results have progressed to the point where model comparisons with RADHY and EGG22 extended to high electron densities may be appropriate. This should be actively pursued.

VIII. REFERENCES

1. Sappenfield, D. S., "Electron Radiation", chapter 6, "Physics of High Altitude Nuclear Burst Effects", Technical Report DNA 4501F (U), 1977.

2. Minck, R.W., "Optical-Frequency Electrical Breakdown in Gases", J. Appl. Phys., 35, 252, 1964.

3. Sappenfield, D., "Radiation from a Recombining Oxygen Plasma", Los Alamos Supplemental Report LA-4303 (U), 1971.

4. Zel'dovich, Y.B. and Raizer, Y.P., "Physics of Shock Waves and High Temperature Hydrodynamic Phenomena", Academic Press, New York, 1966.

5. Holland, D.H., Archer, D.H., Berkowitz, B.J., Hart, W.C., Hendrick, R.W., and Humphrey, C., "Physics of High Altitude Nuclear Burst Effects", Technical Report DNA-4501F (U), Chap. 6, 1977.

6. Taylor, R.L. and Caledonia, G., "Experimental Determination of the Cross-Sections for Neutral Bremsstrahlung", J. Quant. Spectrosc. Radiat. Transfer, 9, 681, 1969.

7. Geltman, S., J. Quant. Spectrosc. Radiat. Transfer, 13, 601, 1973.

8. McWhirter, R.W.P., "Plasma Diagnostic Techniques", Chap. 5, "Spectral Intensities", R.H., Huddlestone, S.L. Leonard, eds., Academic Press, New York, 1965.

9. Bates, D.R., Kingston, A.E., and McWhirter, R.W.P., "Recombination Between Electrons and Atomic Ions: I. Optically Thin Plasmas", Proc. Roy. Soc. A, 267, 297, 1962.

10. Armstrong, R.A., Lucht, R.A., and Rawlins, W.T., "Spectroscopic Investigation of Laser-Initiated Low-Pressure Plasmas in Atmospheric Gases", Appl. Opt., 22(10), 1573, 1983.

11. Lurie, J.B., Miller, S.M., Blumberg, W.A.M., and Armstrong, R.A., Chem. Phys. Lett., "Short-Wavelength Infrared Line Emission in a Laser-Produced Oxygen Plasma", 120, 481, 1985.

12. Wiese, W.L., Smith, M.W., and Glennon, B.M., "Atomic Transition Probabilities, Volume I, Hydrogen Through Neon", National Standard Reference Data Series NBS-4, 1966.

13. Bekefi, G., "Principles of Laser Plasmas", Wiley & Sons, 1976.

14. Griem, H. R., "Spectral Line Broadening by Plasmas", Academic Press, New York, 1974.

15. Dzelzkalns, L., Private Communication, 1989.

16. Townes, C.H. and Schalow, A.L., "Microwave Spectroscopy", Dover Publications, Inc., New York, 1975.

17. Thorne, A.P., "Spectrophysics", Chapman and Hall, London, 1988.

18. Anderson, P.W., "Pressure Broadening in the Microwave and Infra-Red Regions", Phys. Rev., 76, 647, 1949.

19. Press, W.H., Flannery, B.P., Teukolsky, S.A., and Vetterling, W.T., "Numerical Recipes - The Art of Scientific Computing", Cambridge University Press, 1986.

20. Baranger, M. and Mozer, B., "Electric Field Distributions in an Ionized Gas", Phys. Rev., 115, 521, 1959; Phys. Rev., 118, 626, 1960.

21. Hooper, C.F., Jr., Phys. Rev., 149, 77, 1966; Phys. Rev., 165, 215, 1968; Phys. Rev., 169, 193, 1968.

22. Tighe, R.J. and Hooper, C.F., Jr., Phys. Rev. A, 14, 1514, 1976; Phys. Rev. A, 15, 1773, 1977; Phys. Rev. A, 17, 410, 1978.

23. Hooper, C.F., Jr., Private Communication, 1989.

24. Holtsmark, J., Ann. Phys., 58, 577, 1919.

25. Moore, C.E., "Selected Tables of Atomic Spectra. Atomic Energy Levels and Multiplet Tables OI", Nat. Stand. Ref. Data Ser., Nat. Bur. Stand. (U.S.) 3, Sec. 7, 1976.

26. Edlén, B., "Handbuch der Physik", Vol. 27, ed. S. Flugge, Springer, Berlin, 1964.

27. Lin, C., Private Communication, 1989.

28. Oertel, G.K. and Shomo, L.P., "Tables for the Calculation of Radial Multipole Matrix Elements by the Coulomb Approximation", Astrophys. J. Suppl. Ser., 16, 175, 1968.

29. Condon, E.U. and Shortley, G.H., " The Theory of Atomic Spectra", Cambridge University Press, 1963.

30. Weisskopf, V.F., Z. Phys., 75, 287, 1932.

31. Baranger, M., Phys. Rev., 111, 494, 1958; Phys. Rev., 112, 855, 1958.

32. Private Communication from SPEX personnel, 1989.

33. Assous, R., J. Quant. Spectrosc. Radiat. Transfer, 10, 975, 1970.

34. Conner, W. and Lin, C., Private Communication, 1989.

35. Wiese, W.L. and Murphy, P.W., "Shifts and Widths of Some Stark-Broadened Oxygen Lines in an Arc Plasma", Phys. Rev., 131, 2108, 1963.

36. Goly, A. and Weniger, S., "Widths and Shifts of Some Plasma-Broadened Oxygen and Carbon Multiplets", J. Quant. Spectrosc. Radiat. Transfer, 38, 225, 1987.

37. Wende, B., ed. "Spectral Line Shapes", Proc. 5th Internat. Conf., Berlin, 1981.

38. Mancini, R.C. and Hooper, C.F., Jr., "Field-Dependent Dipole Matrix Elements and Their Application to the Calculation of Plasma-Broadened Line Profiles", Rev. Sci. Instrum., 59, 1512, 1988.

39. Amsden, A.A., Ruppel, H.M., and Hirt, C.W., "SALE: A Simplified ALE Computer Program for Fluid Flow at All Speeds", LA-8095 (U), 1980.

40. Armstrong, R.A., "Laser-induced Plasma Analysis", MRC-NSH-R-0001(U), 1985.

41. Cosner, K., Private Communication, 1988.

42. Ip, P., Armstrong, R.A., and Baird, J.C., "Investigation of Laser-Induced Plasma Processes", AFGL-TR-87-0052, ADA190463, 1986.

43. Dzelzkalns, L., Private Communication, 1986.

44. Spitzer, L., "Physics of Fully Ionized Gases", Interscience Publishers, New York, 1956.

45. Bates, D.R., "Dielectronic Recombination to Normal Nitrogen and Oxygen Ions", Planet. Space Sci., 9, 77, 1962.

46. Blank, C.A., Baurer, T., Bortner, M.H., and Feryok, A.A., "A Pocket Manual of the Physical and Chemical Characteristics of the Earth's Atmosphere", DNA Technical Report DNA 3467H (U), 1974.

47. Kim, Y.S. and Pratt, R.H., "Direct Radiative Recombination of Electrons with Atomic Ions: Cross Sections and Rate Coefficients", Phys. Rev. A, 27 (6), 2913, 1983.

48. LINUS Topical Meeting, Los Alamos National Laboratory, 1987.

49. Dzelzkalns, L., Private Communication, 1987.